WASHINGTON UNIVERSITY IN ST. LOUIS

School of Arts & Sciences
Department of Physics

Dissertation Examination Committee:
Kater W. Murch, Chair
Erik A. Henriksen
Michael C. Ogilvie
Robert B. Wexler
Chong Zu

Entanglement-Enhanced Metrology With Superconducting Circuits

by
Xingrui Song

A dissertation presented to
Washington University in St. Louis
in partial fulfillment of the
requirements for the degree
of Doctor of Philosophy

May 2025
St. Louis, Missouri

Table of Contents

List of Figures

List of Tables

Acknowledgments

This thesis is dedicated to my advisor, Prof. Kater Murch, whose patience, guidance, and unwavering support have profoundly influenced my academic journey. The freedom he has granted me has enabled me to explore numerous fascinating aspects of physics both within and beyond the scope of my research projects. I am also sincerely thankful to every member of the Murch lab. I have learned a great deal from each one of you, and the experiences and insights I have gained here have profoundly shaped my cognition of reality. I couldn't have reached this point without the support of every member of the Murch lab.

I would like to thank my parents for their support in my pursuit of scientific research—they are the source of my confidence. An equal amount of gratefulness is due to my wife, Shilling, for joining me on this journey. She provides me with a solid foundation for all my future endeavors. We have shared both happiness and sorrow, and our complementary personalities and skills have made our partnership a balanced and rather fortunate combination.

Finally, I appreciate Washington University and the Department of Physics for providing a beautiful campus and excellent infrastructure.

Xingrui Song

Washington University in St. Louis

May 2025

ABSTRACT OF THE DISSERTATION

Entanglement-Enhanced Metrology With Superconducting Circuits

by

Xingrui Song

Doctor of Philosophy in Physics

Department of Physics

Washington University in St. Louis, 2025

Professor Kater W. Murch, Chair

Circuit quantum electrodynamics provides a unique platform for investigating fundamental physics and practical quantum applications. In this thesis, I introduce the superconducting circuit platform from a foundational perspective. Drawing inspiration from quantum electrodynamics and utilizing the analog of closed time-like curves, this work achieves quantum enhancement over classical strategies. Specifically, I investigate the agnostic phase estimation protocol and the associated approaches that leverage quantum entanglement to optimally estimate an unknown rotation angle without requiring prior knowledge of the rotation axis. This work not only demonstrates a proof of concept for a type of entanglement-assisted metrology but also highlights intriguing quantum effects. To establish the theoretical framework, I include a pedagogical introduction to quantum and classical Fisher information - the key concepts we utilize for quantifying sensor performance. Finally, I detail the experimental techniques that enable the demonstration of metrological advantage, weighing the benefits of quantum enhancement against the costs of entanglement manipulation.

Chapter 1: Quantization of Superconductors

1.1 Introduction

The *electromagnetic field* and *electrical current* represent the very first instance of a gauge field and corresponding conserved flow of charge that humans have learned to engineer at the quantum level. The practice of harnessing this specie of gauge interaction with superconducting circuits is termed *circuit quantum electrodynamics (cQED)*. In terms of elementary interactions, cQED can be considered even more *fundamental* than atoms, while also *richer* than individual spins or photons, when compared with these equally popular quantum information platforms. The distinctive interplay between gauge field and matter deserves greater appreciation. Inspecting these two objects, the electromagnetic field itself is already quite pristine to work with. On the other hand, to access the intrinsic properties of electric current flowing in superconductors, strategic simplification is the approach we take.

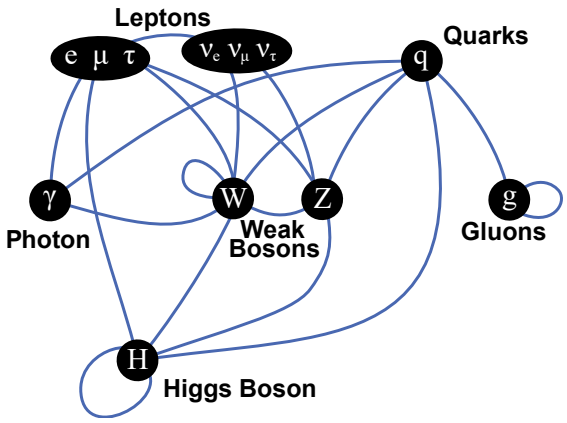

Figure 1.1: **Elementary particle interactions.** The electromagnetic interaction is mediated by photons γ. The form of electrical current most accessible to humans is carried by the ensemble of electrons e. Other types of interaction are mediated by known bosons, while the particle (quantum) nature of gravity remains elusive [1].

The purpose of this chapter is to present a tailored model of superconductors suited for cQED applications. Although various models of superconductivity exist, they are not always the most convenient for our specific needs. Below is an incomplete list of well-known approaches [2–9], loosely organized by category:

1. **Macroscopic models**: Ginzburg-Landau theory, or more generally, nonlinear Schrödinger equations. Stemming from thermodynamic considerations, these phenomenological models provide unique insights into superconductivity, especially near phase transitions.
2. **Microscopic models**: BCS theory, Bogoliubov-de-Gennes (BdG) formalism, and Gor'kov equations: derived from the many-body electronic Hamiltonian, these models provide a refined description incorporating quasiparticles.

Despite the capability of these models, our goal is to develop a *minimal* model that captures only the most essential degrees of freedom—namely, the superconducting *phase* and *charge density*—along with a small set of related variables. In fact, the *conjugacy* of phase and charge with a genuine quantum treatment of their interaction with the electromagnetic field comprises nearly all the phenomena we seek to analyze. This motivates us to search for a specialized framework. Drawing selectively from various established approaches, we assemble a minimal yet consistent model that provides a clear starting point for investigating superconducting circuits.

1.2 Lagrangian and Hamiltonian Formalisms of a Superconductor

From a phenomenological perspective, a superconductor can be regarded as a perfect fluid with negligible viscosity and thermal conductivity. Under these assumptions, there is effectively no entropy production or heat transfer within the relevant time scales, so the fluid's evolution is isentropic (adiabatic and reversible). This reversibility justifies adopting Lagrangian and Hamiltonian formalisms, eventually guiding us toward a quantized description of superconductivity. The thermal-

ization of the superconductor is also assumed to be homogeneous and far below the superconducting critical temperature, where the quasiparticle population can be neglected. As a starting point for the approximation, the fluid is dominated by a single superconducting component.

In this picture, the superconductor could be considered as a coherent ensemble of identical particles (Cooper pairs) in the condensate, each carrying energy and momentum, thus satisfying certain universal parameterization and conservation laws. We consider a general form of the Lagrangian density expressed via its variation

$$\delta\mathcal{L} = n\delta\mu - \boldsymbol{j}\cdot\delta\boldsymbol{p}, \tag{1.1}$$

where μ is the chemical potential of a Cooper pair, and $\boldsymbol{p}$ is its momentum. By treating $\mathcal{L}$ as a function of μ and $\boldsymbol{p}$, we define the derivatives

$$\begin{aligned} n &= n(\mu,\boldsymbol{p}) = \frac{\partial\mathcal{L}}{\partial\mu}, \\ \boldsymbol{j} &= \boldsymbol{j}(\mu,\boldsymbol{p}) = -\frac{\partial\mathcal{L}}{\partial\boldsymbol{p}}, \end{aligned} \tag{1.2}$$

to be the number density and the corresponding conserved current density of the Cooper pairs, respectively.

Before proceeding, let us briefly examine the dimensional consistency of these quantities. The Lagrangian density $\delta\mathcal{L}$ has the same dimension as an energy density, i.e., energy per unit volume. This is consistent with the term $n\delta\mu$, where n represents particles per volume and μ is essentially the form of energy when a particle is at rest. So, their product has the dimension of energy per volume as well.

Meanwhile, a particle's kinetic energy has units of momentum multiplied by velocity. Hence, a particle flow (number flux) $\boldsymbol{j}$ carries units of velocity per spatial volume, and multiplying that by momentum $\delta\boldsymbol{p}$ again yields an energy per volume. Taken together, these considerations confirm that each term contributing to the Lagrangian density is properly interpreted as an energy density.

We specify the Lagrangian density through the variation δ because only the differential of the Lagrangian density is physically meaningful. Adding an arbitrary constant to the Lagrangian generally does not contribute to any measurable effect.

For consistency, we require the mixed partial derivatives of $\mathcal{L}$ to commute, which yields the following conditions:

$$\begin{aligned} \frac{\partial n}{\partial \boldsymbol{p}} - \frac{\partial \boldsymbol{j}}{\partial \mu} &= 0, \\ \frac{\partial}{\partial \boldsymbol{p}} \times \boldsymbol{j} &= 0. \end{aligned} \tag{1.3}$$

These conditions guarantee the $\delta\mathcal{L}$ to be an exact differential.

Since all the variables are assumed to be dependent on the spacetime coordinates, we also introduce the covariant notation $x^\beta = (ct, \boldsymbol{x}) = (ct, x, y, z)$ [1], where the index β chooses a value from $\{0, 1, 2, 3\}$, c is the speed of light in vacuum. The differential operators are denoted as $\partial_\beta = (\partial_t/c, \nabla) = (\partial_t/c, \partial_x, \partial_y, \partial_z)$. Using this representation, we can optionally represent Eq. (1.1) in a covariant format

$$\delta\mathcal{L} = -j_\beta \delta p^\beta = -g_{\beta\gamma} j^\beta \delta p^\gamma \tag{1.4}$$

, where $j^\beta = (cn, \boldsymbol{j})$ is the four-current density and $p^\beta = (\mu/c, \boldsymbol{p})$ is the four-momentum. In the following part of the chapter, repeated indices are always implicitly summed over, unless otherwise stated. We use the Minkowski metric with matrix representation

$$g_{\beta\gamma} = g^{\beta\gamma} = \begin{pmatrix} -1 & 0 & 0 & 0 \\ 0 & 1 & 0 & 0 \\ 0 & 0 & 1 & 0 \\ 0 & 0 & 0 & 1 \end{pmatrix}. \tag{1.5}$$

The meaning of the metric is for measuring infinitesimal spacetime distance (Fig. (1.2))

$$\begin{aligned} \mathrm{d}s^2 &= g_{\beta\gamma} \mathrm{d}x^\beta \mathrm{d}x^\gamma \\ &= g_{00} \left(\mathrm{d}x^0\right)^2 + g_{11} \left(\mathrm{d}x^1\right)^2 + g_{22} \left(\mathrm{d}x^2\right)^2 + g_{33} \left(\mathrm{d}x^3\right)^2 \\ &= -c^2 \mathrm{d}t^2 + \mathrm{d}x^2 + \mathrm{d}y^2 + \mathrm{d}z^2. \end{aligned} \tag{1.6}$$

We will encounter more examples of measuring infinitesimal distances in the later chapters.

[1] Throughout this chapter, for clarity, we use Greek (Latin) alphabet as indices to label the components of 4-dimensional (3-dimensional) quantities.

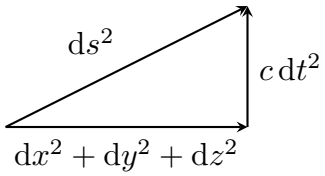

Figure 1.2: **Minkowski metric.** The minus sign in the time-like component of the metric is significant. In the triangle, the hypotenuse $\mathrm{d}s$ is *shorter* than the bottom leg $\sqrt{\mathrm{d}x^2 + \mathrm{d}y^2 + \mathrm{d}z^2}$ due to the contribution from propagation in time $c\,\mathrm{d}t$. The phenomenon is known as *length contraction* in relativity. The value of $\mathrm{d}s^2$ is positive (negative) for a space-like (time-like) interval.

The variables with lowered indices are $j_\beta = (-cn, \boldsymbol{j})$ and $p_\beta = (-\mu/c, \boldsymbol{p})$. We will occasionally adopt the covariant notations, which help us utilize the formal symmetry between temporal and spatial coordinates.

In addition to the fluid picture, a superconductor is simultaneously characterized as a wave. We further assume the superconductor admits an order parameter $\theta = \theta(t, \boldsymbol{x})$ taking values from $[-\pi, \pi]$ with the endpoints *identified* (Fig. (1.3)). The order parameter plays the role of a phase propagating in spacetime, complying with the four-momentum

$$\begin{aligned} \hbar\partial_\beta\theta &= \hbar(-\omega/c, \boldsymbol{k}) = p_\beta, \\ -\hbar\partial_t\theta &= \hbar\omega = \mu, \\ \hbar\nabla\theta &= \hbar\boldsymbol{k} = \boldsymbol{p}, \end{aligned} \tag{1.7}$$

where $\hbar$ is the reduced Planck constant. We write down the Lagrangian density and action using θ as the field variable

$$\begin{aligned} \delta\mathcal{L}(\theta) &= -\hbar j^\beta\partial_\beta\delta\theta, \\ \delta S[\theta] &= \int \mathrm{d}^4x\,\delta\mathcal{L} = -\hbar\int \mathrm{d}^4x\,(n\partial_t\delta\theta + \boldsymbol{j}\cdot\nabla\delta\theta), \end{aligned} \tag{1.8}$$

where the square bracket in $S[\theta]$ is a convention for emphasizing the action is a *functional* which maps a function $\theta(x)$ to a number.

The wave picture and the fluid picture unify when we calculate the equation of motion by

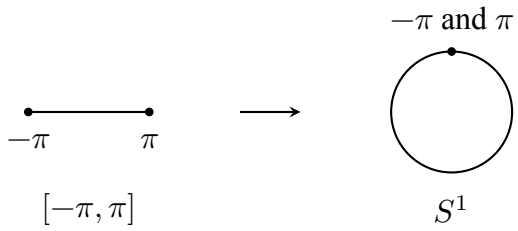

$$[-\pi, \pi]/\{-\pi, \pi\} = S^1$$

Figure 1.3: **Identifying endpoints of a line segment.** The topology of the line segment is changed. Identifying points is a topological operation of gluing together points. Also known as the quotient topology. We will encounter more examples of identifying points in a manifold in the later chapters. We emphasize that the topology of the space in which the order parameter is defined is important in two ways: (1) it defines the correct quantum mechanical boundary conditions for the allowed states. In particular, such a periodic boundary condition prescribes a discretized conjugate momentum. In other words, the integer nature of charge. (2) It emphasizes the importance of gauge symmetry in quantum mechanics since each point on the circle is placed on an equal footing.

evaluating the action principle

$$\begin{aligned} 0 &= \delta S[\theta] \\ &= \hbar \int \mathrm{d}^4x \, (\partial_t n + \nabla \cdot \boldsymbol{j}) \delta\theta - \hbar \int d^4x \partial_\beta (j^\beta \delta\theta), \end{aligned} \tag{1.9}$$

for arbitrary variation $\delta\theta$, where the second term is a vanishing surface if $j^\beta = 0$ on the integration boundary. For simplicity, we assume no current entering or escaping the superconductor, and vanishing initial and final charge distribution. In this case, the equation of motion is simply the continuity equation expressing the conservation of the number of Cooper pairs

$$\partial_t n + \nabla \cdot \boldsymbol{j} = 0, \tag{1.10}$$

which turns out to be also a wave equation for θ in the later section.

The unification of the two pictures becomes more explicit when we consider the kinetics of a Cooper pair

$$\partial_t \boldsymbol{p} + \nabla \mu = 0, \tag{1.11}$$

which can be understood as the gradient of chemical potential induces acceleration of the Cooper pair following Newton's second law, being derived by commuting ∂_t and ∇ acting on the phase θ.

We also conclude that the momentum field is irrotational

$$\nabla \times \boldsymbol{p} = 0. \tag{1.12}$$

We calculate the canonical momentum of θ

$$\frac{\partial \mathcal{L}}{\partial(\partial_t \theta)} = -\hbar n, \tag{1.13}$$

which leads to the With the Hamiltonian density given by the Legendre transform

$$\begin{aligned} \delta\mathcal{H}(\theta) &= -\hbar\delta(n\partial_t\theta) - \delta\mathcal{L}(\theta) \\ &= \delta(n\mu) - \delta\mathcal{L}(\theta) \\ &= \mu\delta n + \boldsymbol{j}\cdot\delta\boldsymbol{p} \\ &= \mu\delta n - \hbar(\nabla\cdot\boldsymbol{j})\delta\theta \end{aligned} \tag{1.14}$$

The Hamilton equations of motion are

$$\begin{aligned} \partial_t\theta &= -\frac{1}{\hbar}\frac{\partial\mathcal{H}}{\partial n(\boldsymbol{x})} = -\frac{\mu}{\hbar}, \\ \partial_t n &= \frac{1}{\hbar}\frac{\partial\mathcal{H}}{\partial\theta(\boldsymbol{x})} = -\nabla\cdot\boldsymbol{j} \end{aligned} \tag{1.15}$$

We proceed with the canonical quantized description by writing the commutation relation for the operators

$$[\theta(\boldsymbol{x}), n(\boldsymbol{x}')] = -i\delta^{(3)}(\boldsymbol{x}-\boldsymbol{x}'), \tag{1.16}$$

where $\delta^{(3)}(\boldsymbol{x})$ is the Dirac delta function in the spatial dimensions. The above commutation relation could be applied to the analysis of lumped element circuits, as we will encounter in the later chapters.

1.3 Quantization along a Spacetime Loop

In addition to the canonical quantization scheme, superconductors exhibit another curious quantized feature, which is the action along a loop in spacetime.

$$S_{\text{loop}} = \oint \mathrm{d}x^\beta\, p_\beta = \hbar \oint \mathrm{d}\theta = mh, \tag{1.17}$$

where m is an integer and $h = 2\pi\hbar$ is the Planck constant, also aknown as the *quantum of action*. While the loop can be chosen as an arbitrary closed curve within the superconducting material in spacetime, the particular meaningful case is when the curve is associated with the physical movement of a piece of superconducting material subject to the limitation of the speed of light in the vacuum, which travels along a time-like curve. It could be understood as a single piece of superconductor breaking apart, experiencing individual evolution, and recombining later. Joining the trajectory of the pieces together, we obtain a *closed time-like curve (CTC)* in spacetime [10–16].

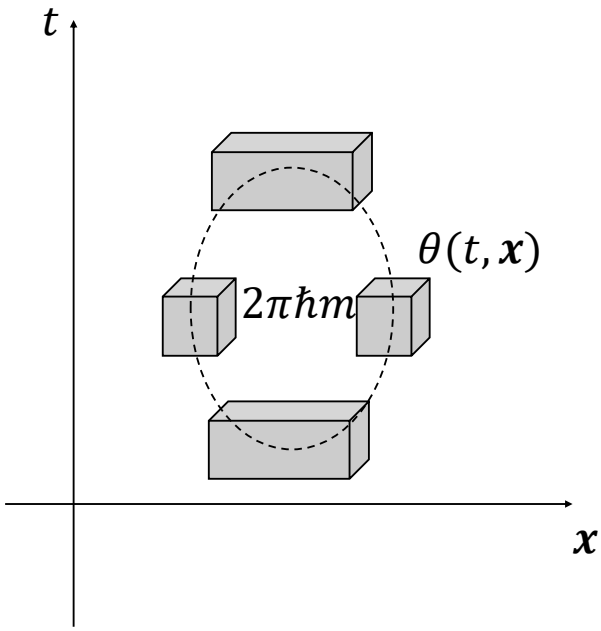

Figure 1.4: Quantization along a spacetime loop.

Or it could be interpreted as the temporary loss of superconductivity in part of the superconductor, causing a phase slip. In either case, no matter how complicated the individual evolution of the two pieces undergoes, the integral is constrained to be an integer.

The meaning of this integer is associated with the number of four-dimensional flux quanta enclosed in the closed spacetime loop. In the case that the system is in a steady state, such a phenomenon is recognized as the usual quantization of magnetic flux. We will explore the details by considering the coupling between the superconductor and an electromagnetic field.

The above equation reminds us of the old quantum condition, also known as *Bohr–Sommerfeld rule* [17, 18]

$$\oint_{H(q,p)=E} = p_i dq_i = m_i h, \quad (\text{Not summing over } i) \tag{1.18}$$

where the integration contour is defined over one period of the motion of constant energy E and m_i is an integer assigned to each pair of canonical coordinates. Despite the visual similarity, the Bohr–Sommerfeld rule is valid only via the *WKB approximation*, while our quantization condition appears to be *exact* for a superconductor.

1.4 Lagrangian and Hamiltonian Formalisms of Electromagnetic Field

We work with low fields where the difference between type-I and type-II superconductors is negligible. Quantization of a gauge field is a non-trivial job, in general. There exist general approaches like the BRST quantization for the quantization of a general system with gauge symmetry [19, 20]. For the electromagnetic field, simpler methods exist, and it is useful to demonstrate one working solution explicitly. Throughout this section, we adopt the temporal gauge

$$\begin{aligned} \varphi &= 0, \\ A^\beta &= (0, \boldsymbol{A}), \\ \boldsymbol{E} &= -\partial_t \boldsymbol{A}, \\ \boldsymbol{B} &= \nabla \times \boldsymbol{A} \end{aligned} \tag{1.19}$$

Under the temporal gauge, the last two equations can be regarded as the definition of $\boldsymbol{E}$ and $\boldsymbol{B}$, with which the following two equations are immediately satisfied

$$\nabla \cdot \boldsymbol{B} = 0 \qquad (\text{Gauss's law for magnetism}) \tag{1.20}$$

$$\nabla \times \boldsymbol{E} = -\partial_t \boldsymbol{B} \qquad (\text{Faraday's law of induction}) \tag{1.21}$$

The Lagrangian density

$$\begin{aligned}\delta\mathcal{L}(\boldsymbol{A}) &= \boldsymbol{D}\cdot\delta\boldsymbol{E} - \boldsymbol{H}\cdot\delta\boldsymbol{B} + \boldsymbol{J}\cdot\delta\boldsymbol{A} \\ &= -\boldsymbol{D}\cdot\partial_t\delta\boldsymbol{A} - \boldsymbol{H}\cdot\nabla\times\delta\boldsymbol{A} + \boldsymbol{J}\cdot\delta\boldsymbol{A},\end{aligned} \tag{1.22}$$

where $\boldsymbol{J}$ is the current density of the free charge, here treated as a fixed function. Evaluating the action principle

$$\begin{aligned}0 &= \delta S[\boldsymbol{A}] \\ &= \int d^4x(\partial_t\boldsymbol{D} - \nabla\times\boldsymbol{H} + \boldsymbol{J})\cdot\delta\boldsymbol{A} - \int d^4x\partial_t(\boldsymbol{D}\cdot\delta\boldsymbol{A}) + \int d^4x\nabla\cdot(\boldsymbol{H}\times\delta\boldsymbol{A}),\end{aligned} \tag{1.23}$$

where the last two terms vanish by assuming both $\boldsymbol{D}$ and $\boldsymbol{H}$ vanish on the corresponding boundary. The resulting equation of motion is

$$\nabla\times\boldsymbol{H} = \boldsymbol{J} + \partial_t\boldsymbol{D}. \qquad (\text{Ampère–Maxwell law}) \tag{1.24}$$

The divergence of the above equation produces

$$\nabla\cdot\partial_t\boldsymbol{D} = \partial_t\rho, \qquad (\text{Time derivative of Gauss's law}) \tag{1.25}$$

where ρ is the charge density satisfying

$$\partial_t\rho + \nabla\cdot\boldsymbol{J} = 0. \tag{1.26}$$

We additionally impose an initial condition

$$\nabla\cdot\boldsymbol{D} = \partial_t\rho, \quad t = 0 \tag{1.27}$$

Combining Eq. (1.20), (1.21), (1.24), (1.20) and (1.26), we recover the Maxwell's equations. We proceed with the Hamiltonian formalism by calculating the canonical momentum corresponding to $\boldsymbol{A}$,

$$\frac{\partial\mathcal{L}}{\partial(\partial_t\boldsymbol{A})} = -\boldsymbol{D}, \tag{1.28}$$

satisfying the canonical commutation relation

$$[A_a(\boldsymbol{x}), D_b(\boldsymbol{x}')] = -i\hbar\delta^{(3)}\delta_{ab}(\boldsymbol{x}-\boldsymbol{x}'). \tag{1.29}$$

The Hamiltonian is

$$\delta\mathcal{H}(\boldsymbol{A}) = \boldsymbol{E}\cdot\delta\boldsymbol{D} + \boldsymbol{H}\cdot\delta\boldsymbol{B} - \boldsymbol{J}\cdot\delta\boldsymbol{A} \tag{1.30}$$

1.5 Superconductor Coupled to Electromagnetic Field

We couple the superconductor with the electromagnetic field through minimal coupling. By performing the replacement

$$\nabla\theta \to \nabla\theta + \frac{2e}{\hbar}\boldsymbol{A}, \tag{1.31}$$

We distinguish the canonical momentum

$$\boldsymbol{p} = \hbar\nabla\theta, \tag{1.32}$$

which is gauge-dependent and the kinetic momenta

$$\boldsymbol{P} = \hbar\nabla\theta + 2e\boldsymbol{A} \tag{1.33}$$

where the coupling strength is set by the charge of the Cooper pair, $-2e$. The total Lagrangian density

$$\delta\mathcal{L}(\theta, \boldsymbol{A}) = -\hbar(n\partial_t\delta\theta + \boldsymbol{j}\cdot\nabla\delta\theta) - \boldsymbol{D}\cdot\partial_t\delta\boldsymbol{A} - \boldsymbol{H}\cdot\nabla\times\delta\boldsymbol{A} - 2e\boldsymbol{j}\cdot\delta\boldsymbol{A} \tag{1.34}$$

Using the action principle, we obtain the equations of motion under similar procedures and assumptions

$$\begin{aligned} \partial_t n + \nabla\cdot\boldsymbol{j} &= 0, \\ \partial_t\boldsymbol{D} - \nabla\times\boldsymbol{H} - 2e\boldsymbol{j} &= 0. \end{aligned} \tag{1.35}$$

The kinetic equation shows that the electric field accelerates the Cooper pair in addition to the chemical potential gradient.

$$\partial_t\boldsymbol{P} = -2e\boldsymbol{E} - \nabla\mu \tag{1.36}$$

and

$$\nabla\times\boldsymbol{P} = 2e\boldsymbol{B} \tag{1.37}$$

The total Hamiltonian density is

$$\delta\mathcal{H}(\theta, \boldsymbol{A}) = \mu\delta n + \boldsymbol{j}\cdot\delta\boldsymbol{P} + \boldsymbol{E}\cdot\delta\boldsymbol{D} + \boldsymbol{H}\cdot\delta\boldsymbol{B}. \tag{1.38}$$

1.6 Sigma Model for Superconductors

We consider a special case of the above framework, the $O(2)$ sigma model or, equivalently, the quantum rotor model in the continuum limit [2, 3]. As a phenomenological model, it correctly treats the linear part of kinetic inductance without the complexity involving critical temperature and critical field, making it a suitable description in the dilution refrigeration temperature with appropriate magnetic shielding. We introduce the model by evaluating the charge density. Considering a metal near the equilibrium satisfying

$$\delta n_e = \nu \delta \mu_e, \quad \delta \boldsymbol{j}_e = \rho_0 \delta \boldsymbol{v}_e = \frac{\rho_0}{m} \delta \boldsymbol{p}_e, \tag{1.39}$$

where ν represents the electronic density of states near the Fermi surface, n_e and μ_e represent the density and chemical potential of the electrons, respectively. $\boldsymbol{j}_e$ represents the flow of electrons, ρ_0 represents the density of electrons near equilibrium, m represents the effective mass of the electron, $\boldsymbol{v}_e$ and $\boldsymbol{p}_e$ represent the velocity and momentum of the electron making drift motion, respectively. Since variables for the electrons are related to those of the Cooper pairs we have

$$n = \frac{1}{2} n_e, \quad \mu = 2(\mu_e - \Delta), \quad \boldsymbol{j} = \frac{1}{2} \boldsymbol{j}_e, \quad \boldsymbol{p} = 2\boldsymbol{p}_e \tag{1.40}$$

, where Δ is the superconducting gap energy that we have assumed to be a constant, for simplicity. Using these variables, we obtain

$$\delta n = \frac{1}{4} \nu \delta \mu, \quad \delta \boldsymbol{j} = \frac{\rho_0}{4m} \delta \boldsymbol{p}. \tag{1.41}$$

The major approximation we apply in the sigma model is the *linearization* of the above equations by approximating ν, ρ_0, m to be constants near the equilibrium. The implication of the linearization will be discussed later. Under the approximation, we could integrate Eq. (1.41) to arrive at the relations

$$n = \frac{1}{4} \nu \mu, \quad \boldsymbol{j} = \frac{\rho_0}{4m} \boldsymbol{p}, \tag{1.42}$$

where in the first equation we have set the equilibrium ($\mu = 0$) to be charge-neutral ($n = 0$).

This allows us to evaluate the first term in the Lagrangian density

$$\delta\mathcal{L} = n\delta\mu - \boldsymbol{j}\cdot\delta\boldsymbol{p} = \frac{1}{4}\left(\nu\mu\delta\mu - \frac{\rho_0}{m}\boldsymbol{j}\cdot\delta\boldsymbol{p}\right) = \frac{1}{4}\delta\left(\frac{\nu}{2}\mu^2 - \frac{\rho_0}{2m}\boldsymbol{p}^2\right), \tag{1.43}$$

By using Eq. (1.7), the Lagrangian density and action of the system without electromagnetic field

$$\mathcal{L}(\theta) = \frac{\hbar^2}{4}\left[\frac{\nu}{2}(\partial_t\theta)^2 - \frac{\rho_0}{2m}(\nabla\theta)^2\right], \tag{1.44}$$

$$S[\theta] = \int dtdr^3\mathcal{L}(\theta) = \frac{\hbar^2}{4}\int dtdr^3\left[\frac{\nu}{2}(\partial_t\theta)^2 - \frac{\rho_0}{2m}(\nabla\theta)^2\right], \tag{1.45}$$

Performing variation with respect to θ, we obtain

$$\delta S[\theta] = \frac{\hbar^2}{4}\int dtdr^3\delta\theta\left(-\nu\partial_t^2 + \frac{\rho_0}{m}\nabla^2\right)\theta, \tag{1.46}$$

By enforcing the action principle $\delta S[\theta]/\delta\theta = 0$, the equation of motion we obtain is a wave equation defining the *Goldstone mode* of the superconductor [21–26]

$$\left(-\nu\partial_t^2 + \frac{\rho_0}{m}\nabla^2\right)\theta = 0, \tag{1.47}$$

By replacing $-\partial_t \to \omega, \nabla \to \boldsymbol{k}$, we obtain the linear dispersion relation

$$\omega = \pm v|\boldsymbol{k}|, \tag{1.48}$$

where the velocity v of the propagation is the Fermi velocity given by

$$v = \left|\frac{\partial\omega}{\partial\boldsymbol{k}}\right| = \sqrt{\frac{\rho_0}{m\nu}}. \tag{1.49}$$

While the Goldstone mode is massless, featuring a linear dispersion relation, in reality, the mode does not individually exist because of the strong coupling with the electromagnetic field. In order to see the effect, we write down the coupled Lagrangian density. The free electromagnetic field in a dielectric is described by

$$\begin{aligned}\mathcal{L}(\varphi, \boldsymbol{A}) &= \frac{\epsilon}{2}\boldsymbol{E}^2 - \frac{1}{2\mu}\boldsymbol{B}^2 \\ &= \frac{\epsilon}{2}(\nabla\varphi + \partial_t\boldsymbol{A})^2 - \frac{1}{2\mu}(\nabla\times\boldsymbol{A})^2,\end{aligned} \tag{1.50}$$

where φ is the electric potential, and $\boldsymbol{A}$ is the magnetic vector potential. We have utilized the relations

$$\begin{aligned} \boldsymbol{E} &= -\nabla\varphi - \partial_t \boldsymbol{A}, \\ \boldsymbol{B} &= \nabla \times \boldsymbol{A} \end{aligned} \tag{1.51}$$

When coupled to the electric charge

$$\mathcal{L}(\rho, \boldsymbol{J}, \varphi, \boldsymbol{A}) = -\rho\varphi + \boldsymbol{J} \cdot \boldsymbol{A} + \mathcal{L}(\varphi, \boldsymbol{A}), \tag{1.52}$$

To couple the superconductor to an electromagnetic field, we do the replacement

$$\begin{aligned} \partial_t\theta &\to \partial_t\theta - \frac{2e}{\hbar}\varphi, \\ \nabla\theta &\to \nabla\theta + \frac{2e}{\hbar}\boldsymbol{A}, \end{aligned} \tag{1.53}$$

where the coupling strength is set by the charge of a Cooper pair, $-2e$. The total Lagrangian

$$\mathcal{L}(\theta, \varphi, \boldsymbol{A}) = \frac{\hbar^2}{4}\left[\frac{\nu}{2}\left(\partial_t\theta - \frac{2e}{\hbar}\varphi\right)^2 - \frac{\rho_0}{2m}\left(\nabla\theta + \frac{2e}{\hbar}\boldsymbol{A}\right)^2\right] + \mathcal{L}(\varphi, \boldsymbol{A}) \tag{1.54}$$

Comparing these two gives us the electric charge density and current of the superconductor

$$\begin{aligned} \rho &= \frac{\hbar e\nu}{2}\left(\partial_t\theta - \frac{2e}{\hbar}\varphi\right) \\ \boldsymbol{J} &= -\frac{\hbar e\rho_0}{2m}\left(\nabla\theta + \frac{2e}{\hbar}\boldsymbol{A}\right) \end{aligned} \tag{1.55}$$

By forcing $\delta S[\theta]/\delta\theta = 0$, we obtain the equation of motion for θ, which is alternatively expressed as the continuity equation

$$\partial_t\rho + \nabla \cdot \boldsymbol{J} = 0 \tag{1.56}$$

By calculating the gradient and curl of the two equations, we recover the London equations for superconductors [27]

$$\begin{aligned} \boldsymbol{E} &= \partial_t(\Lambda\boldsymbol{J}) + \frac{1}{e^2\nu}\nabla\rho \approx \partial_t(\Lambda\boldsymbol{J}), \\ \nabla \times (\Lambda\boldsymbol{J}) &= -\boldsymbol{B}, \end{aligned} \tag{1.57}$$

where the phenomenological parameter Λ is given by

$$\Lambda = \frac{m}{e^2\rho_0} = \frac{m^*}{n^*(q^*)^2}. \tag{1.58}$$

The approximation used in the first equation requires that the spatial gradient of the charge distribution is small and the density of states is large, which is usually true for metals. From the London equations, we obtain the Meisner effect. The electromagnetic field follows exponential decay inside a superconductor with characteristic length λ_L. Inside a superconductor, we may assume both ρ and $\boldsymbol{J}$ vanish. From the equation, we see that the electric potential integrated over time, which has the same dimension as a magnetic flux, is also quantized. The change of this value can be a result of a temporary loss of superconductivity or a phase slip through a Josephson junction. After the superconductivity is recovered, the jump only takes an integer value.

1.6.1 Electron-hole Symmetry

In the sigma model, we linearize the relation between charge and phase (Eq. (1.42)). As a result, the system respects charge conjugation symmetry

$$\theta \to -\theta, \quad \mathcal{L} \to \mathcal{L} \tag{1.59}$$

The Lagrangian of the system is invariant under charge conjugation. It is a reasonably good symmetry approximation for superconducting metals with a large density of states. The Hamiltonian exhibits the same electron-hole symmetry inherent from the Lagrangian

$$\theta \to -\theta, \quad n \to -n, \quad \mathcal{H} \to \mathcal{H} \tag{1.60}$$

In chapter four, we utilize this symmetry to construct the electron-hole symmetry of a superconducting transmon qubit. The electron-hole symmetry is employed to define a sensing protocol called the *positronium sensing*.

1.7 Summary

Our agnostic phase estimation protocol, discussed in later chapters, could be described as a generalization of this quantization phenomenon to include more complicated parameter space in addition to a single phase θ, which encodes the information of a qubit.

The interplay of phase and gauge is important because it gives us the hint that quantum mechanics does not live in a flat space, everything is intrinsically *curved*. Even if we are not directly dealing with a gauge field, similar effects will be encountered in the next chapter.

Chapter 2: Agnostic Sensing with Superconducting Qubits

2.1 Introduction

In this chapter, we discuss the concept of agnostic sensing, a protocol designed to estimate an unknown rotation angle α without requiring prior knowledge of the rotation axis $\hat{\boldsymbol{n}}$. To introduce the idea, we draw inspiration from the anecdote of *Richard Feynman* and *John Wheeler*, who explored the notion that an electron traveling forward in time is effectively indistinguishable from a positron traveling backward in time.

Building on this time-reversal symmetry perspective, we show how entanglement is related to the so-called *closed time-like curves*. Specifically, we harness the power of entangled superconducting qubits to implement novel sensing protocols that circumvents the need to align the sensor concerning an unknown rotation axis. We begin by briefly revisiting the historical context and ideas from quantum electrodynamics (QED). We then show how the concepts can be translated into cQED setting, leading to metrological advantage.

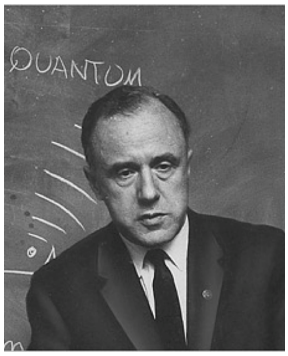

(a) **John Wheeler**

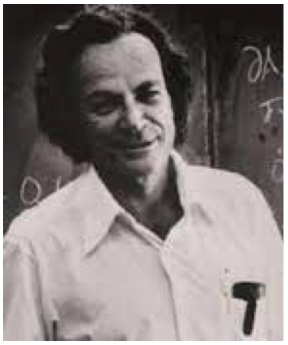

(b) **Richard Feynman**

Figure 2.1

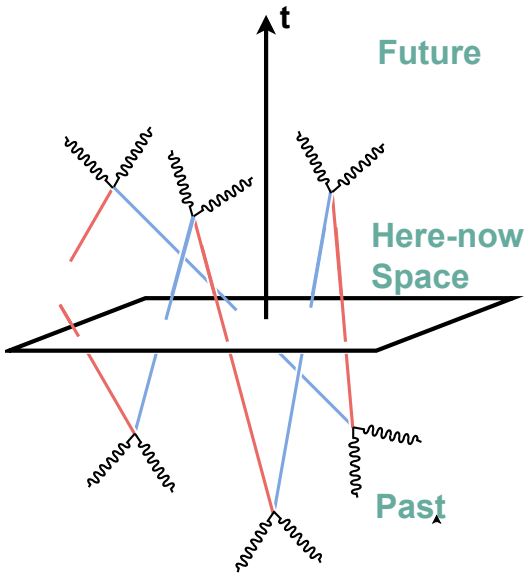

Figure 2.2: **One electron universe.** Each red (blue) solid line represents an electron (positron) traveling forward (backward) in time. Wavy lines represent photons. Each joint of solid lines and wavy lines represents a pair production or pair annihilation event.

2.2 One-Electron Universe and Quantum Electrodynamics

2.2.1 Wheeler's Phone Call to Feynman

Here is the story according to Feynman [28]:

> I received a telephone call one day at the graduate college at Princeton from Professor Wheeler, in which he said, "Feynman, I know why all electrons have the same charge and the same mass" "Why?" "Because, they are all the same electron!"

Although the one-electron universe hypothesis was not polished at that time, the ingredients were later integrated into Feynman's approach to QED. One of the key ideas: the kinematics of particles respects time symmetry.

2.2.2 Feynman Propagators and Diagrams

A textbook for a comprehensive treatment of quantum field theory is recommended [20, 29]. But the basic idea is simple. We represent the vacuum state as $|0\rangle$. A Fermion can be added to a quantum state, for example,

$$\bar{\psi}(y)\,|0\rangle \tag{2.1}$$

represents the quantum state with one Fermion created at the spacetime coordinate y, with the first component y^0 labeling the time of its creation. For simplicity, we have suppressed the spinor indices associated with the Fermion. A Fermion can also be removed from a quantum state. For example

$$\psi(x)\bar{\psi}(y)\,|0\rangle \tag{2.2}$$

represents the removal of a Fermion at spacetime coordinate x, following its creation, where $\bar{\psi} = \psi^\dagger\gamma^0$ is the Dirac adjoint of ψ and γ^0 is the time-like Dirac matrix. We may make the assumption that the Fermion is created before being removed, which translates to $x^0 > y^0$. The ordering of the Fermionic operators ψ and $\bar{\psi}$ is important because they do not commute with each other. The operator to the *right* is always applied first.

This quantum state can be projected back to the vacuum state to produce a probability amplitude

$$S_F(x-y) = \langle 0|\psi(x)\bar{\psi}(y)|0\rangle\,, \quad (x^0 > y^0), \tag{2.3}$$

which defines the Feynman propagator of a Fermion traveling from y to x. Now, what happens if we let a particle travel backward in time? In other words, we are attempting to remove a particle before its creation. Following the previous reasoning, we write down the expression

$$S_F(x-y) = -\langle 0|\bar{\psi}(y)\psi(x)|0\rangle\,, \quad (x^0 < y^0), \tag{2.4}$$

where a minus sign is added due to the Fermionic statistics when the two operators are exchanged. The meaning of the expression can be intuitively understood as: by attempting to remove a Fermion from the vacuum, we created an anti-Fermion at x

$$\psi(x)\,|0\rangle\,. \tag{2.5}$$

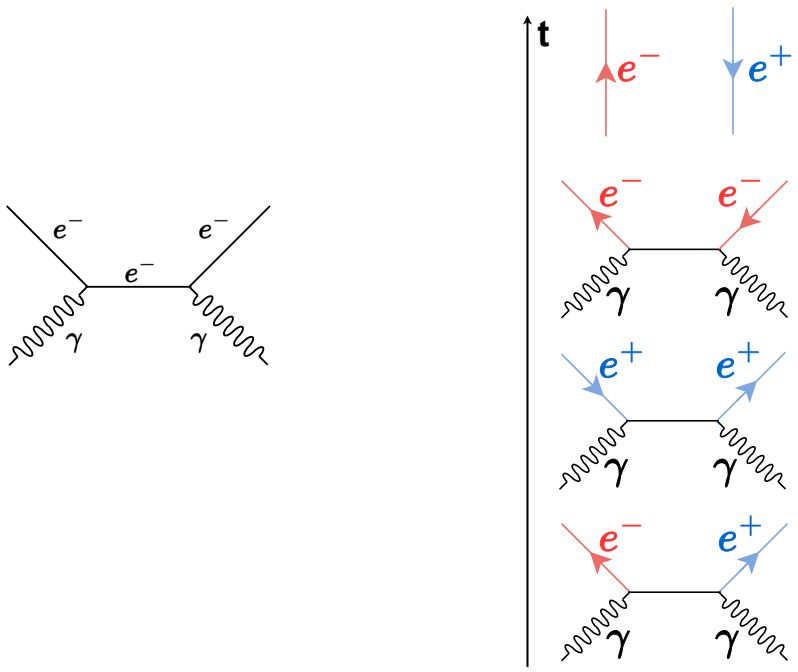

(a) (b)

Figure 2.3: **Feynman diagrams.** (a) Feynman diagram of the Breit-Wheeler pair production without labeling the direction on the electron/positron propagators. (b) Three different interpretations of the same pair production process. Unlike conventional Feynman diagrams where the arrows represent the movement of charge, here, the arrows represent the movement of the particle (electron or positron), for the purpose of clarity. In this figure three possible interpretations of the same Feynman diagram appear different.

Based on this interpretation, Eq. (2.4) describes the propagation of an anti-Fermion from x to y. Combining these two, we arrive at the full definition of the Feynman propagator

$$S_F(x-y) = \langle 0|T\psi(x)\bar{\psi}(y)|0\rangle \,, \tag{2.6}$$

where T is the time-ordering operator. On the left-hand side, the particle physics represented by the Feynman propagator is always meaningful regardless of the relation between x^0 and y^0. On the right-hand side, the picture is more aligned with one's intuition. No matter whether the excitation is a Fermion or an Anti-Fermion, it always propagates forward in time. However, the two descriptions are both correct and equivalent.

Although the construction looks bizarre, built on top of these propagators, QED is a remarkably

accurate theory, which has been experimentally examined down to the 10^{-9} level [30, 31].

Feynman's Nobel Prize-winning work on QED introduced Feynman diagrams to describe interactions between electrons and photons. Each line in a Feynman diagram represents a Feynman propagator, which remains valid under changes of reference frame. In particular, an electron traveling forward in time can be reinterpreted as a positron traveling backward in time. This interchangeability lays the conceptual foundation for thinking of processes as flexible in their arrow of time.

2.3 Closed Time-like Curve

One step further, by connecting the worldline of an electron and a positron, we create an object called *closed time-like curve*. Similar to the ideas discussed in the first chapter, in the context of superconductors.

The reason the electron and positron can be regarded as the same electron traveling in the spacetime is that they are *entangled*. This quantum entanglement comes from the conservation laws. The entanglement involves the linear momenta, orbital angular momenta, and spin angular momenta of the particles. To capture the essence of the process, we focus on the *simplest* case where all spatial degrees of freedom are neglected, only considering the entanglement in the spins. Specifically, in the simple case where two photons are involved, the *Landau–Yang theorem* guarantees that the electron and positron have to be generated in zero total angular momentum [32, 33]. Ignoring the contribution from the orbital part, this implies the generation of a *singlet state*. An example of such a singlet generation process is the *(linear) Breit-Wheeler process* near the energy threshold, with two incident beams of γ-photons both left or right circularly polarized [34].

While high-energy experiments have so far provided only partial evidence for the Breit–Wheeler process [35, 36], we simplify this challenge by adopting an alternative approach to explore its underlying physics. In our experimental work [37], which builds on the protocol of Ref. , we encode the spins of two entangled particles into superconducting transmon qubits, forming the basis for

our experimental investigation. Prior optical experiments have examined the relationship between entanglement manipulation and closed timelike curves [38, 39], and delayed-choice quantum erasure experiments bear conceptual similarities to our protocol [40, 41]. However, metrological protocols inspired by closed timelike curves have not yet been demonstrated experimentally. Before proceeding further, we introduce a diagrammatic representation of entangled states, providing intuitive clarity for working with such quantum systems.

2.4 Diagrammatic Representation of Quantum Entanglement

The creation of an entangled pair is represented by a cup shape. The measurement in projecting into the entangled state is represented by a cap shape.

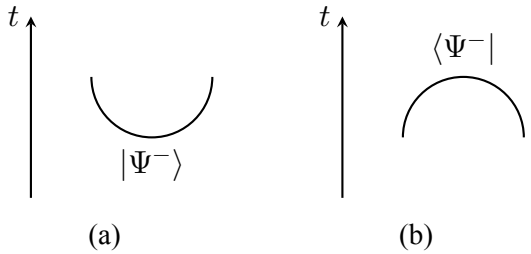

Figure 2.4: **Cup and cap.** (a) A cup represents a pair of qubits in an entangled state. (b) A cap represents a projective measurement collapsing the quantum state into an entangled state.

2.4.1 A Simple Example

Here is a simple example of connecting a cup with a projective measurement.

By connecting a cup with a projective measurement, we allow the eigenstate of the measurement basis to propagate backward in time and determine the initial state of the other qubit in the same entangled pair. The exact initial state of the qubit depends on the measurement outcome and the type of entangled state.

Later, we will analyze this setup in the case that the entangled state is a singlet state, which will be important for our protocols.

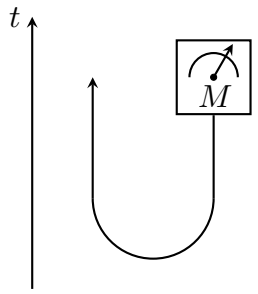

Figure 2.5: **Connecting cup with measurement.**

2.4.2 Quantum Teleportation

By connecting a cup with a cap, we obtain the well-known protocol for *quantum teleportation* [42, 43].

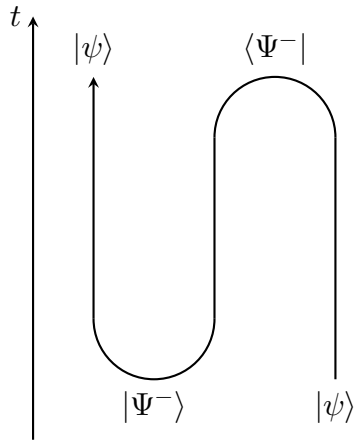

Figure 2.6: **Quantum teleportation.** (a) By connecting a cup with a cap, we obtain the protocol for quantum teleportation.

Note that for the quantum teleportation protocol to work, classical communication of two bits is required. If classical communication is prohibited, $1/4$ of the chance that the correct quantum state will be teleported. The ensemble of the $1/4$ correct teleported state and $3/4$ wrong states is equivalent to a maximally mixed state. This reminds us of the probabilistic nature of the scattering events in QED. We'll come back to this problem later.

Now that we have finished with the entanglement part, we are moving on with *quantum sensing* part by introducing the single qubit sensor.

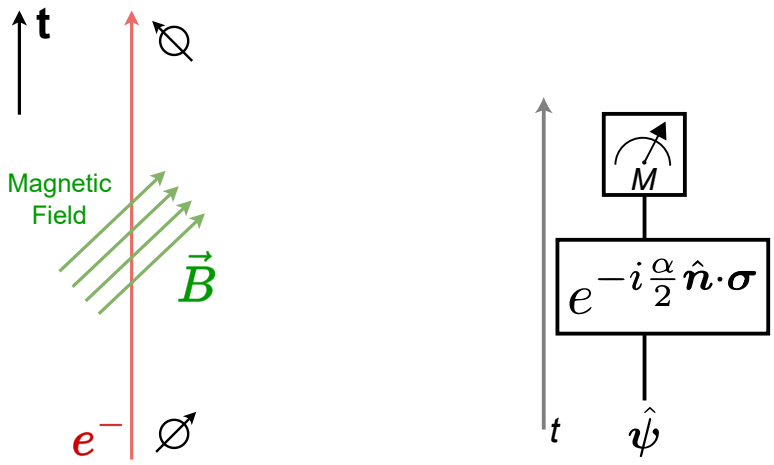

(a) (b)

Figure 2.7: **Single-qubit sensing protocol.** (a) Single-electron spin as a sensor for the magnetic field. The electron spin is altered after interacting with the unknown magnetic field. From the change of the spin, we could extract information regarding the magnetic field. (b) The single-electron sensor can be abstracted as a qubit applied with an unknown rotation and a projective measurement. This is the single-qubit sensing protocol.

2.5 Circuit QED and the Single-qubit Sensor

Superconducting transmon qubits coupled to resonators allow researchers to engineer interactions reminiscent of QED, but on energy scales and physical sizes that are manageable in a typical laboratory.

2.5.1 Single-Qubit Sensing Protocol

As a starting point, consider a single qubit used for parameter estimation. Conceptually, one can imagine the sensor is an electron. We let the electron interact with an unknown magnetic field. The electron spin will be rotated. The amount of rotation encodes the information about the magnetic field. The schematic is shown in Fig. (2.7a).

Translating the elements into a protocol described by qubit states and rotation operators (Fig. (2.7b)), the general workflow consists of three steps:

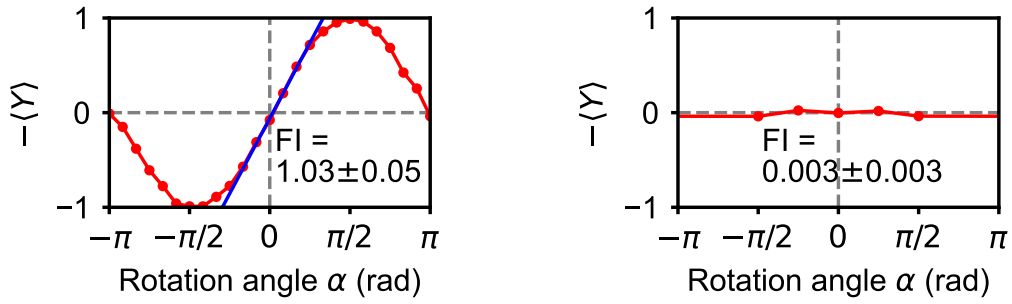

(a) (b)

Figure 2.8: **Deficiency of single qubit sensor.** (a) Maximum contrast is observed when the rotation is along the $\hat{z}$-axis. (b) Vanishing contrast is observed when the rotation is along the $\hat{x}$-axis. We will define the Fisher information in the next section.

1. **State Preparation**: Initialize the qubit in a known state, such as

$$|x+\rangle \;=\; \frac{1}{\sqrt{2}}(|0\rangle + |1\rangle).$$

2. **Unknown rotation**: Evolve the qubit with a rotation around an axis $\hat{\boldsymbol{n}}$ by an angle α:

$$U(\alpha) = \mathrm{e}^{-\mathrm{i}\alpha\hat{\boldsymbol{n}}\cdot\boldsymbol{\sigma}/2} \tag{2.7}$$

3. **Measurement**: Measure in a suitable basis to estimate α.

However, the single-qubit approach works well if one already knows $\hat{\boldsymbol{n}}$. If $\hat{\boldsymbol{n}}$ is unknown, the initial state choice can become suboptimal. Despite the measurement being performed on the correct basis, in our case, it is the Y basis, and depending on the rotation axis, the sensitivity varies. Figures show the best and the worst-case scenarios that one would expect for a single qubit sensor. In the best case, the rotation axis is perpendicular to the initial state, which produces maximum contrast (Fig. (2.8a)).

In order to quantitatively analyze the sensitivity of a sensor, in the next two sections, we introduce the concepts of quantum and classical *Fisher information* and the associated *Cramér–Rao Bound* [44, 45].

2.6 Quantum and Classical Fisher Information

This section does not aim for a rigorous derivation but rather aims for a geometric approach emphasizing intuitive understanding. For simplicity, we limit our discussion to pure states and projective measurements. The important aspect to understand Fisher information we take is to consider measuring the distance between quantum states.

Quantum states are vectors in the *Hilbert space*

$$|\psi\rangle = \sum_i c_i \, |i\rangle \, , \tag{2.8}$$

with complex numbers $c_i = a_i + \mathrm{i}\, b_i$. For an N-level system, the index i chooses an integer value from 1 to $N-1$. Combining the real and imaginary components, the Hilbert space can be considered as a $2N$-dimensional manifold. The Hilbert space is equipped with an inner product, which provides a natural way to calculate the length of a vector

$$l^2 = 4||\psi\rangle|^2 = 4\,\langle\psi|\psi\rangle = 4\sum_i |c_i|^2 = 4\sum_i (a_i^2 + b_i^2), \tag{2.9}$$

where 4 is a scaling factor added for convenience.

The simplest way to compare two states is to calculate the difference between them and get the length of the difference. This motivates us to define the prototype of the distance between two states as

$$\Delta l^2 = 4||\psi\rangle - |\phi\rangle|^2. \tag{2.10}$$

Distance is a useful concept because it allows us to quantify how different two states are. From the above expression, we obtain the prototype of an infinitesimal distance between quantum states

$$\mathrm{d}l^2 = 4\,\langle \mathrm{d}\psi|\mathrm{d}\psi\rangle \, . \tag{2.11}$$

However, the distance defined above is too coarse and includes certain nonphysical effects. In order to understand the problem, we take a deeper look at the Hilbert space. To work with physically meaningful states only, we need to impose the normalization condition $\langle\psi|\psi\rangle = 1$. In other words,

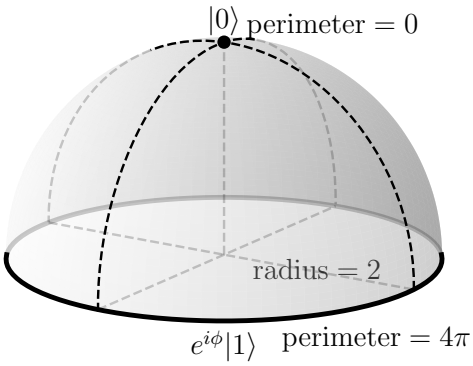

Figure 2.9: **Bloch sphere with the incorrect metric.** The metric given by dl^2 in Eq. (2.14) corresponds to the upper hemisphere of radius 2. The state $|0\rangle$ appears as a single point with zero length, while the state $|1\rangle$ appears as a circle with a perimeter of 4π. Though the metric here shows up as the incorrect option for the Bloch sphere, we will encounter the same metric in the next chapter when we discuss the two-qubit maximally entangled states.

the quantum states live on a $(2N-1)$-dimensional sphere. In addition to the normalization condition, the quantum state has a free global phase. The topological operation for removing these two extra degrees of freedom is making all quantum states that are proportional to the same representative quantum state $|\psi\rangle$ *identified*. Namely, the states

$$|\psi_\lambda\rangle = \lambda\,|\psi\rangle\,, \tag{2.12}$$

with some complex numbers λ are regarded as the same state as $|\psi\rangle$, like gluing them into a single point. The collection of such representative states $\{|\psi\rangle\}$ forms the *projective Hilbert space*.

The most familiar example of a projective Hilbert state is the *Bloch sphere* [43]. We consider the single-qubit representative quantum states

$$|\psi\rangle = \cos\frac{\theta}{2}\,|0\rangle + e^{\,\mathrm{i}\,\phi}\sin\frac{\theta}{2}\,|1\rangle\,, \tag{2.13}$$

with the differential

$$|\mathrm{d}\psi\rangle = \frac{1}{2}\left(-\sin\frac{\theta}{2}\,|0\rangle + \mathrm{e}^{\,\mathrm{i}\,\phi}\cos\frac{\theta}{2}\,|1\rangle\right)\mathrm{d}\theta + \,\mathrm{i}\,\mathrm{e}^{\,\mathrm{i}\,\phi}\sin\frac{\theta}{2}\,|1\rangle\,\mathrm{d}\phi. \tag{2.14}$$

The infinitesimal distance is written as

$$\mathrm{d}l^2 = 4\,\langle\mathrm{d}\psi|\mathrm{d}\psi\rangle = \mathrm{d}\theta^2 + 4\sin^2\frac{\theta}{2}\,\mathrm{d}\phi^2. \tag{2.15}$$

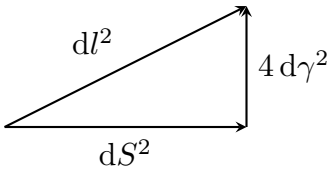

Figure 2.10: **Metric in the projective Hilbert space.** In the triangle, the hypotenuse $\mathrm{d}l$ is *longer* than the bottom leg $\mathrm{d}S$ due to the contribution from the geometric phase $2\,\mathrm{d}\gamma$. The metric $\mathrm{d}S^2$ is also known as (4 times of) the *Fubini-Study metric* [46]. Despite the curious visual similarity with the Minkowski metric Eq. (1.6) in the minus sign, we need to be cautious because here $\mathrm{d}S^2$ given by Eq. (2.19) is positive definite.

However, the metric defined by Eq. (2.15) appears to be incorrect. One way to see the problem is to calculate the perimeter of the circles of constant latitude.

$$l = \int_{-\pi}^{\pi} 2\sin\frac{\theta}{2}\,\mathrm{d}\phi = 4\pi\sin\frac{\theta}{2}. \tag{2.16}$$

At the north pole, $\theta = 0$, l shrinks to 0, as expected. However, at the south "pole" where $\theta = \pi$, we have $l = 4\pi$. The geometry faithfully respects this wrong metric would be a hemisphere with a radius of 2 (Fig. (2.9)).

The problem is that when we are transporting the quantum state on the Bloch sphere, the attached phase is also evolving. This is the *geometric phase* [46, 47]

$$\begin{aligned} \mathrm{d}\gamma &= \mathrm{i}\,\langle\psi|\mathrm{d}\psi\rangle \\ &= \mathcal{A}_\theta\,\mathrm{d}\theta + \mathcal{A}_\phi\,\mathrm{d}\phi, \end{aligned} \tag{2.17}$$

where

$$\begin{aligned} \mathcal{A}_\theta &= \mathrm{i}\,\langle\psi|\partial_\theta\psi\rangle = 0, \\ \mathcal{A}_\phi &= \mathrm{i}\,\langle\psi|\partial_\phi\psi\rangle = \sin^2\frac{\theta}{2}, \end{aligned} \tag{2.18}$$

are the components of the *Berry connection* [46]. The value of the Berry connection is dependent on the choice of the representative quantum states, also known as the *gauge dependence*.

Since the change in the global phase does not generate a physically measurable effect, we need to subtract the contribution from the geometric phase

$$\mathrm{d}S^2 = \mathrm{d}l^2 - 4\,\mathrm{d}\gamma^2 = 4(\langle\mathrm{d}\psi|\mathrm{d}\psi\rangle - |\langle\psi|\mathrm{d}\psi\rangle|^2). \tag{2.19}$$

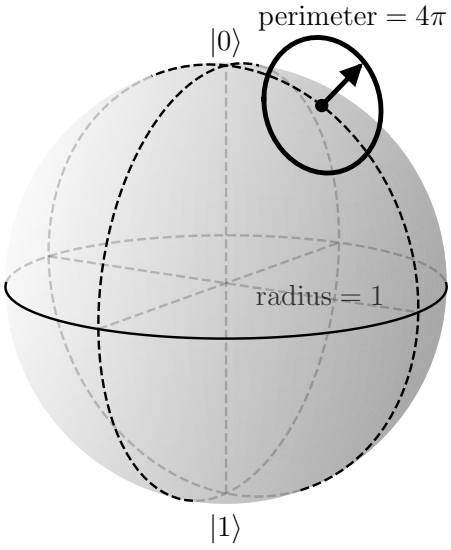

Figure 2.11: **Bloch sphere.** Each quantum state of a single qubit is mapped to a point on a unit sphere. Every point on the sphere is attached with a circle of perimeter 4π encoding the global phase of the qubit (the size is not up to scale in the figure). The fact that a 4π-rotation is needed to recover the qubit in its original global phase is a property of the spin-$1/2$ structure. The combination of the Bloch sphere and the circles in this setting is homeomorphic to S^3, a geometric mapping known as the *Hopf fibration*. S^3 with each of these circles identified as a single point produces the Bloch sphere.

For a qubit, we have

$$\mathrm{d}S^2 = \mathrm{d}\theta^2 + 4\left(\sin^2\frac{\theta}{2} - \sin^4\frac{\theta}{2}\right)\mathrm{d}\phi^2 = \mathrm{d}\theta^2 + \sin^2\theta\,\mathrm{d}\phi^2, \tag{2.20}$$

which is the usual metric on a unit sphere.

We connect the geometric concepts with classical probability distribution with a set of angles $0 \leq \theta_i \leq \pi$,

$$P_i = |\langle i|\psi\rangle|^2 = \cos^2\frac{\theta_i}{2} = \frac{1}{2}(1+\cos\theta_i). \tag{2.21}$$

Geometrically, these angles are given by the length of the shortest path connecting $|\psi\rangle$ and $|i\rangle$. These paths are also called the *geodesics*. The geodesics in the projective Hilbert space are arcs cut from the great circles, which makes the calculation of the length particularly easy. Although the projective Hilbert space is not a sphere, in general, we could use the Bloch sphere to demonstrate the idea. Two states separated by an arc length equal to π are orthogonal to each other.

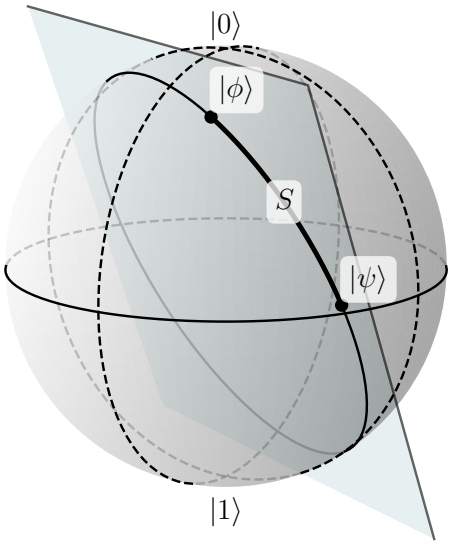

Figure 2.12: **Geodesic on the Bloch sphere.** Geodesics are special kinds of trajectories on a manifold. On the Bloch sphere, a geodesic is the great circle with 2π perimeter. For any two distinct states $|\psi\rangle$ and $|\phi\rangle$, there is a unique great circle passing through both of them. The length of the minor arc connecting them defines their distance S from each other. Generally, by reading the length of the trajectories, the value of the quantum Fisher information can be obtained. Particularly, the trajectories with maximal quantum Fisher information are the geodesics.

These angles satisfy the constraint,

$$1 = \sum_i P_i = \sum_i \cos^2 \frac{\theta_i}{2} = \frac{1}{2} \sum_i (1 + \cos \theta_i). \tag{2.22}$$

Differentiating the above expression gives us the constraint on the infinitesimal changes,

$$\sum_i \sin \theta_i \, \mathrm{d}\theta_i = 0. \tag{2.23}$$

The quantum state has the general form

$$|\psi\rangle = \sum_i e^{\,\mathrm{i}\,\phi_i} \cos \frac{\theta_i}{2} \, |i\rangle \,, \tag{2.24}$$

with the differential

$$|\mathrm{d}\psi\rangle = \sum_i \left(-\frac{1}{2} \sin \frac{\theta_i}{2} d\theta_i + \mathrm{i} \cos \frac{\theta_i}{2} d\phi_i \right) e^{\,\mathrm{i}\,\phi_i} \, |i\rangle \,. \tag{2.25}$$

We proceed with calculating the distances

$$\begin{aligned} \mathrm{d}l^2 &= 4||\mathrm{d}\psi\rangle|^2 \\ &= \sum_i \sin^2\frac{\theta_i}{2}\mathrm{d}\theta_i^2 + 4\sum_i \cos^2\frac{\theta_i}{2}\mathrm{d}\phi_i^2. \end{aligned} \tag{2.26}$$

The contribution from the geometric phase

$$\begin{aligned} \mathrm{d}\gamma^2 &= |\langle\psi|\mathrm{d}\psi\rangle|^2 \\ &= \left|\sum_i \cos\frac{\theta_i}{2}\left(-\frac{1}{2}\sin\frac{\theta_i}{2}\,\mathrm{d}\theta_i + \mathrm{i}\,\cos\frac{\theta_i}{2}\,\mathrm{d}\phi_i\right)\right|^2 \\ &= \left|\sum_i \left(-\frac{1}{4}\sin\theta_i d\theta_i + \mathrm{i}\,\cos^2\frac{\theta_i}{2}\,\mathrm{d}\phi_i\right)\right|^2. \end{aligned} \tag{2.27}$$

Using Eq. (2.23)

$$\begin{aligned} \mathrm{d}\gamma^2 &= \left|\sum_i \cos^2\frac{\theta_i}{2}\mathrm{d}\phi_i\right|^2 \\ &= \left|\sum_i \left(\cos\frac{\theta_i}{2}\cdot\cos\frac{\theta_i}{2}\mathrm{d}\phi_i\right)\right|^2 \\ &\leq \left(\sum_i \cos^2\frac{\theta_i}{2}\right)\cdot\left(\sum_i \cos^2\frac{\theta_i}{2}\mathrm{d}\phi_i^2\right) \\ &= \sum_i \cos^2\frac{\theta_i}{2}\mathrm{d}\phi_i^2, \end{aligned} \tag{2.28}$$

where the upper bound is evaluated with the *Cauchy-Schwarz inequality*. The inequality is saturated only when the vectors $\cos(\theta_i/2)$ and $\cos(\theta_i/2)\,\mathrm{d}\phi_i$ are proportional, namely

$$\cos\frac{\theta_i}{2}\,\mathrm{d}\phi_i = \cos\frac{\theta_i}{2}\,\mathrm{d}\xi, \tag{2.29}$$

for some infinitesimal change in the global phase $\mathrm{d}\xi$, ruling out any contribution from the relative phases. In fact, this condition simply implies $\mathrm{d}\gamma = \mathrm{d}\xi$.

$$
\begin{aligned}
\mathrm{d}S^2 &= \mathrm{d}l^2 - 4\,\mathrm{d}\gamma^2 \\
&= \sum_i \sin^2\frac{\theta_i}{2}\,\mathrm{d}\theta_i^2 + 4\sum_i \cos^2\frac{\theta_i}{2}\,\mathrm{d}\phi_i^2 - 4\left|\sum_i \cos^2\frac{\theta_i}{2}\,\mathrm{d}\phi_i\right|^2 \\
&\geq \sum_i \sin^2\frac{\theta_i}{2}\,\mathrm{d}\theta_i^2 \\
&= \sum_i \left(2\,\mathrm{d}\cos\frac{\theta_i}{2}\right)^2 \\
&= \sum_i \left(2\,\mathrm{d}\sqrt{P_i}\right)^2 .
\end{aligned}
\tag{2.30}
$$

This motivates us to define another metric for the manifold of probability distributions.

$$
\mathrm{d}s^2 = \sum_i \left(2\,\mathrm{d}\sqrt{P_i}\right)^2 = \sum_i \frac{\mathrm{d}P_i^2}{P_i}
\tag{2.31}
$$

The summary is below

$$
\mathrm{d}l^2 = \overbrace{\underbrace{\overbrace{\left(\begin{array}{c}\text{Distance from}\\ \text{Probability distribution}\end{array}\right)^2}^{\mathrm{d}s^2}}_{\propto \text{Classical Fisher information } F} + \left(\begin{array}{c}\text{Distance from}\\ \text{Relative phases}\end{array}\right)^2}^{\mathrm{d}S^2} + \overbrace{\left(\begin{array}{c}\text{Distance from}\\ \text{Global phase}\end{array}\right)^2}^{4\,\mathrm{d}\gamma^2} .
\tag{2.32}
$$

In order to relate the geometric distance with measurable quantities, we parameterize a trajectory in either space with α. The expressions are

$$
P_i = P_i(\alpha), \quad |\psi\rangle = |\psi_\alpha\rangle\,,
\tag{2.33}
$$

with the differentials

$$
\mathrm{d}P_i = \partial_\alpha P_i(\alpha)\,\mathrm{d}\alpha, \quad |\mathrm{d}\psi\rangle = |\partial_\alpha \psi_\alpha\rangle\,\mathrm{d}\alpha.
\tag{2.34}
$$

The rate of change $\mathrm{d}s/d\alpha$ and $\mathrm{d}S/d\alpha$ could be understood as the analogue of a velocity. The square of this velocity is defined as the classical Fisher information

$$
F_\alpha = \left(\frac{\mathrm{d}s}{\mathrm{d}\alpha}\right)^2 = \sum_i \frac{[\partial_\alpha P_i(\alpha)]^2}{P_i(\alpha)},
\tag{2.35}
$$

and quantum Fisher information [48–50]

$$\mathcal{F}_\alpha = \left(\frac{\mathrm{d}S}{\mathrm{d}\alpha}\right)^2 = \left(\frac{\mathrm{d}l}{\mathrm{d}\alpha}\right)^2 - 4\left(\frac{\mathrm{d}\gamma}{\mathrm{d}\alpha}\right)^2 = 4(\langle\partial_\alpha\psi_\alpha|\partial_\alpha\psi_\alpha\rangle - |\langle\psi_\alpha|\partial_\alpha\psi_\alpha\rangle|^2). \tag{2.36}$$

Eq. (2.32) implies $\mathrm{d}s^2 \leq \mathrm{d}S^2$, which results in

$$F_\alpha \leq \mathcal{F}_\alpha. \tag{2.37}$$

In the next section, we relate the left-hand side, the classical Fisher information, with the variance of an unbiased estimator by establishing the Cramér–Rao Bound.

2.7 Cramér–Rao Bound

We can reinterpret the classical Fisher information F_α as follows:

$$F_\alpha \;=\; \sum_i \frac{\left(\partial_\alpha P_i(\alpha)\right)^2}{P_i(\alpha)} \;=\; \sum_i P_i(\alpha)\left(\frac{\partial_\alpha P_i(\alpha)}{P_i(\alpha)}\right)^2 \;=\; \sum_i P_i(\alpha)\, V_i(\alpha)^2 \;=\; \mathrm{E}[V_i(\alpha)^2], \tag{2.38}$$

where $\mathrm{E}[\cdot]$ denotes an *expectation value*, and

$$V_i(\alpha) \;=\; \frac{\partial_\alpha P_i(\alpha)}{P_i(\alpha)} \tag{2.39}$$

is a statistical quantity called the *score*. The score has a zero mean:

$$\mathrm{E}[V_i(\alpha)] \;=\; \sum_i P_i(\alpha)\,\frac{\partial_\alpha P_i(\alpha)}{P_i(\alpha)} \;=\; \partial_\alpha \sum_i P_i(\alpha) \;=\; \partial_\alpha(1) \;=\; 0. \tag{2.40}$$

Hence, F_α is the variance of $V_i(\alpha)$:

$$F_\alpha = \mathrm{E}[V_i(\alpha)^2] - \mathrm{E}[V_i(\alpha)]^2 = \mathrm{var}[V_i(\alpha)]. \tag{2.41}$$

Next, consider an unbiased estimator $\hat{\alpha}$ of α:

$$\mathrm{E}[\hat{\alpha}] = \alpha. \tag{2.42}$$

We calculate the covariance between $V_i(\alpha)$ and $\hat{\alpha}$:

$$\begin{aligned}\operatorname{cov}[V_i(\alpha),\,\hat{\alpha}] &= \mathrm{E}[V_i(\alpha)\,\hat{\alpha}] \;-\; \mathrm{E}[V_i(\alpha)]\,\mathrm{E}[\hat{\alpha}] \\ &= \sum_i P_i(\alpha)\,\frac{\partial_\alpha P_i(\alpha)}{P_i(\alpha)}\,\hat{\alpha} \;=\; \partial_\alpha \sum_i P_i(\alpha)\,\hat{\alpha} \\ &= \partial_\alpha\,\mathrm{E}[\hat{\alpha}] \;=\; 1.\end{aligned} \tag{2.43}$$

Using the Cauchy–Schwarz inequality on $\operatorname{cov}[V,\hat{\alpha}]$:

$$1 \;=\; \left(\operatorname{cov}[V,\hat{\alpha}]\right)^2 \;\le\; \operatorname{var}[V]\,\operatorname{var}[\hat{\alpha}] \;=\; F_\alpha\,\operatorname{var}[\hat{\alpha}], \tag{2.44}$$

which implies

$$\operatorname{var}[\hat{\alpha}] \;\ge\; \frac{1}{F_\alpha}. \tag{2.45}$$

If the experiment is repeated N times, the bound generalizes to

$$\operatorname{var}[\hat{\alpha}] \;\ge\; \frac{1}{N F_\alpha}, \tag{2.46}$$

the standard Cramér–Rao inequality for an unbiased estimator over N samples.

Hence, these definitions and properties establish the key tools for analyzing the performance limits of a quantum sensor. In the next section, we will apply this framework to a single-qubit sensing protocol.

2.8 Generalized Uncertainty Principle

Following the velocity analogue, we could write down the analogue of a Schrödinger equation for a parameterized trajectory

$$\mathrm{i}\,|\partial_\alpha \psi_\alpha\rangle = \hat{h}\,|\psi_\alpha\rangle\,, \tag{2.47}$$

where the Hermitian operator $\hat{h}$ is the generator of the evolution operator

$$U_\alpha = \mathrm{e}^{-\mathrm{i}\,\hat{h}\alpha}. \tag{2.48}$$

We have

$$\left(\frac{\mathrm{d}l}{\mathrm{d}\alpha}\right)^2 = 4\left\langle \partial_\alpha \psi_\alpha | \partial_\alpha \psi_\alpha \right\rangle = 4\left\langle \psi_\alpha | \hat{h}^2 | \psi_\alpha \right\rangle = 4\left\langle \hat{h}^2 \right\rangle \tag{2.49}$$

and

$$\left(\frac{\mathrm{d}\gamma}{\mathrm{d}\alpha}\right)^2 = \left|\left\langle \psi_\alpha | \partial_\alpha \psi_\alpha \right\rangle\right|^2 = \left|\left\langle \psi_\alpha | \hat{h} | \psi_\alpha \right\rangle\right|^2 = \left\langle \hat{h} \right\rangle^2 \tag{2.50}$$

The quantum Fisher information is four times of the quantum mechanical variance of the operator

$$\mathcal{F}_\alpha = \left(\frac{\mathrm{d}l}{\mathrm{d}\alpha}\right)^2 - 4\left(\frac{\mathrm{d}l}{\mathrm{d}\gamma}\right)^2 = 4\left(\left\langle \hat{h}^2 \right\rangle - \left\langle \hat{h} \right\rangle^2\right) = 4\left(\Delta h\right)^2. \tag{2.51}$$

Combining this with the Cramér-Rao bound gives rise to the generalized uncertainty principle.

$$\Delta\alpha \Delta h \geq \frac{1}{2}, \tag{2.52}$$

where $\Delta\alpha = \sqrt{\operatorname{var}\hat{\alpha}}$ is the uncertainty of the estimator $\hat{\alpha}$, which originates from a *statistical* perspective. While Δh is calculated from the expectation value of an operator, which is of *quantum mechanical* nature. This expression brings together the *conjugate pair* consisting of seemingly different types of quantities in a unified, symmetric manner.

2.9 Single Qubit Sensor

We consider a general qubit state in the $\hat{\boldsymbol{x}}$-$\hat{\boldsymbol{z}}$-plane parameterized by angle λ,

$$\left|\psi_{\alpha=0}\right\rangle = \cos\frac{\lambda}{2}\left|0\right\rangle + \sin\frac{\lambda}{2}\left|1\right\rangle. \tag{2.53}$$

To simplify the problem, we choose the rotation axis also within the $\hat{\boldsymbol{x}}$-$\hat{\boldsymbol{z}}$-plane:

$$\hat{\boldsymbol{n}} = \sin\theta\,\hat{\boldsymbol{x}} + \cos\theta\,\hat{\boldsymbol{z}}. \tag{2.54}$$

The corresponding rotation operator is

$$U_\alpha = R_{\hat{\boldsymbol{n}}}(\alpha) = \begin{pmatrix} \cos\dfrac{\alpha}{2} - \mathrm{i}\,\sin\dfrac{\alpha}{2}\cos\theta & -\mathrm{i}\,\sin\dfrac{\alpha}{2}\sin\theta \\ -\mathrm{i}\,\sin\dfrac{\alpha}{2}\sin\theta & \cos\dfrac{\alpha}{2} + \mathrm{i}\,\sin\dfrac{\alpha}{2}\cos\theta \end{pmatrix}. \tag{2.55}$$

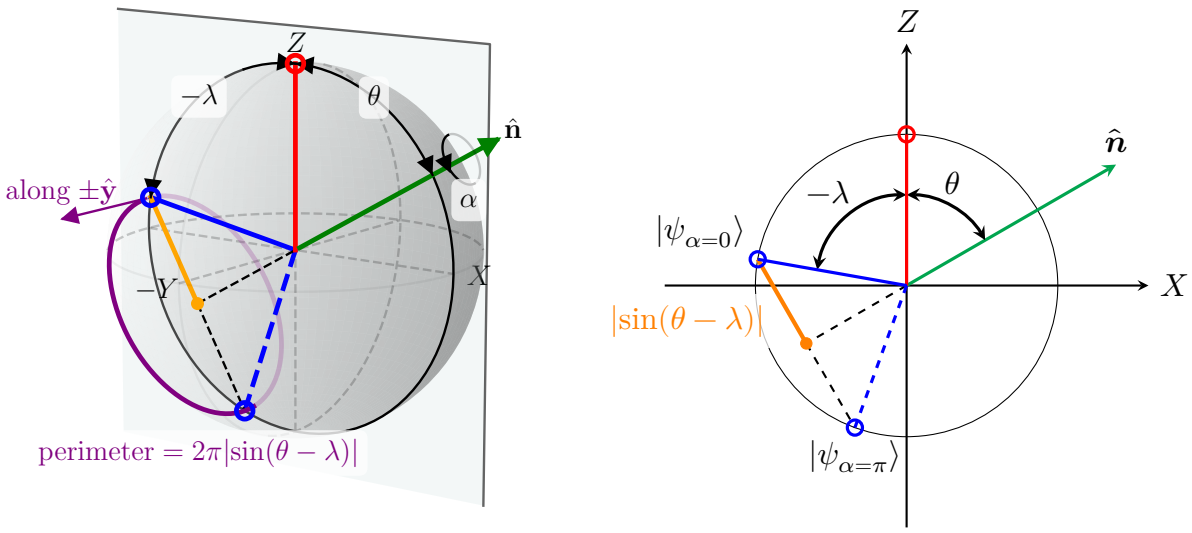

(a) (b)

Figure 2.13: **Single-qubit sensing protocol on the Bloch sphere.** (a) The blue and red solid lines represent the possible initial states. The green line represents the rotation axis $\hat{\boldsymbol{n}}$. The blue dashed line represents the qubit state after π-rotation. The purple circle represents the trajectory of the qubit state during the rotation. The perimeter of the circle is $2\pi|\sin(\theta-\lambda)|$. The purple arrow represents the vector tangent to the circle at the initial state. The tangent vector is always along the $\pm\hat{\boldsymbol{y}}$-axis. (b) The same geometry represented in the $\hat{\boldsymbol{x}}$-$\hat{\boldsymbol{z}}$-plane for clarity.

After the rotation

$$\begin{aligned}
|\psi_\alpha\rangle &= U_\alpha\,|\psi_{\alpha=0}\rangle \\
&= \left[\left(\cos\frac{\alpha}{2} - \mathrm{i}\,\sin\frac{\alpha}{2}\cos\theta\right)\cos\frac{\lambda}{2} - \mathrm{i}\,\sin\frac{\alpha}{2}\sin\theta\sin\frac{\lambda}{2}\right]|0\rangle \\
&\quad + \left[-\mathrm{i}\,\sin\frac{\alpha}{2}\sin\theta\cos\frac{\lambda}{2} + \left(\cos\frac{\alpha}{2} + \mathrm{i}\,\sin\frac{\alpha}{2}\cos\theta\right)\sin\frac{\lambda}{2}\right]|1\rangle \\
&= \left[\cos\frac{\alpha}{2}\cos\frac{\lambda}{2} - \mathrm{i}\,\sin\frac{\alpha}{2}\cos\left(\theta-\frac{\lambda}{2}\right)\right]|0\rangle \\
&\quad + \left[\cos\frac{\alpha}{2}\sin\frac{\lambda}{2} - \mathrm{i}\,\sin\frac{\alpha}{2}\sin\left(\theta-\frac{\lambda}{2}\right)\right]|1\rangle \\
&= \cos\frac{\alpha}{2}\,|\psi_{\alpha=0}\rangle + \sin\frac{\alpha}{2}\,|\psi_{\alpha=\pi}\rangle
\end{aligned} \tag{2.56}$$

where

$$|\psi_{\alpha=\pi}\rangle = -\mathrm{i}\left[\cos\left(\theta-\frac{\lambda}{2}\right)|0\rangle + \sin\left(\theta-\frac{\lambda}{2}\right)|1\rangle\right]. \tag{2.57}$$

The quantum and classical Fisher information are calculated in the following subsections.

2.9.1 Quantum Fisher Information

The quantum Fisher information can be calculated in multiple ways:

1. Evaluating Eq. (2.36) directly

We calculate the derivative

$$|\partial_\alpha \psi_\alpha\rangle = \frac{1}{2}\left(-\sin\frac{\alpha}{2}\,|\psi_{\alpha=0}\rangle + \cos\frac{\alpha}{2}\,|\psi_{\alpha=\pi}\rangle\right). \tag{2.58}$$

We first calculate the inner product

$$\langle\psi_{\alpha=0}|\psi_{\alpha=\pi}\rangle = -\,\mathrm{i}\,\cos(\theta-\lambda). \tag{2.59}$$

Next, we calculate

$$\left(\frac{\mathrm{d}l}{\mathrm{d}\alpha}\right)^2 = 4\,\langle\partial_\alpha\psi_\alpha|\partial_\alpha\psi_\alpha\rangle = 1, \tag{2.60}$$

and

$$\frac{\mathrm{d}\gamma}{\mathrm{d}\alpha} = \mathrm{i}\,\langle\psi_\alpha|\partial_\alpha\psi_\alpha\rangle = \frac{1}{2}\cos(\theta-\lambda). \tag{2.61}$$

The quantum fisher information is calculated

$$\mathcal{F}_\alpha = \left(\frac{\mathrm{d}l}{\mathrm{d}\alpha}\right)^2 - 4\left(\frac{\mathrm{d}\gamma}{\mathrm{d}\alpha}\right)^2 = \sin^2(\theta-\lambda). \tag{2.62}$$

2. Using the generalized uncertainty principle

Alternatively, one could use the generalized uncertainty principle with the generator

$$\hat{h} = \frac{1}{2}\boldsymbol{\sigma}\cdot\hat{\boldsymbol{n}} = \frac{1}{2}\left(\sin\theta\sigma_x + \cos\theta\sigma_z\right) \tag{2.63}$$

We calculate the expectation values with regard to the initial state $|\psi_{\alpha=0}\rangle$

$$\left\langle\hat{h}^2\right\rangle = \frac{1}{4}\,\langle I\rangle = \frac{1}{4}, \tag{2.64}$$

where I is the identity operator, and

$$\begin{aligned}\left\langle \hat{h} \right\rangle &= \frac{1}{2}\left(\sin\theta \left\langle \sigma_x \right\rangle + \cos\theta \left\langle \sigma_z \right\rangle\right) \\ &= \frac{1}{2}\left[2\sin\theta \sin\frac{\lambda}{2}\cos\frac{\lambda}{2} + \cos\theta\left(\cos^2\frac{\lambda}{2} - \sin^2\frac{\lambda}{2}\right)\right] \\ &= \frac{1}{2}\left(\sin\theta\sin\lambda + \cos\theta\cos\lambda\right) \\ &= \frac{1}{2}\cos(\theta-\lambda)\end{aligned} \tag{2.65}$$

We arrive at the same value

$$\mathcal{F}_{\alpha} = 4\left(\left\langle \hat{h}^2 \right\rangle - \left\langle \hat{h} \right\rangle^2\right) = \sin^2(\theta-\lambda) \tag{2.66}$$

3. Measuring the length of the trajectory geometrically

After every a 2π rotation $\Delta\alpha = 2\pi$, The perimeter of the circular trajectory is

$$\Delta S = 2\pi|\sin(\theta-\lambda)|, \tag{2.67}$$

Comparing these two lengths, we arrive at

$$\mathcal{F}_{\alpha} = \left(\frac{\Delta S}{\Delta\alpha}\right)^2 = \left(\frac{2\pi|\sin(\theta-\lambda)|}{2\pi}\right)^2 = \sin^2(\theta-\lambda). \tag{2.68}$$

The result shows that the quantum Fisher information is independent of the rotation angle α but is sensitive to the relative alignment between the rotation axis and the initial state. The maximum value $\mathcal{F}_{\alpha} = 1$ is only achieved when rotation axis and the initial state are perpendicular with each other on the Bloch sphere ($\theta - \lambda = \pm\pi/2$) [49, 51, 52]. However in the worst case where the initial state and the rotation axis are aligned or opposite ($\theta - \lambda = 0$ or π), the quantum Fisher information completely vanishes.

In order to experimentally obtain the quantum Fisher information, we need to perform measurement in a chosen basis. From the resulting probability distribution, we could extract the classical Fisher information.

2.9.2 Classical Fisher Information

From the Fig. (2.13a) we see the circular trajectory always starts with a tangent vector in parallel with $\hat{\boldsymbol{y}}$. This indicates the y-basis can be chosen as the measurement basis. We check it with the calculation. The Y eigenbasis is defined by

$$|y\pm\rangle = \frac{1}{\sqrt{2}}(|0\rangle \pm \mathrm{i}\,|1\rangle). \tag{2.69}$$

$$\begin{aligned} |\psi_\alpha\rangle &= U_\alpha\,|\psi_{\alpha=0}\rangle \\ &= \left[\cos\frac{\alpha}{2}\cos\frac{\lambda}{2} - \mathrm{i}\,\sin\frac{\alpha}{2}\cos\left(\theta-\frac{\lambda}{2}\right)\right]|0\rangle \\ &\quad + \left[\cos\frac{\alpha}{2}\sin\frac{\lambda}{2} - \mathrm{i}\,\sin\frac{\alpha}{2}\sin\left(\theta-\frac{\lambda}{2}\right)\right]|1\rangle\,. \end{aligned} \tag{2.70}$$

We calculate the probability of the measurement outcome

$$\begin{aligned} P_{y+}(\alpha) &= |\langle y+|\psi_\alpha\rangle|^2 \\ &= \frac{1}{2}\left|\cos\frac{\alpha}{2}\cos\frac{\lambda}{2} - \mathrm{i}\,\sin\frac{\alpha}{2}\cos\left(\theta-\frac{\lambda}{2}\right) - \mathrm{i}\,\cos\frac{\alpha}{2}\sin\frac{\lambda}{2} - \sin\frac{\alpha}{2}\sin\left(\theta-\frac{\lambda}{2}\right)\right|^2 \\ &= \frac{1}{2}\left\{1 - 2\sin\frac{\alpha}{2}\cos\frac{\alpha}{2}\left[\sin\left(\theta-\frac{\lambda}{2}\right)\cos\frac{\lambda}{2} - \cos\left(\theta-\frac{\lambda}{2}\right)\sin\frac{\lambda}{2}\right]\right\} \\ &= \frac{1}{2}\left[1 - \sin\alpha\sin(\theta-\lambda)\right] \end{aligned} \tag{2.71}$$

and

$$P_{y-}(\alpha) = 1 - P_{y+}(\alpha) = \frac{1}{2}\left[1 + \sin\alpha\sin(\theta-\lambda)\right] \tag{2.72}$$

The classical Fisher information

$$\begin{aligned} F_\alpha &= \frac{\left[\partial_\alpha P_{y+}(\alpha)\right]^2}{P_{y+}(\alpha)} + \frac{\left[\partial_\alpha P_{y-}(\alpha)\right]^2}{P_{y-}(\alpha)} \\ &= \frac{1}{2}\left[\frac{\cos^2\alpha\sin^2(\theta-\lambda)}{1-\sin\alpha\sin(\theta-\lambda)} + \frac{\cos^2\alpha\sin^2(\theta-\lambda)}{1+\sin\alpha\sin(\theta-\lambda)}\right] \\ &= \frac{\cos^2\alpha\sin^2(\theta-\lambda)}{1-\sin^2\alpha\sin^2(\theta-\lambda)} \end{aligned} \tag{2.73}$$

From the result, unlike the quantum Fisher information, the classical Fisher information is dependent on both α and $(\theta-\lambda)$. This is because the optimal measurement basis in dependent on

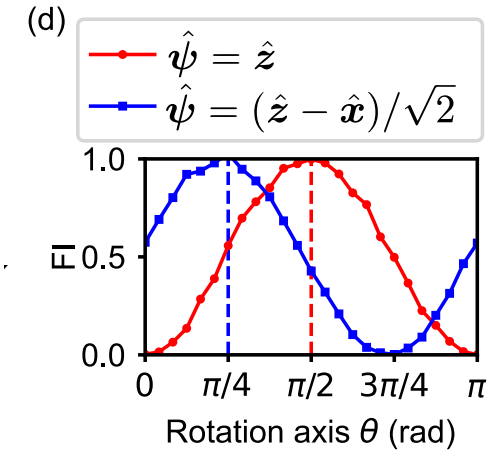

Figure 2.14: (2.8) Single qubit sensing. Blue curve shows when the initial state is along the $\hat{z}$-axis ($\lambda = 0$), and the Red curve shows when the initial state is along $(\hat{z} - \hat{x})/\sqrt{2}$-axis ($\lambda = -\pi/4$).

α. Fortunately, the maximum value is always achieved near $\alpha = 0$ or π, where the quantum fisher information is achieved.

2.9.3 Experimental Investigation for the Single Qubit Sensor

In order to experimentally test the ideas, we use superconducting transmon qubits.

We use curve fitting

$$P_{y-}(\alpha) = A + B\sin(\alpha + \delta). \tag{2.74}$$

with $P_{y+}(\alpha) = 1 - P_{y-}(\alpha)$. The experimentally measured Fisher information is

$$\begin{aligned} F_\alpha &= \frac{\left[\partial_\alpha P_{y+}(\alpha)\right]^2}{P_{y+}(\alpha)} + \frac{\left[\partial_\alpha P_{y-}(\alpha)\right]^2}{P_{y-}(\alpha)} \\ &= \frac{B^2\cos^2(\alpha+\delta)}{A + B\sin(\alpha+\delta)} + \frac{B^2\cos^2(\alpha+\delta)}{1 - A - B\sin(\alpha+\delta)} \end{aligned} \tag{2.75}$$

The point with the largest slope is $\alpha = -\delta$, from which we extract the Fisher information

$$F = F_{\alpha=-\delta} = \frac{B^2}{A} + \frac{B^2}{1-A} = \frac{B^2}{A(1-A)} \tag{2.76}$$

F is a function of θ because it is dependent on the rotation axis.

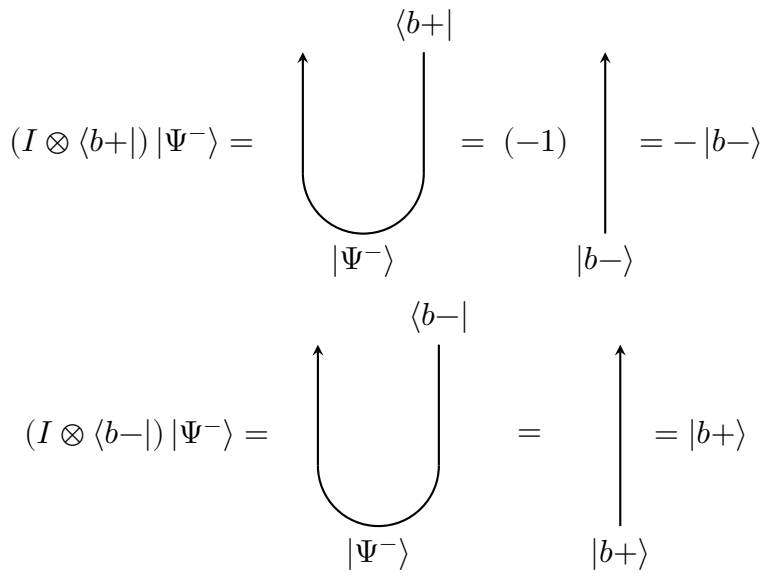

Figure 2.15: **Basis independence of the singlet state.** Projecting one of the qubits in a singlet state will always puts the other qubit in the orthogonal state (with a possible change in the global phase).

Even if the measurement basis is optimally chosen, the optimal initial state has to be dependent on the rotation axis. Without knowing the optimal initial state, one can learn about the rotation through quantum-process tomography [43, 53–56]. However, process tomography requires many applications of the rotation. Is there an approach to exploit the CTC to determine the optimal initial state after the rotation axis is revealed at a later time? In order to understand this, we first examine the rotational invariance of the singlet state.

2.10 Rotational Invariance of the Singlet State

The singlet state is defined as

$$|\Psi^-\rangle = \frac{1}{\sqrt{2}}\left(|0\rangle\,|1\rangle - |1\rangle\,|0\rangle\right). \tag{2.77}$$

Singlet state has the *basis independent* property. In order to see this, we define the unit vector

$$\hat{\boldsymbol{b}} = \sin\theta_b \cos\phi_b\,\hat{\boldsymbol{x}} + \sin\theta_b \sin\phi_b\,\hat{\boldsymbol{y}} + \cos\theta_b\,\hat{\boldsymbol{z}}. \tag{2.78}$$

The eigenstates of the Pauli operator $\boldsymbol{\sigma}\cdot\hat{\boldsymbol{b}}$ are

$$\begin{aligned}|b+\rangle &= \cos\frac{\theta_b}{2}\,|0\rangle + \mathrm{e}^{\,\mathrm{i}\,\phi_b}\sin\frac{\theta_b}{2}\,|1\rangle\,,\\ |b-\rangle &= -\mathrm{e}^{-\,\mathrm{i}\,\phi_b}\sin\frac{\theta_b}{2}\,|0\rangle + \cos\frac{\theta_b}{2}\,|1\rangle\,,\end{aligned} \tag{2.79}$$

which define a orthonormal basis. The singlet state in this $\{|b\pm\rangle\}$ basis is written as

$$\begin{aligned}|\Psi_b^-\rangle &= \frac{1}{\sqrt{2}}\left(|b+\rangle\,|b-\rangle - |b-\rangle\,|b+\rangle\right)\\ &= \frac{1}{\sqrt{2}}\Bigg[\left(\cos\frac{\theta_b}{2}\,|0\rangle + \mathrm{e}^{\,\mathrm{i}\,\phi_b}\sin\frac{\theta_b}{2}\,|1\rangle\right)\left(-\mathrm{e}^{-\,\mathrm{i}\,\phi_b}\sin\frac{\theta_b}{2}\,|0\rangle + \cos\frac{\theta_b}{2}\,|1\rangle\right)\\ &\qquad - \left(-\mathrm{e}^{-\,\mathrm{i}\,\phi_b}\sin\frac{\theta_b}{2}\,|0\rangle + \cos\frac{\theta_b}{2}\,|1\rangle\right)\left(\cos\frac{\theta_b}{2}\,|0\rangle + \mathrm{e}^{\,\mathrm{i}\,\phi_b}\sin\frac{\theta_b}{2}\,|1\rangle\right)\Bigg]\\ &= \frac{1}{\sqrt{2}}\Bigg[\Bigg(-\mathrm{e}^{-\,\mathrm{i}\,\phi_b}\sin\frac{\theta_b}{2}\cos\frac{\theta_b}{2}\,|0\rangle\,|0\rangle + \cos^2\frac{\theta_b}{2}\,|0\rangle\,|1\rangle\\ &\qquad\quad - \sin^2\frac{\theta_b}{2}\,|1\rangle\,|0\rangle + \mathrm{e}^{\,\mathrm{i}\,\phi_b}\sin\frac{\theta_b}{2}\cos\frac{\theta_b}{2}\,|1\rangle\,|1\rangle\Bigg)\\ &\qquad - \Bigg(-\mathrm{e}^{-\,\mathrm{i}\,\phi_b}\sin\frac{\theta_b}{2}\cos\frac{\theta_b}{2}\,|0\rangle\,|0\rangle - \sin^2\frac{\theta_b}{2}\,|0\rangle\,|1\rangle\\ &\qquad\quad + \cos^2\frac{\theta_b}{2}\,|1\rangle\,|0\rangle + \mathrm{e}^{\,\mathrm{i}\,\phi_b}\sin\frac{\theta_b}{2}\cos\frac{\theta_b}{2}\,|1\rangle\,|1\rangle\Bigg)\Bigg]\\ &= \frac{1}{\sqrt{2}}\left(|0\rangle\,|1\rangle - |1\rangle\,|0\rangle\right),\end{aligned} \tag{2.80}$$

which is the same as the singlet state defined in Eq. (2.84). This diagramatic representation is shown in Fig. (2.15).

The rotation operator along the $\hat{\boldsymbol{b}}$-axis is

$$\begin{aligned}R_{\hat{\boldsymbol{b}}}(\alpha) &= I\cos\frac{\alpha}{2} - \mathrm{i}\,\boldsymbol{\sigma}\cdot\hat{\boldsymbol{b}}\,\sin\frac{\alpha}{2}\\ &= \cos\frac{\alpha}{2}\left(|b+\rangle\langle b+| + |b-\rangle\langle b-|\right) - \mathrm{i}\,\sin\frac{\alpha}{2}\left(|b+\rangle\langle b+| - |b-\rangle\langle b-|\right)\\ &= \mathrm{e}^{-\,\mathrm{i}\,\alpha/2}\,|b+\rangle\langle b+| + \mathrm{e}^{\,\mathrm{i}\,\alpha/2}\,|b-\rangle\langle b-|\,.\end{aligned} \tag{2.81}$$

Applying simultaneus rotations on the two qubits

$$\begin{aligned}&\left[R_{\hat{\boldsymbol{b}}}(\alpha)\otimes R_{\hat{\boldsymbol{b}}}(\alpha)\right]\right]\,|\Psi^-\rangle\\ &= \frac{1}{\sqrt{2}}\left(\mathrm{e}^{-\,\mathrm{i}\,\alpha/2}\,|b+\rangle\,\mathrm{e}^{\,\mathrm{i}\,\alpha/2}\,|b-\rangle - \mathrm{e}^{\,\mathrm{i}\,\alpha/2}\,|b-\rangle\,\mathrm{e}^{-\,\mathrm{i}\,\alpha/2}\,|b+\rangle\right)\\ &= |\Psi^-\rangle\,,\end{aligned} \tag{2.82}$$

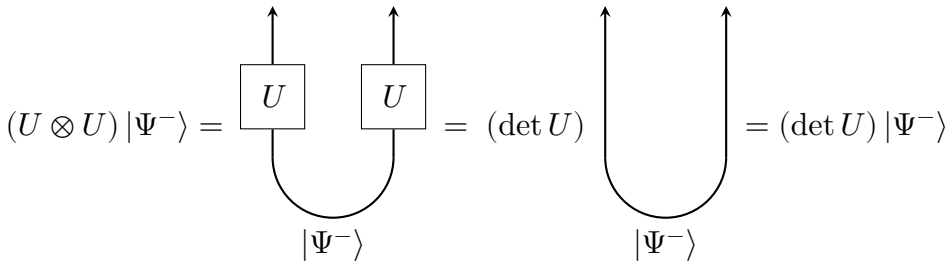

Figure 2.16: **Rotational invariance of the singlet state.** The singlet state is unchanged after simultaneously applying the same unitary operator on both of the qubits (up to a global phase).

where $\otimes$ represents the tensor product. For arbitrary unitary with an extra phase factor $U = e^{\mathrm{i}\,\xi} R_{\hat{\boldsymbol{b}}}$, Eq. (2.82) is correct upto a global phase

$$(U \otimes U)\,|\Psi^-\rangle = (\det U)\,|\Psi^-\rangle\,, \tag{2.83}$$

where $\det U = e^{2\,\mathrm{i}\,\xi}$ is the determinant of U.

2.11 Hindsight Sensing Protocol

We exploit the basis independence property of the singlet state to prepare the optimal initial state for the probe qubit.

The system consists of a *probe qubit* and an *ancilla qubit*. They are prepared in a singlet state

$$|\Psi^-\rangle = \frac{1}{\sqrt{2}}\left(|0\rangle_{\mathrm{P}}\,|1\rangle_{\mathrm{A}} - |1\rangle_{\mathrm{P}}\,|0\rangle_{\mathrm{A}}\right). \tag{2.84}$$

2.11.1 Protocol Outline

The *Hindsight Sensing* protocol proceeds as follows:

1. **Initial Entanglement**: Prepare two qubits (probe + ancilla) in the singlet state $|\Psi^-\rangle$.
2. **Unknown Rotation**: Apply the unknown unitary U_α to the *probe* qubit.
3. **Axis Revelation and Measurement**: Once $\hat{\boldsymbol{n}}$ is revealed at t_2, perform a projective measurement on the *ancilla* qubit in the basis aligned with $\hat{\boldsymbol{n}}$.

4. **Time Reversal Interpretation**: By the diagrammatic rules, this measurement outcome is fed back to the probe's initial state at t_0, effectively ensuring the probe was prepared in the optimal initial state for the now-known axis $\hat{\boldsymbol{n}}$.

2.11.2 Experimental Observations

In our transmon qubit device, we initialize the two qubits in the singlet state.

This means if we perform a projective measurement on the ancilla qubit in $\{|b\pm\rangle\}$, we have two equally possible outcomes. If the ancilla is measured to be $|b+\rangle$, the state of the probe is set to be $|b-\rangle$. And if the ancilla is measured to be $|b-\rangle$, the state of the probe is set to be $|b+\rangle$. In this way, we could use the ancilla qubit to effectively alter the state of the probe qubit, even after the rotation.

and implement the rotation $U(\alpha)$. We then measure various correlation observables.

A key experimental finding is that single-qubit expectation values of the probe remain essentially zero, indicating that all the relevant information about α is stored in the *two-qubit correlations*. Shown in Fig. (2.17b).

By choosing the ancilla measurement basis based on $\hat{\boldsymbol{n}}$, we detect a near-constant Fisher information over a wide range of $\hat{\boldsymbol{n}}$. The measured value ≈ 0.82 approaches the theoretical maximum 1 for a single qubit, outperforming the single-qubit protocol in which the axis is unknown at the outset.

What if the rotation axis is never known?

2.12 Agnostic Sensing Protocol

We first consider the case where no rotation is applied on the qubit. The system is prepared in the single state $|\Psi^-\rangle$, and projected back to $\langle\Psi^-|$. This could be understood as the analogue of a CTC. The probability will always be 1 (Fig. (2.18)).

Next, we consider adding a rotation. As is shown in Fig. (2.19a)

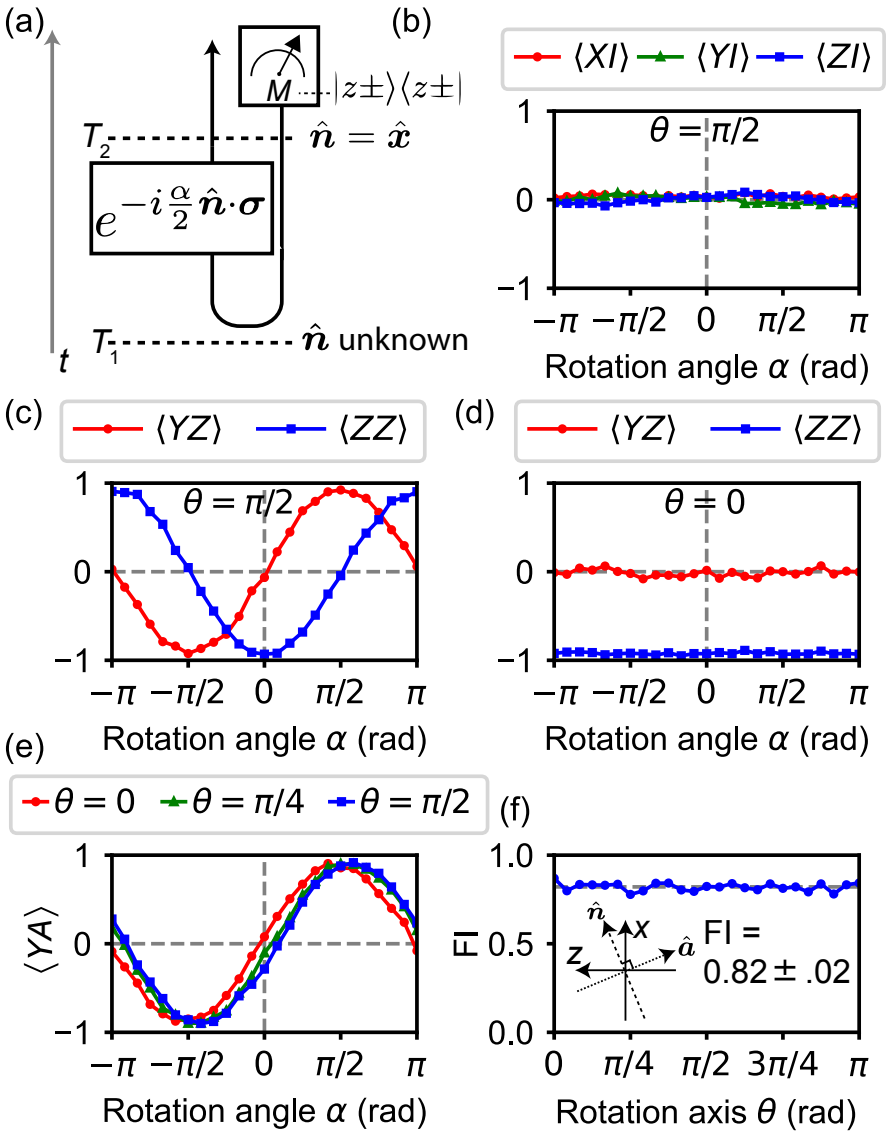

Figure 2.17: **Hindsight sensing.** (a) Schematic for the hindsight sensing protocol. (b) The expectation value of the single-body Pauli operators vanishes.

2.12.1 Concepts

The *Agnostic Sensing* protocol removes the requirement that $\mathbf{n}$ is revealed at any stage. Here:

1. Start in $|\Psi^-\rangle$.
2. Apply $U(\alpha)$ on the probe qubit.
3. Close the loop by projecting back into $|\Psi^-\rangle$ for both qubits, effectively forming a closed

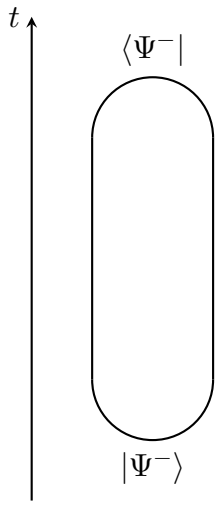

Figure 2.18: **Entanglement analogue of a CTC.** By connecting a cup with a cap, we prepare the system in an entangled state, let the two qubits wait for some time, and perform a projective measurement which collapse the quantum state into the same initial entangled state. Without additional interactions, the probability will be 1. Alternatively, this diagram can be interpreted as one qubit traveling forward and backward in time, following a closed time-like curve.

time-like curve without explicit knowledge of .

Because the qubits begin and end in the same entangled state, any change in the probability of returning to $|\Psi^-\rangle$ directly encodes α. This global effect is axis-independent.

2.12.2 Results and Performance

Experimentally, we measure the probability that the two-qubit system returns to $|\Psi^-\rangle$ after the unknown rotation $U(\alpha)$. Fitting this probability over varying α provides the Fisher information, which averages around 0.72. While slightly lower than the hindsight protocol, it still surpasses the best *classical ancilla* protocol bound of $\frac{2}{3}$. This shows a clear quantum advantage in the axis-agnostic scenario.

Figure 2.20 shows a simplified illustration of how the return probability changes with α. The experimental points (blue circles) closely match the theoretical model (red line), demonstrating consistent axis independence across multiple rotation directions.

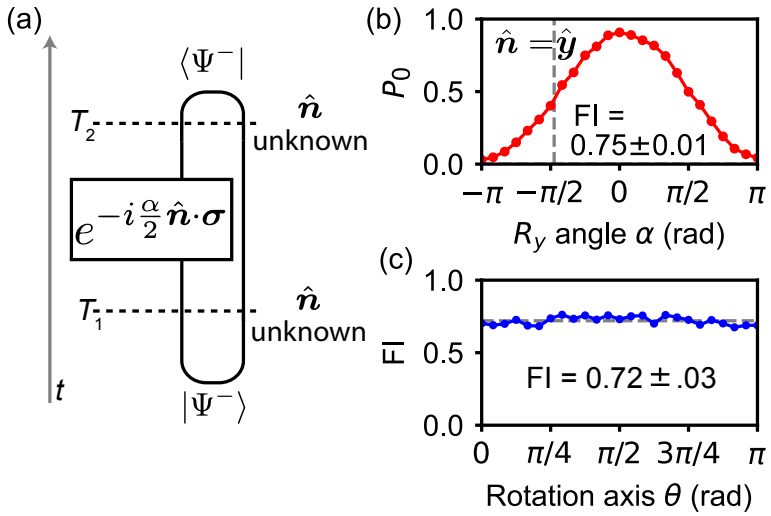

Figure 2.19: **Agnostic sensing protocol.** (a) Schematic of the agnostic sensing protocol.

2.12.3 Finite Fidelity

In the presence of finite state fidelity, the Fisher information degrades. We define the fidelity of quantum states ρ with respect to a target quantum state σ as

$$\mathfrak{F} = \left(\mathrm{tr}\sqrt{\rho\sqrt{\sigma}\rho}\right)^2 \tag{2.85}$$

In our case, the target state is the singlet state $\sigma = |\Psi^-\rangle\langle\Psi^-|$. We model the realistc quantum state to be an incoherent mixture of the singlet state and a maximally mixed state.

$$\rho = \mathfrak{F}\,|\Psi^-\rangle\langle\Psi^-| + \frac{1}{3}(1-\mathfrak{F})(\mathbb{1} - |\Psi^-\rangle\langle\Psi^-|) \tag{2.86}$$

The Fisher information is calculated as

$$F_\alpha = -\frac{(1-4\mathfrak{F})^2\sin^2\alpha}{[-5+2\mathfrak{F}+(-1+4\mathfrak{F})\cos\alpha]\,[1+2\mathfrak{F}+(-1+4\mathfrak{F})\cos\alpha]} \tag{2.87}$$

We find the Fisher information is highly sensitive to the infidelity of the input state. Especially, the Fisher information vanishes near $\alpha = 0$ or π for realistic entangled state with arbitrarily small infidelity. This motivates us to consider whether we could circumvent this drawback. We will come back to this problem in the next chapter.

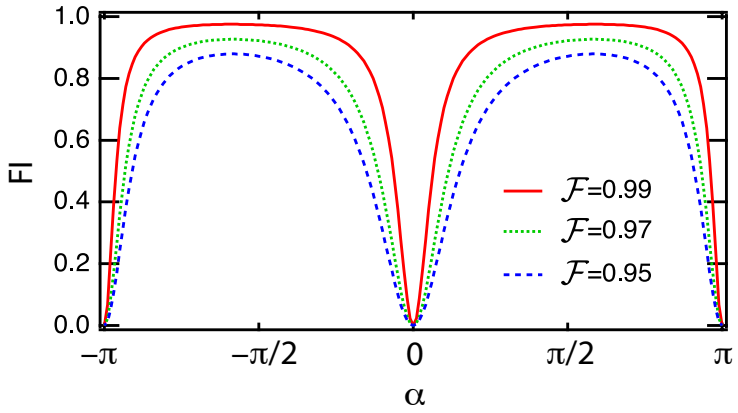

Figure 2.20: **Finite fidelity.** The curves show the dependence of Fisher information with respect to the fidelity of the singlet state. The different fidelity values of the singlet state are labeled by different colors and line styles.

2.13 Classical Ancilla

The optimal classical approach is given by a classical ancilla protocol. The density matrix has the general form of

$$\rho = \sum_j p_j \left|\psi_j\right\rangle\left\langle\psi_j\right| \otimes \left|j\right\rangle\left\langle j\right|, \tag{2.88}$$

where p_j satisfy

$$\sum_j p_j = 1. \tag{2.89}$$

For our case, the optimal classical ancilla state could be chosen as

$$\rho_0 = \frac{1}{3}(\left|x+\right\rangle\left\langle x+\right| \otimes \left|1\right\rangle\left\langle 1\right| + \left|y+\right\rangle\left\langle y+\right| \otimes \left|2\right\rangle\left\langle 2\right| + \left|z+\right\rangle\left\langle z+\right| \otimes \left|3\right\rangle\left\langle 3\right|) \tag{2.90}$$

The classical upper bound for the Fisher information is $2/3$, which could be intuitively understood (Fig. 5.11).

2.14 Summary

Our experimental data and theoretical analysis confirm the following:

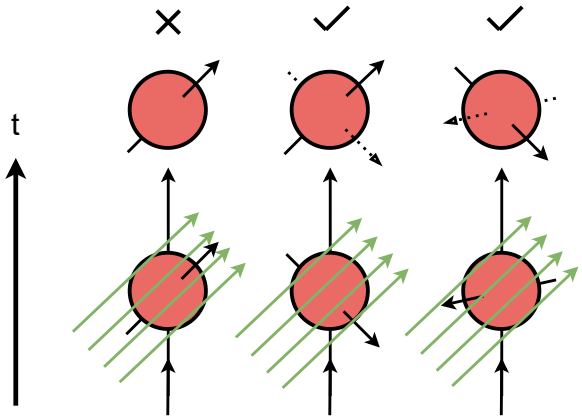

Figure 2.21: **classical ancilla.** Intuitively, only $2/3$ of the chance the initial state of the sensor is sensitive to an unknown rotation. The quantum Fisher information of a classical ancilla approach is $2/3$.

- **Single-Qubit Sensing** fails to maintain optimal sensitivity when the rotation axis is unknown.
- **Hindsight Sensing** allows near-maximal Fisher information (≈ 0.82) by postponing the choice of measurement basis until after the axis is revealed.
- **Agnostic Sensing** achieves axis independence *without* any knowledge of $\mathbf{n}$, exhibiting FI ≈ 0.72, above the classical ancilla limit of $\frac{2}{3}$.

These results underscore the power of quantum entanglement for metrology tasks where *no a priori* information about the parameter of interest is available.

2.15 Discussion

The last section is for a discussion of whether allowing quantum systems evolving backward in time is physical.

The time as we perceive always flows in one direction. One would wonder, how would evolution along a closed time-like curve possible? The seemingly contradiction comes the from the fact that we are working with a system dominated by quantum mechanical evolution of pure states. This assumption is both true for QED and the cQED when the environmental couplings are neglected during the timescale of interest. In order for irreversible effects to become manifest, we would need

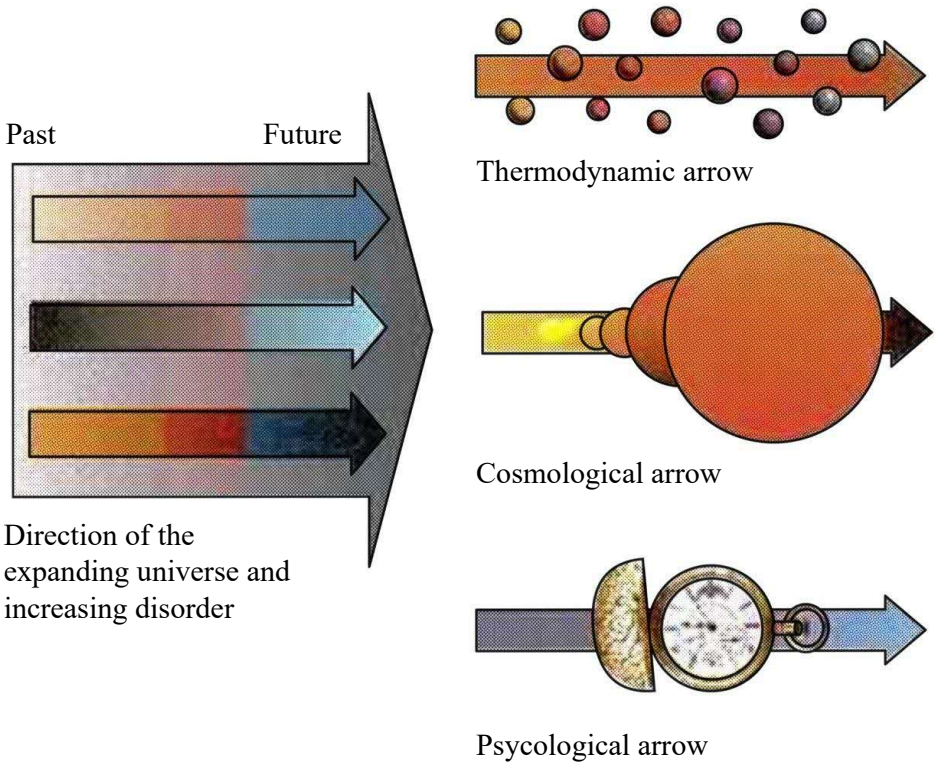

(a)

Figure 2.22: **Arrows of time.** There are at least three arrows of time: the direction in which disorder increases, the direction in which we perceive time passes, the direction in which the universe increases in size (Stephen Hawking) [57].

to consider a larger system, where the dynamics of open quantum systems and thermodynamical laws come to play. An large ensemble in the nature tend to behave in an irreversible fashion.

On the other hand, if we work with such a near-ideal quantum system, evolution backward in time should be considered as a type of *resource* that we could exploit. We have presented the idea of the metrological advantage achievable with closed time-like curves. More applications potentially exist.

In chapter one, we introduced the quantization of flux which could be considered as a closed time-like curve. We can make a comparison of them. The CTC we in counter in superconderctors is protected by the thermodynamics. Because it's energetically infavorable to break the order

parameter of the superconductor. However, here in this chapter, CTC is implemented with quantum gates and quantum measurements. The difference is, the latter one is not protect by thermodynamics. The condition of the system ends up in the singlet state is *probabilistic* rather than *deterministic*. In principle, it should be possible to engineer energetically favorable type of CTC for qubit case by engineering a corresponding order parameter. The existence of such type of CTC in a quantum system and potential applications remain to be explored.

Chapter 3: Tri-axis Sensor States

3.1 Introduction

We introduce the tri-axis sensor states in this chapter with three motivations: Though ideally, every maximally entangled two-qubit state, including the four Bell states, produces a similar metrological advantage predicted by quantum Fisher information, they become less sensitive approaching the probabilities $P = 0$ or $P = 1$. They are most sensitive at $P = 0.5$, where the rate of change is at the maximum. This motivates us to align this sensitive zone with small-angle rotations. In addition, the rotation measured by Bell states has sign ambiguity. The previous protocols does not resolve all

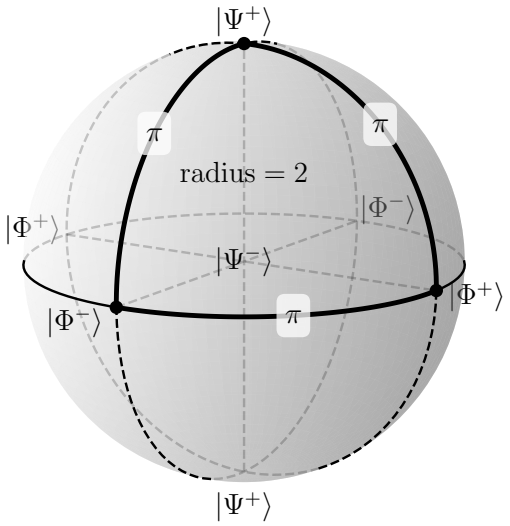

Figure 3.1: **Ball of two-qubit maximally entangled states.** Each point in a ball of radius 2 represents a two-qubit maximally entangled state. The surface of the ball is assigned to the triplet states. Specifically, the three pairs of antipodal points—corresponding to the directions $\pm\hat{\boldsymbol{x}}$, $\pm\hat{\boldsymbol{y}}$, and $\pm\hat{\boldsymbol{z}}$—are associated with the Bell states $|\Phi^-\rangle$, $|\Phi^+\rangle$, and $|\Psi^+\rangle$, respectively. These points are connected by circular arcs of length π on the surface, indicating the mutual orthogonality of the corresponding states. The singlet state $|\Psi^-\rangle$ is located at the center of the ball.

three components of the rotation, simultaneously. In order to circumvent these three drawbacks, in this chapter, we propose the *tri-axis sensor states*. In order to obtain an intuitive understanding of the states, we investigate the properties of the *two-qubit maximally entangled states*.

3.2 Two-qubit Maximally Entangled States

We parametrize the two-qubit maximally entangled states by (α, θ, ϕ). Applying rotation of α along the axis specified by the spherical coordinate θ and ϕ on the first qubit of the singlet state

$$\begin{aligned}
&|\Psi(\alpha,\theta,\phi)\rangle = [R(\alpha,\theta,\phi)\otimes I]\,|\Psi^-\rangle \\
&= \frac{1}{\sqrt{2}}\Big[\Big(\cos\frac{\alpha}{2} - \mathrm{i}\,\sin\frac{\alpha}{2}\cos\theta\Big)\,|01\rangle + \mathrm{i}\,\mathrm{e}^{-\mathrm{i}\,\phi}\sin\frac{\alpha}{2}\sin\theta\,|00\rangle \\
&\qquad\qquad - \mathrm{i}\,\mathrm{e}^{\mathrm{i}\,\phi}\sin\frac{\alpha}{2}\sin\theta\,|11\rangle - \Big(\cos\frac{\alpha}{2} + \mathrm{i}\,\sin\frac{\alpha}{2}\cos\theta\Big)\,|10\rangle\Big] \\
&= \cos\frac{\alpha}{2}\,|\Psi^-\rangle - \mathrm{i}\,\sin\frac{\alpha}{2}\cos\theta\,|\Psi^+\rangle + \mathrm{i}\,\sin\frac{\alpha}{2}\sin\theta\cos\phi\,|\Phi^-\rangle + \sin\frac{\alpha}{2}\sin\theta\sin\phi\,|\Phi^+\rangle
\end{aligned} \tag{3.1}$$

These states are *maximally entangled states* because any local unitary operation $[R(\alpha,\theta,\phi)\otimes I]$ is unable to disentangle the singlet state. We examine the above expression by calculating a few special cases. We start with the trivial case where $\alpha = 0$,

$$|\Psi(0,\theta,\phi)\rangle = |\Psi^-\rangle\,, \tag{3.2}$$

The qubits remain in the singlet state, as expected. Next, we consider the triplet states obtained by a π-rotation along an arbitrary axis defined by θ and ϕ

$$|\Psi(\pi,\theta,\phi)\rangle = -\,\mathrm{i}\,\cos\theta\,|\Psi^+\rangle + \mathrm{i}\,\sin\theta\cos\phi\,|\Phi^-\rangle + \sin\theta\sin\phi\,|\Phi^+\rangle\,. \tag{3.3}$$

The result is a 2-dimensional sphere spanned by the three Bell states $\{-\mathrm{i}\,|\Psi^+\rangle\,, \mathrm{i}\,|\Phi^-\rangle\,, |\Phi^+\rangle\}$. Moreover, the sphere is parameterized by the usual spherical coordinates (θ, ϕ) after the extra phase factors are omitted. This fact motivates us to visualize these three triplet states on a sphere. We align the triplet states with the $\{\hat{\boldsymbol{x}}, \hat{\boldsymbol{y}}, \hat{\boldsymbol{z}}\}$ unit vectors in a usual Cartesian coordinate system, respectively.

We define this sphere ($\alpha = \pi$) together with its interior ($0 \leq \alpha < \pi$) the *ball of two-qubit maximally entangled states*, or simply the *2QMES ball*.

Unlike the Bloch sphere, the 2QMES ball has peculiar properties that we will discuss. We first calculate the radius of the ball. Recall from the Bloch sphere, orthogonal quantum states are separated by π distance measured from the length of the geodesic. The triplet states are orthogonal with each other, connected by quarter circles (of $\pi/2$ radian) on the surface. By assuming the quarter circles are the geodesics, we conclude that the radius of the ball is $\pi/(\pi/2) = 2$.

The center of the ball is the singlet state, which should be orthogonal with all the triplet states. However, the Euclidean distance between the center and the surface of the ball is 2 which is less than π.

The second peculiarity appears when we consider the pair of *antipodal points* on the ball. We calculate

$$|\Psi(\pi, \pi-\theta, \phi+\pi)\rangle = \mathrm{i}\cos\theta\,|\Psi^+\rangle - \mathrm{i}\sin\theta\cos\phi\,|\Phi^-\rangle - \sin\theta\sin\phi\,|\Phi^+\rangle = -|\Psi(\pi,\theta,\phi)\rangle\,. \tag{3.4}$$

The antipodal points represents physically identical states except for an extra global π phase difference. Intuitively, this is because single-qubit π rotations along axes $\hat{\boldsymbol{n}}$ and $-\hat{\boldsymbol{n}}$ are equivalent up to a minus sign. and In the next subsection, we explore the peculiarities of the 2QMES ball with detailed calculations.

3.2.1 Measuring Distance in the 2QMES Ball

Following the same idea for the Bloch sphere

$$\begin{aligned}
&|\mathrm{d}\Psi\rangle \\
&= \frac{1}{2}\left[-\sin\frac{\alpha}{2}\,|\Psi^-\rangle + \cos\frac{\alpha}{2}\left(-\mathrm{i}\cos\theta\,|\Psi^+\rangle + \mathrm{i}\sin\theta\cos\phi\,|\Phi^-\rangle + \sin\theta\sin\phi\,|\Phi^+\rangle\right)\right]\mathrm{d}\alpha \\
&\quad + \sin\frac{\alpha}{2}\left(\mathrm{i}\sin\theta\,|\Psi^+\rangle + \mathrm{i}\cos\theta\cos\phi\,|\Phi^-\rangle + \cos\theta\sin\phi\,|\Phi^+\rangle\right)\mathrm{d}\theta \\
&\quad + \sin\frac{\alpha}{2}\sin\theta\left(-\mathrm{i}\sin\phi\,|\Phi^-\rangle + \cos\phi\,|\Phi^+\rangle\right)\mathrm{d}\phi
\end{aligned} \tag{3.5}$$

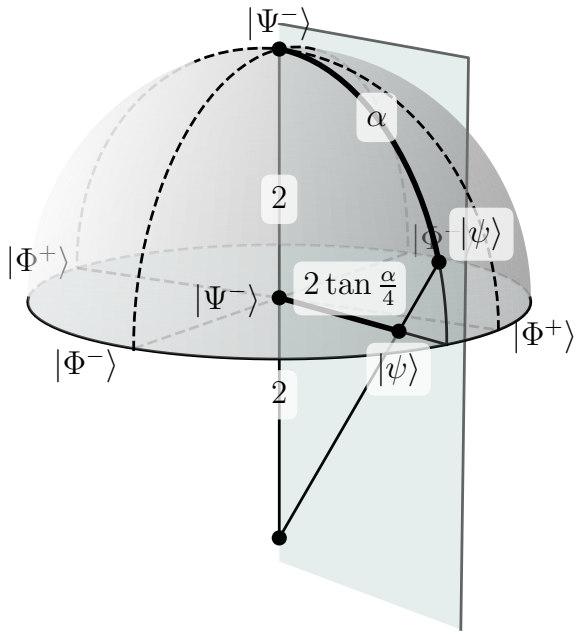

Figure 3.2: **Stereographic projection of the equatorial plane of the 2QMES ball.** The distances labeled here are measured in the usual Euclidean metric of the Cartesian coordinates. The arc in the upper hemisphere with length α is projected to the equatorial plane as a line segment of $2\tan(\alpha/4)$. Particularly, when $\alpha = \pi$, the length of the projection is 2, which is equal to the radius of the 2QMES ball. The stereographic projection explains why the singlet state appears closer to the triplet states in the 2QMES ball, though they are separated by geodesic distance of π. Note that the antipodal points in the equatorial plane represents the same state. By identifying the pair of antipodal points here, we conclude that the equatorial plane has the topology of a two-dimensional real projective plane $\mathbb{RP}^2$.

We calculate

$$\mathrm{d}l^2 = 4||\mathrm{d}\Psi\rangle|^2 = \mathrm{d}\alpha^2 + 4\sin^2\frac{\alpha}{2}\,\mathrm{d}\theta^2 + 4\sin^2\frac{\alpha}{2}\sin^2\theta\,\mathrm{d}\phi^2 \tag{3.6}$$

The geometric phase seemingly vanishes

$$\mathrm{d}\gamma = \mathrm{i}\,\langle\Psi|\mathrm{d}\Psi\rangle = 0. \tag{3.7}$$

However, this does not imply the space is flat. We will discuss the geometric phase later. Combining

Figure 3.3: **Northern hemisphere map.** A similar stereographic projection technique is employed to create maps of the Earth. In this projection, the north pole is placed at the center while the equator forms the outer boundary. Due to inherent map distortions, the circles of latitude (represented by circular dotted lines) are not evenly spaced. On the map, geodesics appear as circular arcs (shown as solid black lines) connecting pairs of antipodal points (marked by black dots) on the equator. Although these geodesics share the same length on the sphere, they appear with varying lengths in the projection.

the above derivation, we obtain

$$\begin{aligned} \mathrm{d}S^2 &= \mathrm{d}l^2 - 4\,\mathrm{d}\gamma^2 \\ &= \mathrm{d}\alpha^2 + 4\sin^2\frac{\alpha}{2}\,\mathrm{d}\theta^2 + 4\sin^2\frac{\alpha}{2}\sin^2\theta\,\mathrm{d}\phi^2 \\ &= \mathrm{d}\alpha^2 + 4\sin^2\frac{\alpha}{2}\left(\mathrm{d}\theta^2 + \sin^2\theta\,\mathrm{d}\phi^2\right). \end{aligned} \tag{3.8}$$

Although the (θ, ϕ) part displays spherical symmetry, this metric tells us the space is curved because it differs from the metric of usual spherical coordinates.

$$\mathrm{d}S^2_{\mathrm{sphere}} = \mathrm{d}r^2 + r^2\left(\mathrm{d}\theta^2 + \sin^2\theta\,\mathrm{d}\phi^2\right). \tag{3.9}$$

In order to analyze this, it is sufficient to inspect one cross section, due to the spherical symmetry. We choose the equatorial plane $\theta = \pi/2$, where

$$\mathrm{d}S^2 = \mathrm{d}\alpha^2 + 4\sin^2\frac{\alpha}{2}\,\mathrm{d}\phi^2. \tag{3.10}$$

Based on our previous analysis Fig. (2.9), this is the metric of the hemisphere of radius 2. This motivates us to use the stereographic projection to flatten this cross section.

$$r = 2\tan\frac{\alpha}{4} \tag{3.11}$$

Another important feature of the 2QMES ball is the states does not include relative phase, which implies

$$\mathrm{d}s^2 = \mathrm{d}S^2, \tag{3.12}$$

Measuring from the Bell basis, the classical Fisher information is always equal to the quantum Fisher information.

3.2.2 Geodesics in the 2QMES Ball

Geodesics in the 2QMES ball are circular arcs connecting a pair of antipodal points. The special case is the geodesics pass through the center of the ball, namely the singlet state $|\Psi\rangle^-$. In this case the arc becomes a straight line as the radius of the arc becomes infinite. The length of a geodesic is always 2π.

The 2QMES ball is topologically a three-dimensional *real projective plane* $\mathbb{RP}^3$.

3.3 Tri-axis Sensor States

3.3.1 Definition

The tri-axis sensor states are obtained by $2\pi/3$ rotations along certain axes

$$\alpha_S = \frac{2\pi}{3}, \quad \cos\frac{\alpha_S}{2} = \frac{1}{2}, \quad \sin\frac{\alpha_S}{2} = \frac{\sqrt{3}}{2}. \tag{3.13}$$

For example, the $|S^{+++}\rangle$ state, the axes are specified by θ_S, with

$$\cos\theta_S = \frac{1}{\sqrt{3}}, \quad \sin\theta_S = \sqrt{\frac{2}{3}}, \quad \tan\theta_S = \sqrt{2}, \tag{3.14}$$

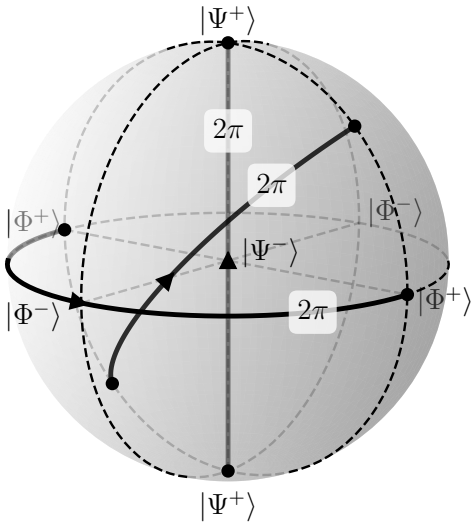

Figure 3.4: **Geodesics in the 2QMES ball.** The three solid lines in the graph are examples of geodesics. Each connects a pair of antipodal points on the sphere, which represent the same quantum state. Depending on its path, a geodesic appears either as a circular arc or as a straight line when it passes through the origin (which represents the singlet state $|\Psi^-\rangle$). Notably, the three geodesics chosen for this graph exhibit the same shapes as the three solid lines in Fig. (3.3). Regardless of their appearance, every geodesic in the 2QMES ball has a length of 2π. Specifically, the geodesics shown in the graph correspond to the trajectories of quantum states undergoing rotation about the $\hat{z}$-axis, with the direction of rotation indicated by the arrow at the midpoint of each trajectory.

and the value for ϕ

$$\phi_S = \frac{\pi}{4}, \quad \cos\phi_S = \sin\phi_S = \frac{1}{\sqrt{2}}. \tag{3.15}$$

The other tri-axis sensor states can be obtained with 8 combinations of

$$|S\rangle = \left|\Psi\left(\frac{2\pi}{3}, \theta_S \text{ or } (\pi - \theta_S), \pm\frac{\pi}{4} \text{ or } \pm\frac{3\pi}{4}\right)\right\rangle. \tag{3.16}$$

We represent these states in qubit and Bell basis as

$$\begin{aligned} |S^{m_x m_y m_z}\rangle &= \frac{1}{2\sqrt{2}}\left[(1 - \mathrm{i}\, m_z)\,|01\rangle + (\mathrm{i}\, m_x + m_y)\,|00\rangle - (\mathrm{i}\, m_x - m_y)\,|11\rangle - (1 + \mathrm{i}\, m_z)\,|10\rangle\right] \\ &= \frac{1}{2}\left(|\Psi^-\rangle - \mathrm{i}\, m_z\,|\Psi^+\rangle + \mathrm{i}\, m_x\,|\Phi^-\rangle + m_y\,|\Phi^+\rangle\right), \end{aligned} \tag{3.17}$$

where m_x, m_y, m_z are indices taking values from ± 1. Geometrically, the indices label the *octant* the state is located. For example, the $m_x = +1,\ m_y = -1,\ m_z = +1$ tri-axis sensor state is

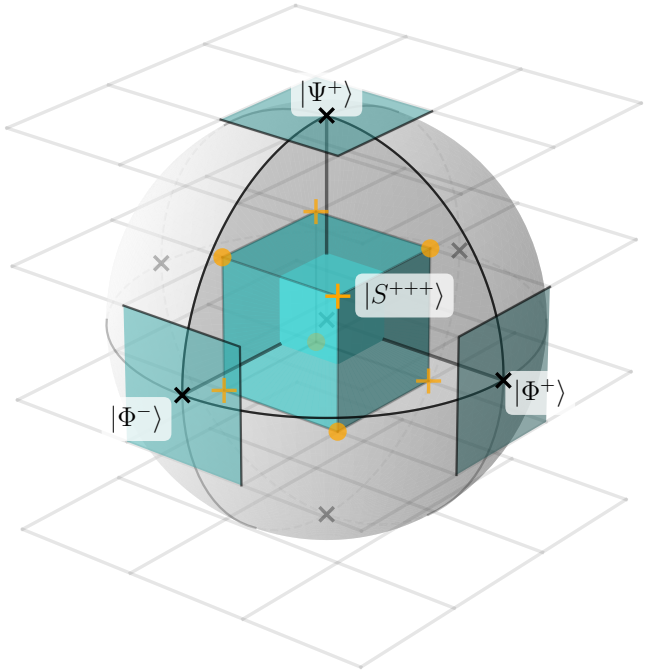

Figure 3.5: **Tri-axis sensor states.** The Bell states are labeled with black $\times$. The even (odd) tri-axis sensor states are labeled with orange $+$ (circles). The total eight tri-axis sensor states form a cube inside of the 2QMES ball. In the stereographic projection, the edge size of the cube is exactly $1/3$ of the diameter of the 2QMES ball. The two groups of tri-axis sensor states form two sets of orthogonal bases, respectively. In other words, the geodesic distance between two tri-axis sensor states with the same parity is π. The geodesic distance between an even and an odd tri-axis sensor state is $2\pi/3$. The geodesic distance between a tri-axis sensor state and a Bell state is also $2\pi/3$.

denoted as $|S^{+-+}\rangle$, in the $x > 0, y < 0, z > 0$ octant.

m_x, m_y, m_z transforms when applied these of the three *mirror reflection operators* along each axis in the 2QMES ball. For example

$$M_x |S^{+-+}\rangle = |S^{---+}\rangle \tag{3.18}$$

$$\begin{aligned} M_x &= |01\rangle\langle 01| + |10\rangle\langle 10| + |11\rangle\langle 00| + |00\rangle\langle 11| \\ M_y &= |01\rangle\langle 01| + |10\rangle\langle 10| - |11\rangle\langle 00| - |00\rangle\langle 11| \\ M_z &= -|10\rangle\langle 01| - |01\rangle\langle 10| + |00\rangle\langle 00| + |11\rangle\langle 11| \end{aligned} \tag{3.19}$$

They could be alternatively represented in the Bell basis

$$\begin{aligned} M_x &= |\Psi^-\rangle\langle\Psi^-| + |\Psi^+\rangle\langle\Psi^+| - |\Phi^-\rangle\langle\Phi^-| + |\Phi^+\rangle\langle\Phi^+| \\ M_y &= |\Psi^-\rangle\langle\Psi^-| + |\Psi^+\rangle\langle\Psi^+| + |\Phi^-\rangle\langle\Phi^-| - |\Phi^+\rangle\langle\Phi^+| \\ M_z &= |\Psi^-\rangle\langle\Psi^-| - |\Psi^+\rangle\langle\Psi^+| + |\Phi^-\rangle\langle\Phi^-| + |\Phi^+\rangle\langle\Phi^+| \end{aligned} \tag{3.20}$$

We also introduce the product of the three indices

$$m = m_x m_y m_z, \tag{3.21}$$

which also takes value from ± 1. Even number of mirror reflections keep m unchanged, while odd number of mirror reflections flip the sign of m. In this sense, we also call m the parity of the tri-axis sensor state. The tri-axis sensor states with the same parity form an orthonormal basis for the two-qubit states.

3.3.2 State Preparation

There is likely a family of them. For example, this one is constructed by applying a -120 degree rotation along the diagonal $\frac{1}{\sqrt{3}}(\hat{x}+\hat{y}+\hat{z})$ axis after preparing $|\Phi^+\rangle$

$$\begin{aligned} |S'\rangle &= \frac{1}{2}\left(|\Phi^+\rangle + \mathrm{i}\,|\Phi^-\rangle + \mathrm{i}\,|\Psi^+\rangle + |\Psi^-\rangle\right) \\ &= \frac{1}{2\sqrt{2}}\left[(1+\mathrm{i})\,|00\rangle + (1+\mathrm{i})\,|01\rangle + (\mathrm{i}-1)\,|10\rangle + (1-\mathrm{i})\,|11\rangle\right] \end{aligned} \tag{3.22}$$

Since the entangled state prepared by our parametric drive is naturally closest to $|\Psi^+\rangle$, we can use this one

$$\begin{aligned} |S\rangle &= \frac{1}{2}\left[\mathrm{i}\,|\Phi^+\rangle + |\Phi^-\rangle - |\Psi^+\rangle + \mathrm{i}\,|\Psi^-\rangle\right] \\ &= \frac{1}{2\sqrt{2}}\left[(1+\mathrm{i})\,|00\rangle + (\mathrm{i}-1)\,|01\rangle - (\mathrm{i}+1)\,|10\rangle + (\mathrm{i}-1)\,|11\rangle\right], \end{aligned} \tag{3.23}$$

which is constructed by applying a 120-degree rotation along the diagonal $\frac{1}{\sqrt{3}}(\hat{x}+\hat{y}+\hat{z})$ axis

Along an arbitrary axis, the quantum Fisher information is 1 due to symmetry.

3.3.3 Classical Fisher Information

For x-rotations

$$U(\theta_x, 0, 0) = \begin{pmatrix} \cos\alpha_x/2 & -\mathrm{i}\,\sin\alpha_x/2 \\ -\mathrm{i}\,\sin\alpha_x/2 & \cos\alpha_x/2 \end{pmatrix}. \tag{3.24}$$

The probabilities for the Bell basis measurements

$$P(\theta_x, \Phi^+) = \frac{1}{4}(1 + \sin\theta_x), \tag{3.25}$$

$$P(\theta_x, \Phi^-) = \frac{1}{4}(1 - \sin\theta_x), \tag{3.26}$$

$$P(\theta_x, \Psi^+) = \frac{1}{4}(1 - \sin\theta_x), \tag{3.27}$$

$$P(\theta_x, \Psi^-) = \frac{1}{4}(1 + \sin\theta_x). \tag{3.28}$$

Although, for each of the single outcomes, the modulation of the probability is only half of the amplitude compared with the single-qubit case. But considering the contributions from all of them, the total classical fisher information

$$\begin{aligned} F = & \frac{[\partial_{\theta_x} P(\theta_x, \Phi^+)]^2}{P(\theta_x, \Phi^+)} + \frac{[\partial_{\theta_x} P(\theta_x, \Phi^-)]^2}{P(\theta_x, \Phi^-)} + \frac{[\partial_{\theta_x} P(\theta_x, \Psi^+)]^2}{P(\theta_x, \Psi^+)} + \frac{[\partial_{\theta_x} P(\theta_x, \Psi^-)]^2}{P(\theta_x, \Psi^-)} \\ & = 1, \end{aligned} \tag{3.29}$$

Similarly, for y-rotations

$$U(0, \theta_y, 0) = \begin{pmatrix} \cos\theta_y/2 & -\sin\theta_y/2 \\ \sin\theta_y/2 & \cos\theta_y/2 \end{pmatrix}. \tag{3.30}$$

The probabilities for the Bell basis measurements

$$P(\theta_y, \Phi^+) = \frac{1}{4}(1 + \sin\theta_y), \tag{3.31}$$

$$P(\theta_y, \Phi^-) = \frac{1}{4}(1 + \sin\theta_y), \tag{3.32}$$

$$P(\theta_y, \Psi^+) = \frac{1}{4}(1 - \sin\theta_y), \tag{3.33}$$

$$P(\theta_y, \Psi^-) = \frac{1}{4}(1 - \sin\theta_y). \tag{3.34}$$

Easy to check

$$F = 1. \tag{3.35}$$

for z-rotations

$$U(0, 0, \theta_z) = \begin{pmatrix} e^{-\mathrm{i}\,\theta_z/2} & 0 \\ 0 & e^{\mathrm{i}\,\theta_z/2} \end{pmatrix}. \tag{3.36}$$

The probabilities for the Bell basis measurements

$$P(\theta_z, \Phi^+) = \frac{1}{4}(1 - \sin\theta_z), \tag{3.37}$$

$$P(\theta_z, \Phi^-) = \frac{1}{4}(1 + \sin\theta_z), \tag{3.38}$$

$$P(\theta_z, \Psi^+) = \frac{1}{4}(1 - \sin\theta_z), \tag{3.39}$$

$$P(\theta_z, \Psi^-) = \frac{1}{4}(1 + \sin\theta_z). \tag{3.40}$$

Easy to check

$$F = 1. \tag{3.41}$$

3.3.4 Quantum Fisher Information Matrix

We consider measuring the three components of a rotation simultaneously. We use slightly different parameterizations for convenience.

$$U(\alpha_x, \alpha_y, \alpha_z) = e^{-\mathrm{i}\,\boldsymbol{\sigma}\cdot\boldsymbol{\alpha}/2} = I\cos\frac{\alpha}{2} - \frac{\mathrm{i}\,\boldsymbol{\sigma}\cdot\boldsymbol{\alpha}}{2}\sin\frac{\alpha}{2}, \tag{3.42}$$

where the rotation angle is a vector

$$\boldsymbol{\alpha} = (\alpha_x, \alpha_y, \alpha_z). \tag{3.43}$$

The magnitude of $\boldsymbol{\alpha}$ is the rotation angle

$$\alpha = |\boldsymbol{\alpha}| = \sqrt{\alpha_x^2 + \alpha_y^2 + \alpha_z^2}. \tag{3.44}$$

The coordinate transformation

$$\begin{aligned}\alpha_x &= \alpha \sin\theta \cos\phi,\\ \alpha_y &= \alpha \sin\theta \sin\phi,\\ \alpha_z &= \alpha \cos\theta.\end{aligned} \tag{3.45}$$

The differentials

$$\begin{pmatrix} \mathrm{d}\alpha_x \\ \mathrm{d}\alpha_y \\ \mathrm{d}\alpha_z \end{pmatrix} = \begin{pmatrix} \sin\theta\cos\phi & \alpha\cos\theta\cos\phi & -\alpha\sin\theta\sin\phi \\ \sin\theta\sin\phi & \alpha\cos\theta\sin\phi & \alpha\sin\theta\cos\phi \\ \cos\theta & -\alpha\sin\theta & 0 \end{pmatrix} \begin{pmatrix} \mathrm{d}\alpha \\ \mathrm{d}\theta \\ \mathrm{d}\phi \end{pmatrix}. \tag{3.46}$$

The inverse relations

$$\begin{pmatrix} \mathrm{d}\alpha \\ \mathrm{d}\theta \\ \mathrm{d}\phi \end{pmatrix} = \begin{pmatrix} \sin\theta\cos\phi & \sin\theta\sin\phi & \cos\theta \\ \frac{1}{\alpha}\cos\theta\cos\phi & \frac{1}{\alpha}\cos\theta\cos\phi & -\frac{1}{\alpha}\sin\theta\cos\phi \\ -\frac{\sin\phi}{\alpha\sin\theta} & \frac{\cos\phi}{\alpha\sin\theta} & 0 \end{pmatrix} \begin{pmatrix} \mathrm{d}\alpha_x \\ \mathrm{d}\alpha_y \\ \mathrm{d}\alpha_z \end{pmatrix}. \tag{3.47}$$

Due to spherical symmetry, we could choose an arbitrary direction. We choose a point along the $\hat{\boldsymbol{x}}$-axis $\theta = \pi/2,\ \phi = 0$, which generates

$$\begin{pmatrix} \mathrm{d}\alpha \\ \mathrm{d}\theta \\ \mathrm{d}\phi \end{pmatrix} = \begin{pmatrix} 1 & 0 & 0 \\ 0 & 0 & -\frac{1}{\alpha} \\ 0 & \frac{1}{\alpha} & 0 \end{pmatrix} \begin{pmatrix} \mathrm{d}\alpha_x \\ \mathrm{d}\alpha_y \\ \mathrm{d}\alpha_z \end{pmatrix}. \tag{3.48}$$

The metric is

$$\begin{aligned} dS^2 &= \mathrm{d}\alpha^2 + 4\sin^2\frac{\alpha}{2}\left(\mathrm{d}\theta^2 + \sin^2\theta\,\mathrm{d}\phi^2\right)\\ &= \mathcal{F}_{xx}\mathrm{d}\alpha_x^2 + \mathcal{F}_{yy}\mathrm{d}\alpha_y^2 + \mathcal{F}_{zz}\mathrm{d}\alpha_z^2, \end{aligned} \tag{3.49}$$

with the coefficients are the entries of the *quantum Fisher information matrix* [58, 59]

$$\begin{aligned}\mathcal{F}_{xx} &= 1\\ \mathcal{F}_{yy} &= \mathcal{F}_{zz} = \mathrm{sinc}^2\frac{\alpha}{2}\end{aligned} \tag{3.50}$$

where

$$\mathrm{sinc}\,x = \frac{\sin x}{x}. \tag{3.51}$$

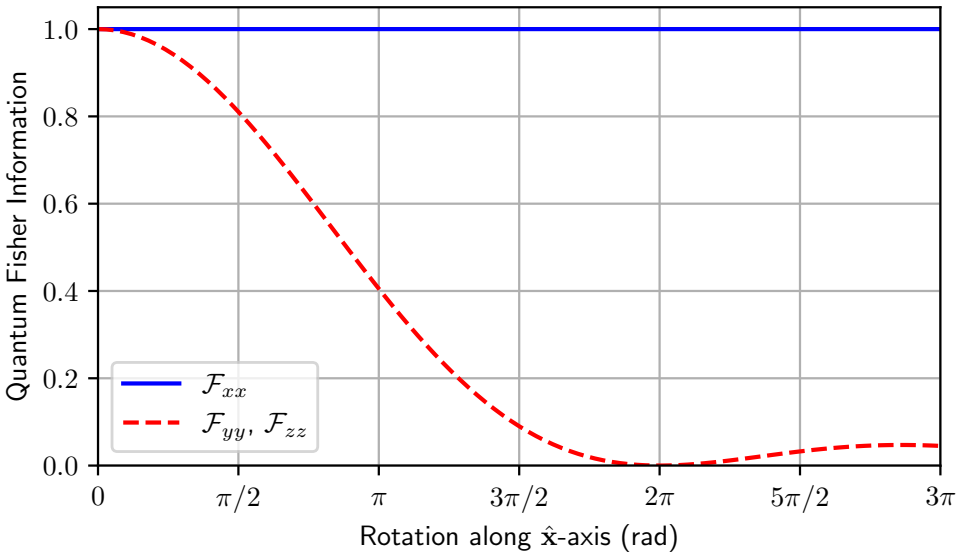

Figure 3.6: **Quantum Fisher information matrix for tri-axis sensor states.** The horizontal axis is the amount of the rotation along the $\hat{\boldsymbol{x}}$-axis. The blue solid line shows the quantum Fisher information along the same axis, which is constantly 1. The red dashed line shows the quantum Fisher information along the other two axes, which decreases as the amount of rotation along the $\hat{\boldsymbol{x}}$-axis increases.

The diagonal components of the quantum Fisher information matrix are shown in Fig. (3.6). We conclude that in the small angle limit, the sensor is equally sensitive to three components. The three components can be estimated simultaneously. Once one of the components gets large ($\alpha > \pi/2$), the tri-axis sensor becomes saturated, in which case the sensitivity regarding the remaining two components decreases. In the deep saturation limit ($\alpha \gg 2\pi$), the sensor becomes effectively a single-axis sensor. But this single-axis sensor still has the agnostic feature - no prior knowledge about the rotation axis is needed for estimating the amount of the rotation.

Chapter 4: Positronium Sensing

4.1 Introduction

So far, our discussion has been focusing on the probe-ancilla paradigm. Imagine a system with both the qubits interacting with the unknown rotation, Is there a way we could gain an advantage? Let's briefly revisit the rotational invariance of the singlet states.

$$(U \otimes U^{\dagger}) \left|\Psi^{-}\right\rangle = (\det U) \left(U^{2} \otimes I\right) \left|\Psi^{-}\right\rangle . \tag{4.1}$$

Because the rotation is doubled, the Fisher information is boosted to 4.

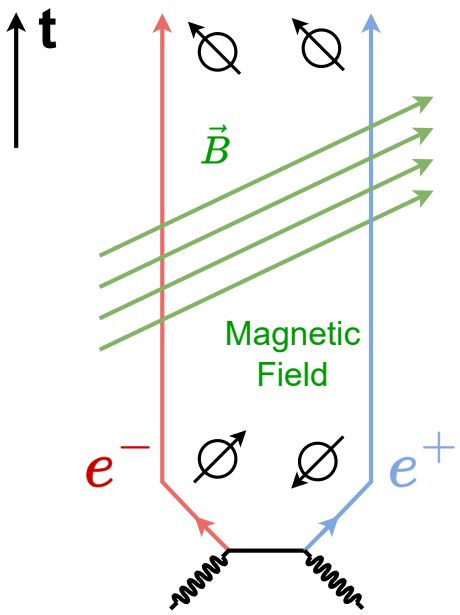

Figure 4.1: **Positronium sensing.** A pair of electron and positron are generated in the para-positronium state. Negelecting the orbital part, it is the singlet state. They interact with an unknown magnetic field. From the rotation of the two spins, one could extract information about the magnetic field.

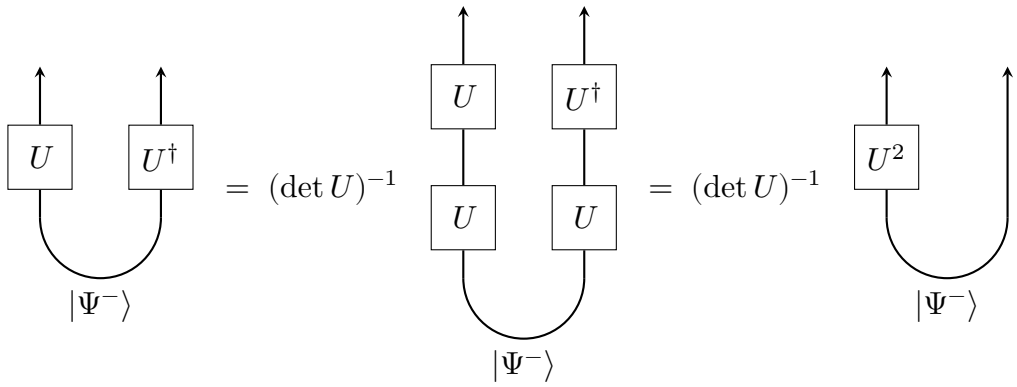

Figure 4.2: **Rotation doubling on singlet state.** Applying a unitary operation and the corresponding Hermitian conjugation on both of the qubits in a singlet state is equivalent to applying the unitary operation twice on one of the qubits (up to a global phase).

For the first part: in chapter one, we mentioned the charge conjugation symmetry for a superconductor. In this section, we utilize the charge conjugation in the context of a lumped element superconducting transmon qubit, which provide us with a natural platform to synthesize the analogue of a natural positron. For the second part, we employ the combination of quantum gates and AC Stark effect.

Such model exist in the nature, which is the positronium. Is there a way to implement the analogue of the positronium in the superconducting qubit? The task of implementing this analogue can be decomposed into two objects:

- Define the positronium state.
- Applying the correct interaction.

4.2 Lagrangian and Hamiltonian Formulism of a Transmon Circuit

The Lagrangian of the transmon circuit [60, 61] is written as

$$L = \frac{1}{2}C(V_1 - V_2)^2 + E_J \cos(\theta_1 - \theta_2) \tag{4.2}$$

where V_i represents the electric potential of the two nodes, and E_J is the Josephson energy stored in the Josephson junction. An ideal lumped-element capacitor features the quasi-equilibrium of electric potential and chemical potential [1]

$$0 = -2eV_i + \mu_i = -2eV_i - \hbar\partial_t\theta_i, \tag{4.3}$$

and

$$\begin{aligned} L &= \frac{\hbar^2 C}{8e^2}(\partial_t\theta_1 - \partial_t\theta_2)^2 + E_J\cos(\theta_1 - \theta_2) \\ &= \frac{\hbar^2}{16E_C}(\partial_t\theta)^2 + E_J\cos\theta \end{aligned} \tag{4.4}$$

where $\theta = \theta_1 - \theta_2$ is the phase difference across the junction and $E_C = e^2/2C$ is the charge energy. The Lagrangian exhibits the *electron-hole symmetry* inherent from the superconductor physics discussed in chapter 1,

$$\theta \to -\theta, \quad L \to L. \tag{4.5}$$

The conjugate momentum,

$$\frac{\partial L}{\partial(\partial_t\theta)} = \frac{\hbar^2}{8E_C}\partial_t\theta = -\hbar n, \tag{4.6}$$

has the meaning of number of Cooper pairs tunneled through the junction. Performing Legendre transform

$$H = \frac{\partial L}{\partial(\partial_t\theta)}\partial_t\theta - L = 4E_C n^2 - E_J\cos\theta, \tag{4.7}$$

The Hamilonian also has the electron-hole symmetry inherent from the Lagrangian

$$\theta \to -\theta, \quad n \to -n, \quad H \to H. \tag{4.8}$$

The transformation above is also refered to as the *charge conjugation*.

The Lagrangian of the transmon circuit coupled to a voltage drive can be described by

$$\begin{aligned} L &= \frac{1}{2}CV^2 + E_J\cos\theta + \frac{1}{2}C_g\left[V - V_d(t)\right]^2 \\ &= \frac{\hbar^2}{8e^2}C(\partial_t\theta)^2 + E_J\cos\theta + \frac{1}{2}C_g\left[\frac{\hbar}{2e}\partial_t\theta + V_d(t)\right]^2 \end{aligned} \tag{4.9}$$

[1] This equation can be derived from Eq. (1.36) by neglecting the acceleration process of the Cooper pairs.

The Hamiltonian of the transmon circuit coupled to a voltage drive can be described by

$$\begin{aligned} H &= 4E_C n^2 - E_J \cos\theta + \frac{1}{2} C_g \left(\frac{\hbar}{2e} \partial_t \theta + V_d(t) \right)^2 \\ &\simeq 4E_C n^2 - E_J \cos\theta - \frac{2eC_g}{C} n V_d(t) \end{aligned} \tag{4.10}$$

where

$$E_C = \frac{e^2}{2(C + C_g)}, \tag{4.11}$$

is understood as the total charge energy. We conclude that by changing the sign of θ and n, the sign of the coupling term is also reversed.

Under the charge conjugation, the lowest energy levels of a superconducting transmon circuit transform as

$$|g\rangle \to |g\rangle\,, \quad |e\rangle \to -|e\rangle\,, \quad |f\rangle \to |f\rangle\,, \quad |h\rangle \to -|h\rangle\,, \ldots\,. \tag{4.12}$$

In the computational space spanned by the lowest two eigenstates, the above charge conjugation is simply π-rotation along the $\hat{z}$-axis. To sum up, π-rotation along the $\hat{z}$-axis on a superconducting transmon qubit is equivalent to transforming an electron to a positron. However, the anti-transmon state prepared in this way doesn't yet allow us to reverse the rotation along the $\hat{z}$-axis. In order to tackle this problem, we introduce a simultaneous AC Stark shift tone on both of the qubits.

4.3 AC Stark Shift

The transmon Hamiltonian with the lowest three energy levels can be written as

$$H/\hbar = \omega_q^g |g\rangle\langle g| + \omega_q^e |e\rangle\langle e| + \omega_q^f |f\rangle\langle f|\,. \tag{4.13}$$

We couple the system with an external off-resonance microwave drive with frequency ω_s. The total Hamiltonian under rotating wave approximation is written as

$$\begin{aligned} H/\hbar = {} & \omega_q^g |g\rangle\langle g| + \omega_q^e |e\rangle\langle e| + \omega_q^f |f\rangle\langle f| \\ & + \omega_s a_s^\dagger a_s + \left(g_{qs}^{ge} |e\rangle\langle g|\, a_s + \text{H.c.} \right) + \left(g_{qs}^{ef} |f\rangle\langle e|\, a_s + \text{H.c.} \right), \end{aligned} \tag{4.14}$$

where "H.c." represents the Hermitian conjugation of the prior term. The eigenstates of the coupled Hamiltonian are called the *the dressed states.* Similar to the dispersive coupling, to analyze the energy of these states, it suffices to investigate the following 3-by-3 matrix blocks

$$H/\hbar = \begin{pmatrix} \omega_q^g + (n+1)\omega_s & g_{qs}^{ge}\sqrt{n+1} & 0 \\ g_{qs}^{ge*}\sqrt{n+1} & \omega_q^e + n\omega_s & g_{qs}^{ef}\sqrt{n} \\ 0 & g_{qs}^{ef*}\sqrt{n} & \omega_q^f + (n-1)\omega_s \end{pmatrix}. \tag{4.15}$$

We introduce the Rabi frequencies when in resonance

$$\Omega_s^{ge} = 2|g_{qs}^{ge}|\sqrt{n+1}, \quad \Omega_s^{ef} = 2\left|g_{qs}^{ef}\right|\sqrt{n+1}. \tag{4.16}$$

The Rabi frequency is proportional to the square root of photon number plus one [62].

The perturbation vanishes in the first order. We apply the second-order perturbation theory. The shift in the qubit frequency is dependent on the number of photons in the ω_s mode,

$$\Delta\omega_{qs}^{g,n+1} = \frac{|\langle e,n|H_s|g,n+1\rangle|^2}{\omega_q^g - \omega_q^e + \omega_s} = -\frac{|g_{qs}^{ge}|^2(n+1)}{\omega_{ge} - \omega_s} \tag{4.17}$$

$$\begin{aligned} \Delta\omega_{qs}^{e,n} &= \frac{|\langle g,n+1|H_s|e,n\rangle|^2}{\omega_q^e - \omega_q^g - \omega_s} + \frac{|\langle f,n-1|H_s|e,n\rangle|^2}{\omega_q^e - \omega_q^f + \omega_s} \\ &= \frac{|g_{qs}^{ge}|^2(n+1)}{\omega_{ge} - \omega_s} - \frac{\left|g_{qs}^{ef}\right|^2 n}{\omega_{ef} - \omega_s}. \end{aligned} \tag{4.18}$$

We study the qubit transition frequency where the number of photons is unchanged

$$\begin{aligned} \Delta\omega_q^{ge} &= \Delta\omega_{qs}^{e,n+1} - \Delta\omega_{qs}^{g,n+1} \\ &= \frac{|g_{qs}^{ge}|^2(2n+3)}{\omega_{ge} - \omega_s} - \frac{\left|g_{qs}^{ef}\right|^2(n+1)}{\omega_{ef} - \omega_s} \end{aligned} \tag{4.19}$$

We assume the AC stark tone has large amount of photons, in which case $n \gg 1$, we can approximate

$$\begin{aligned} \Delta\omega_q^{ge} &\simeq \frac{|g_{qs}^{ge}|^2(2n+2)}{\omega_{ge} - \omega_s} - \frac{\left|g_{qs}^{ef}\right|^2(n+1)}{\omega_{ef} - \omega_s} \\ &= \frac{(\Omega_s^{ge})^2}{2(\omega_{ge} - \omega_s)} - \frac{(\Omega_s^{ef})^2}{4(\omega_{ef} - \omega_s)}, \end{aligned} \tag{4.20}$$

Since Rabi frequency is also approximately proportional to the square root of the excitation number plus one for an anharmonic oscillator, we could use

$$\Omega_s^{ef} = \sqrt{2}\Omega_s^{ge} \tag{4.21}$$

To obtain the approximate formula [63]

$$\Delta\omega_{ge} \simeq \frac{(\Omega_s^{ge})^2}{2}\left(\frac{1}{\omega_{ge}-\omega_s} - \frac{1}{\omega_{ef}-\omega_s}\right) \tag{4.22}$$

Near resonance, the above perturbation result breaks down, but the influence of the AC Stark effect generally exists. The qubit frequency under Rabi drive or gate operations is generally different from the original qubit frequency determined by the Ramsey measurement. The amount of the deviation is usually on the order of a few hundred kHz. This becomes one of the sources of the phase errors. We will come back to this problem later.

For our experiment, we select a special frequency for the AC Stark tone which is able to induce exactly an equal amount of frequency shift in opposite directions on the two transmon qubits. This technique is used to implement opposite rotations along the z-axis for the two qubits. Combining the AC Stark shift part with the π-rotation along the z-axis, we implement the analogue of positronium coupled to an external vector magnetic field. By utilizing this coupling involving two transmon qubits, we achieved improved Fisher information value predicted by Eq. (4.1).

Chapter 5: Experimental Setup

5.1 Device

The device is superconducting aluminum-based. The probe qubit is a fixed-frequency qubit, coupled to a drive line and a readout cavity. The ancilla qubit is a flux-tunable qubit, coupled to a fast flux line in addition to a drive line and a readout cavity. Both of the qubits are coupled through a bus resonator. Physically, the two qubits correspond to two of the three qubits on the chip.

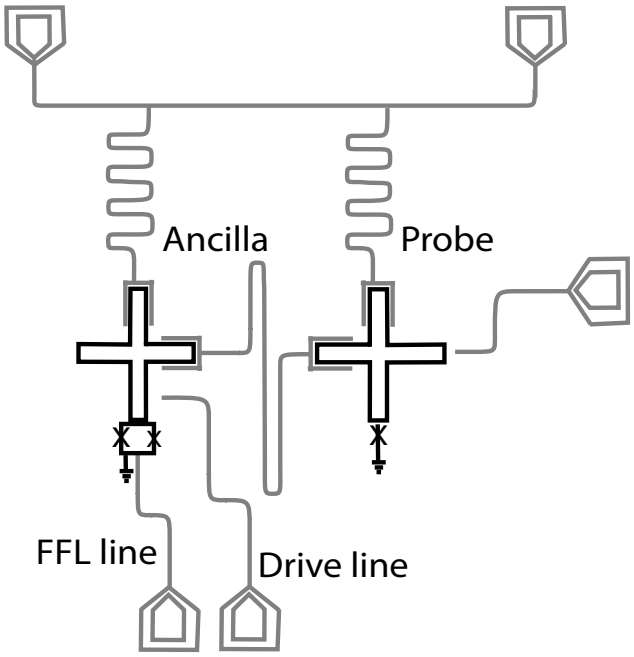

Figure 5.1: Schematic of the device.

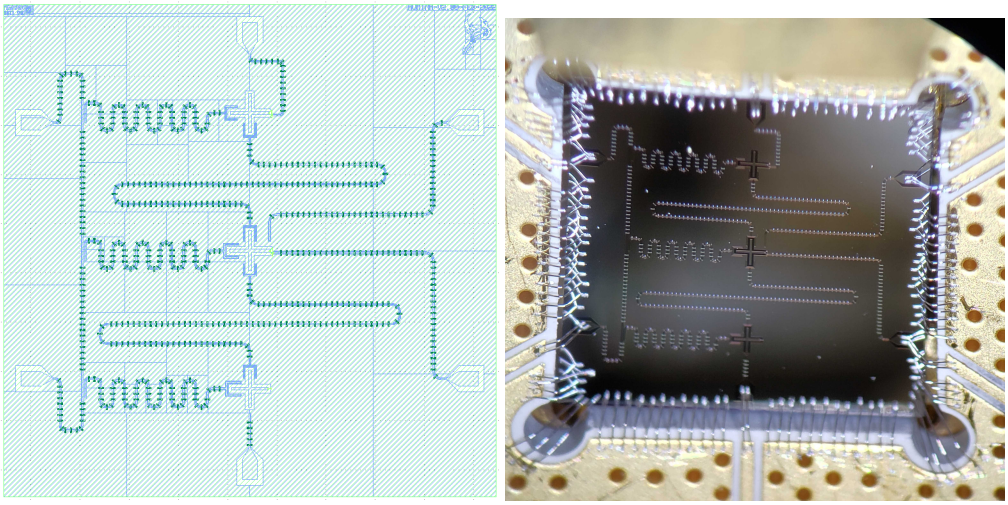

(a) (b)

Figure 5.2: (a) The chip design layout. (b) Microscopic image of the chip.

5.2 Setup

We utilize superconducting qubits for the experimental research. The parameters are included in the table Tab. (5.1). The low-noise amplification is assisted by a traveling-wave parametric amplifier based on the SNAIL (Superconducting Nonlinear Asymmetric Inductive eLements) architecture [64].

	$\omega_q/2\pi$ (GHz)	$\lvert\alpha\rvert/2\pi$ (MHz)	$\chi_{qc}/2\pi$ (kHz)	$\omega_c/2\pi$ (GHz)	$\kappa/2\pi$ (kHz)	T_1 (μs)	T_2^* (μs)
Ancilla	4.2	212	230	6.94	270	32	41
Probe	4.65	180	250	7.09	206	31	39

Table 5.1: **Measured parameters of the device used in the experiment.**

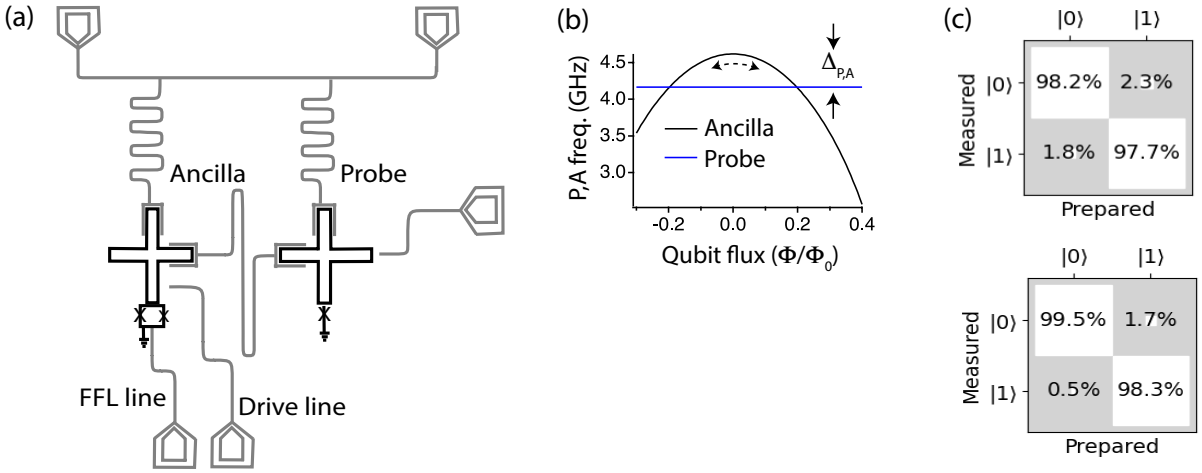

Figure 5.3

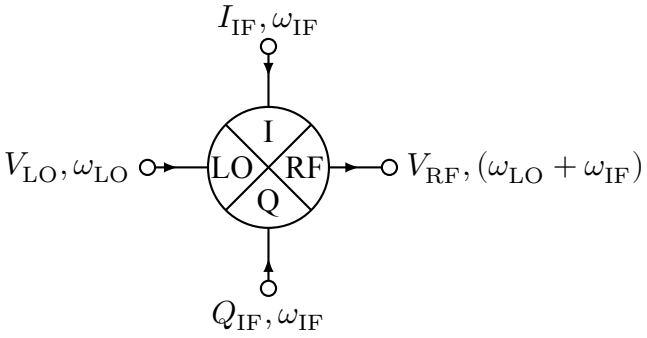

Figure 5.4: IQ mixer for up-conversion.

5.3 Mixer Calibrations

This section focuses on using IQ mixer for frequency up-conversion [65]. The output from RF port can be modeled as

$$V_{\mathrm{RF}}(t) = K_{\mathrm{I}} I_{\mathrm{IF}}(t) V_{\mathrm{LO}}(t) - K_{\mathrm{Q}} \tilde{\mathrm{Q}}(t) V'_{\mathrm{LO}}(t) + G_{\mathrm{LO}} V_{\mathrm{LO}}(t), \tag{5.1}$$

where $V_{\mathrm{LO},90}(t)$ represents $V_{\mathrm{LO}}(t)$ with ideally an 90° phase shift, $V_{\mathrm{LO,leak}}(t)$ represents the LO leakage into V_{RF}. We focus on the case where the signals are approximated by monochromatic

sinusoidal microwaves, in which case we can write down

$$\begin{aligned} V_{\mathrm{LO}}(t) &= A_{\mathrm{LO}}\cos(\omega_{\mathrm{LO}}t), \\ V_{\mathrm{LO},90}(t) &= A_{\mathrm{LO}}\sin\big(\omega_{\mathrm{LO}}t+\phi_{\mathrm{LO},90}\big), \\ V_{\mathrm{LO,leak}}(t) &= A_{\mathrm{LO}}\cos\big(\omega_{\mathrm{LO}}t+\phi_{\mathrm{LO,leak}}\big) \end{aligned} \tag{5.2}$$

where in general, $\phi_{\mathrm{LO},90} = \phi_{\mathrm{LO},90}(\omega_{\mathrm{LO}}) \neq 0$ for a realistic IQ mixer, which characterizes the non-orthogonality of the I, Q components. We also expect $K_{\mathrm{I}} \neq K_{\mathrm{Q}}$ which characterizes the imbalance of the two components. The non-orthogonality and imbalance cause the image frequency. Non-zero G_{LO} characterizes the LO leakage.

The formula for the microwave signal generated by the arbitrary wave generator can be expressed as

$$\begin{pmatrix} I_{\mathrm{IF}} \\ Q_{\mathrm{IF}} \end{pmatrix} = \begin{pmatrix} C_{00} & C_{01} \\ C_{10} & C_{11} \end{pmatrix} \begin{pmatrix} \cos(\omega_{\mathrm{IF}}t+\phi_F) \\ \sin(\omega_{\mathrm{IF}}t+\phi_F) \end{pmatrix} \begin{pmatrix} A_{00} & A_{01} \\ A_{10} & A_{11} \end{pmatrix} \begin{pmatrix} I_{\mathrm{mod}} \\ Q_{\mathrm{mod}} \end{pmatrix} + \begin{pmatrix} I_{\mathrm{DC}} \\ Q_{\mathrm{DC}} \end{pmatrix}, \tag{5.3}$$

where $I_{\mathrm{mod}}(t)$ and $Q_{\mathrm{mod}}(t)$ could be undstood as the envelop of the pulse waveform. The amplitude transform matrix A is for adjusting the amplitude and phase of the pulse. By choosing the appropriate mixer correction C matrix and DC components, we are able to cancel out both the LO leakage and the image frequency. To simplify the problem, we assume the amplitude transform matrix takes the simple form of an identity matrix, and the pulse only involves in-phase component $I(t) = A_{\mathrm{mod}}(t), Q(t) = 0$. The above formula simplifies to

$$\begin{pmatrix} I_{\mathrm{IF}} \\ Q_{\mathrm{IF}} \end{pmatrix} = \begin{pmatrix} 1 & 0 \\ G\sin\theta & G\cos\theta \end{pmatrix} \begin{pmatrix} \cos(\omega_{\mathrm{IF}}t) \\ \sin(\omega_{\mathrm{IF}}t) \end{pmatrix} A_{\mathrm{mod}} + \begin{pmatrix} I_{\mathrm{DC}} \\ Q_{\mathrm{DC}} \end{pmatrix}, \tag{5.4}$$

Substitute Eq. (5.4) into Eq. (5.1), we obtain

$$
\begin{aligned}
&V_{\mathrm{RF}} \\
&= K_{\mathrm{I}} A_{\mathrm{LO}} \left[A_{\mathrm{mod}} \cos(\omega_{\mathrm{IF}} t) + I_{\mathrm{DC}}\right] \cos(\omega_{\mathrm{LO}} t) \\
&\quad - K_{\mathrm{Q}} A_{\mathrm{LO}} \left[G A_{\mathrm{mod}} \sin(\omega_{\mathrm{IF}} t + \theta) + Q_{\mathrm{DC}}\right] \sin\left(\omega_{\mathrm{LO}} t + \phi_{\mathrm{LO},90}\right) \\
&\quad + G_{\mathrm{LO}} A_{\mathrm{LO}} \cos\left(\omega_{\mathrm{LO}} t + \phi_{\mathrm{LO,leak}}\right) \\
&= \frac{1}{2} K_{\mathrm{I}} A_{\mathrm{LO}} A_{\mathrm{mod}} \left\{\cos[(\omega_{\mathrm{LO}} + \omega_{\mathrm{IF}})t] + \cos[(\omega_{\mathrm{LO}} - \omega_{\mathrm{IF}})t]\right\} \\
&\quad + \frac{1}{2} K_{\mathrm{Q}} G A_{\mathrm{LO}} A_{\mathrm{mod}} \left\{\cos[(\omega_{\mathrm{LO}} + \omega_{\mathrm{IF}})t + \phi_{\mathrm{LO},90} + \theta] - \cos[(\omega_{\mathrm{LO}} - \omega_{\mathrm{IF}})t + \phi_{\mathrm{LO},90} - \theta]\right\} \\
&\quad + A_{\mathrm{LO}} \left[G_{\mathrm{LO}} \cos\left(\omega_{\mathrm{LO}} t + \phi_{\mathrm{LO,leak}}\right) + K_{\mathrm{I}} I_{\mathrm{DC}} \cos(\omega_{\mathrm{LO}} t) + K_{\mathrm{Q}} Q_{\mathrm{DC}} \sin\left(\omega_{\mathrm{LO}} t + \phi_{\mathrm{LO},90}\right)\right]
\end{aligned}
\tag{5.5}
$$

To verify the set of parameters is able to simultaneously cancel the image frequency and LO leakage, we apply

$$
\begin{aligned}
G &= \frac{K_{\mathrm{I}}}{K_{\mathrm{Q}}}, \\
\theta &= \phi_{\mathrm{LO},90}, \\
I_{\mathrm{DC}} &= -\frac{G_{\mathrm{LO}}}{K_{\mathrm{I}}} \left(\cos\phi_{\mathrm{LO,leak}} + \tan\phi_{\mathrm{LO},90}\right), \\
Q_{\mathrm{DC}} &= \frac{G_{\mathrm{LO}} \sin\phi_{\mathrm{LO,leak}}}{K_{\mathrm{Q}} \cos\phi_{\mathrm{LO},90}}.
\end{aligned}
\tag{5.6}
$$

With these values

$$
V_{\mathrm{RF}} = A_{\mathrm{RF}} \cos\left[(\omega_{\mathrm{LO}} + \omega_{\mathrm{IF}})t - \phi_{\mathrm{LO},90}\right], \tag{5.7}
$$

where

$$
A_{\mathrm{RF}} = A_{\mathrm{LO}} A_{\mathrm{mod}} K_{\mathrm{I}} \cos\phi_{\mathrm{LO},90}. \tag{5.8}
$$

We automatically optimize these parameters with optimizers from Nevergrad [66].

5.4 Heterodyne Readout

In the readout process, the mixer is used in the opposite way.

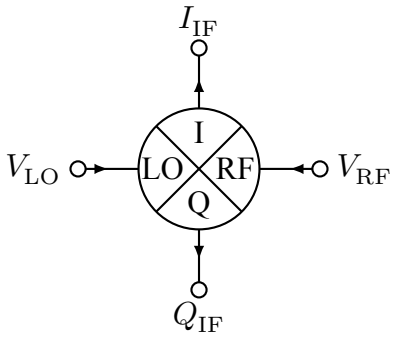

Figure 5.5: IQ mixer for downconversion.

Unlike homodyne measurements, hetrodyne measurement operates at non-zero IF frequency which makes it more robust against low-frequency fluctuations in the setup. The essence of Heterodyne measruement is the phase throughout the demodulation branch has to be consistent with the readout pulse from the upconversion mixer. For homodyne measurements, this is could be done by using the same microwave generator, and use a microwave splitter to allocate the power into both of the LO ports of the input and readout mixers. For Heterodyne readout, the same technique is employed. In addition, the phase of the readout pulse and the integration weights have to be either fixed or consistently accumulating. Once setup, the readout record from hetrodyne measurement is processed similarly to the method used in homodyne measurement.

Traditionally, the readout record is integrated over time to produce a pair of I and Q values, which is used to distinguish the quantum state of the qubit. To improve over this paradigm, we could explore more details about the readout record.

5.5 Integration Weights

The readout record signal from the mixers is not featureless. It is structured with certain self-correlation. This can be visualized by ploting the covariance matrix of the readout record. The covariance matrix has non-zero off-diagnonal components, displaying correlated feature.

A customized integration weight is able to efficiently extract the information from the record by

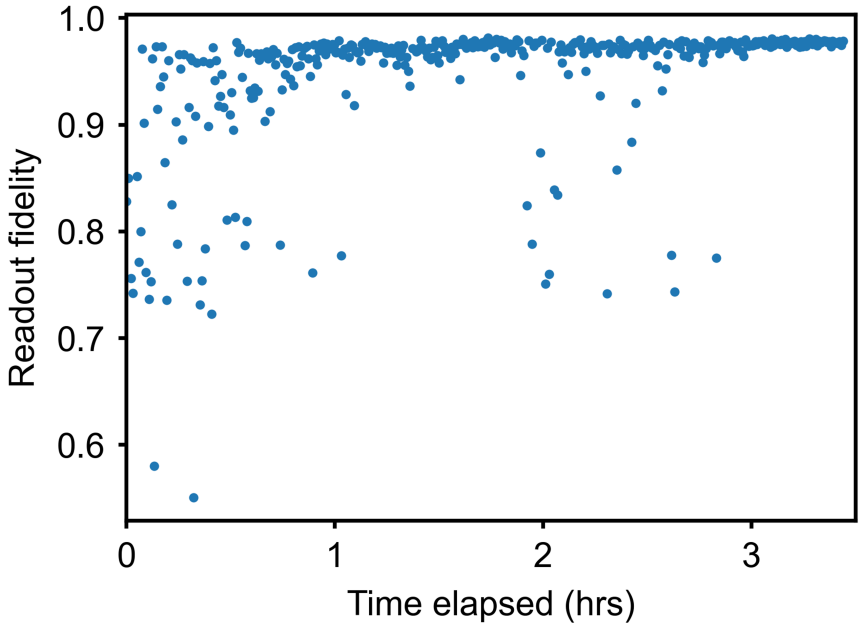

(a)

Figure 5.6: **Readout optimization.**

projecting it into the correct basis. In order to determine the integration weights, the algorithms we have tested are principle component analysis and linear discriminator analysis.

After the integration weights are determined, we prepare a dataset. Half of the data is used as the training set to feed into an opensource classifier. Two options tested to be exellent for two or three qubits are *Random Forest* and *Histogram Gradient Boosting* from scikit-learn [67–71]. The remaining half is used as the test set used to obtain the response matrix R.

5.6 Active Reset

After the readout of the qubits is calibrated, we could utilize the readout to perform more efficient qubit state reset in a feedback protocol. With properly setting up the active reset, the initial state fidelity should be better than the thermal equilibrium. Especially, through tuning the threshold, given the readout is sufficiently stable, such advantage is observed without extremely high readout fidelity ($> 99\%$).

5.7 Readout Corrections

The readout fidelity is represented by the response matrix R. The entries of R is defined as the conditional probability

$$R_{ij} = P(\text{measure } i|\text{truth is } j). \tag{5.9}$$

We apply a method known as Iterative Beyesian Update (IBU) [72]. The response matrix is calibrated for the readout classifiers. The corrected probability distribution t_i^{n+1} is calculated from the iteration

$$\begin{aligned} t_i^{n+1} &= \sum_j P(\text{truth is } i|\text{measure } j) \times m_j \\ &= \sum_j \frac{R_{ji} t_i^n}{\sum_k R_{jk} t_k^n} \times m_j, \end{aligned} \tag{5.10}$$

where m_j is the measured raw probability distribution without correction. The initial value t_i^0 could be chosen as the uniform distribution. The iteration usually converges within 20 steps.

The key benefits of IBU are twofold. First, unlike direct matrix inversion, it gracefully handles unphysical probability estimates (i.e. cases where $P > 1$ or $P < 0$). Second, since it is inherently iterative, IBU can be implemented on FPGA-based hardware without reliance on full-fledged linear algebra libraries.

5.8 Spectral Filtering for Pulses

We define the cosine pulse in the discrete form

$$u(n) = 1 - \cos\frac{(2n+1)\pi}{N}, \quad 0 \le n \le N-1, \tag{5.11}$$

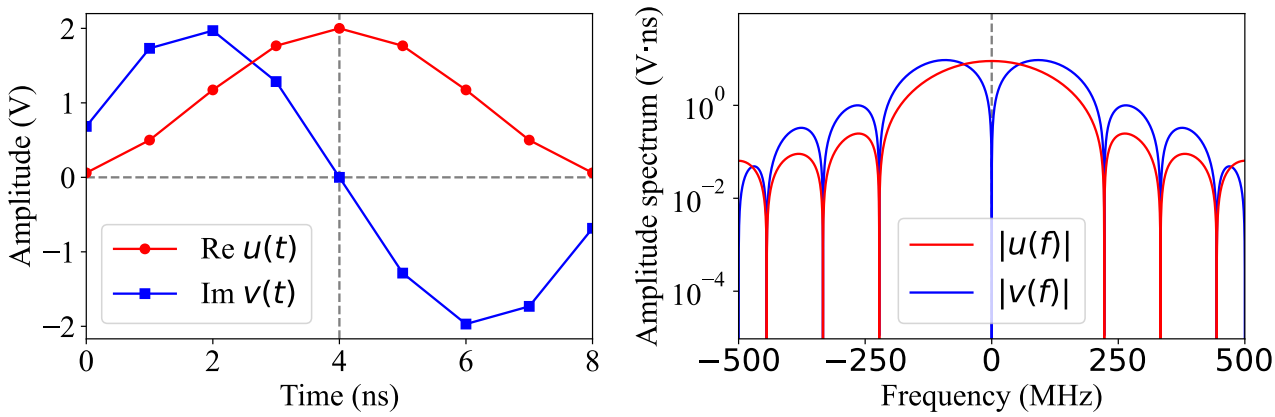

Figure 5.7: **Cosine pulse and the derivative.** (a) The pulse waveforms u and v in the time domain. Each waveform consists of 9 data points, sampled at 1 GHz sampling rate. (b) The Fourier transforms of the pulse waveforms. The spectrum of u and v share the same set of zeros except for the origin and the boundary. The zeros are displayed as dips in the logarithmic scale. The unit of the vertical axis is voltage times nanosecond, the same as magnetic flux.

where N is the length of the pulse, and the pulse is defined to be zero when n is beyond the given range. The Fourier transform is

$$\begin{aligned} u(\omega) &= \tau \sum_{n=0}^{N-1} u(n) \mathrm{e}^{-\mathrm{j}\,(2n-N+1)\omega\tau/2}, \\ &= \frac{\tau}{2} \sum_{n=0}^{N-1} \left(2 - \mathrm{e}^{\mathrm{j}\,(2n+1)\pi/N} - \mathrm{e}^{-\mathrm{j}\,(2n+1)\pi/N}\right) \mathrm{e}^{-\mathrm{j}\,(2n-N+1)\omega\tau/2} \\ &= \frac{\tau \sin^2 \dfrac{\pi}{2N} \sin \dfrac{N\omega\tau}{2} \left(1 + 2\cos\dfrac{\pi}{N} + \cos\omega\tau\right)}{\sin\dfrac{\omega\tau}{2} \sin\left(\dfrac{\pi}{N} + \dfrac{\omega\tau}{2}\right) \sin\left(\dfrac{\pi}{N} - \dfrac{\omega\tau}{2}\right)}, \end{aligned} \tag{5.12}$$

where j is the imaginary unit[1] and τ is the sampling interval, usually taken to be 1 nanosecond for a typical arbitrary wave generator. Physically, the real and imaginary part of the waveform correspond to the in-phase and quadrature components of the signal, respectively. For convenience, we have aligned the timing of the Fourier transform with the center of the time index.

We define a second function that is proportional to the time derivative of the cosine pulse

$$v(n) = 2\,\mathrm{j}\,\sin\frac{(2n+1)\pi}{N}, \quad 0 \le n \le N-1 \tag{5.13}$$

[1]We distinguish between i and j because the imaginary unit is often defined differently depending on the context. For example, in quantum mechanics the time evolution is conventionally denoted as $e^{-\mathrm{i}\,\omega t}$, while in engineering the similar expression is typically denoted as $e^{\mathrm{j}\,\omega t}$.

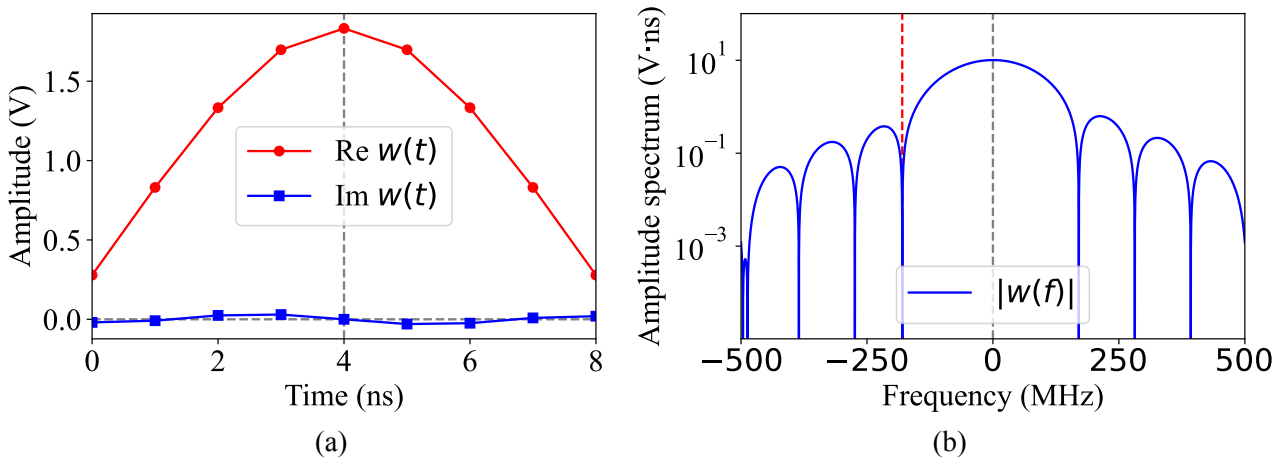

Figure 5.8: **Spectrally filtered pulse.** (a) The real and imaginay part of the spectrally filtered pulse w. The pulse is obtained as the linear combination of u and v through Eq. (5.16) with parameters $\theta = -0.1310\pi$ and $\omega_0 = -0.1035\pi$. These parameters are obtained with numerical optimization. (b) The Fourier transform of w. The frequency component at the transmon anharmonicity $\alpha = -180$ MHz is suppressed, as indicated by the red dashed line.

With the Fourier transform

$$\begin{aligned} v(\omega) &= \tau \sum_{n=0}^{N-1} v(n) \mathrm{e}^{-\mathrm{j}\,(2n-N+1)\omega\tau/2}, \\ &= \tau \sum_{n=0}^{N-1} \left(\mathrm{e}^{\mathrm{j}\,(2n+1)\pi/N} - \mathrm{e}^{-\mathrm{j}\,(2n+1)\pi/N}\right) \mathrm{e}^{-\mathrm{j}\,(2n-N+1)\omega\tau/2} \\ &= -\frac{2\tau \sin\dfrac{\pi}{N} \cos\dfrac{\omega\tau}{2} \sin\dfrac{N\omega\tau}{2}}{\sin\left(\dfrac{\pi}{N} + \dfrac{\omega\tau}{2}\right) \sin\left(\dfrac{\pi}{N} - \dfrac{\omega\tau}{2}\right)} \end{aligned} \tag{5.14}$$

We could verify their ratio

$$\frac{v(\omega)}{u(\omega)} = -\frac{2\sin\omega\tau}{\tan\dfrac{\pi}{2N}\left(1 + 2\cos\dfrac{\pi}{N} + \cos\omega\tau\right)} \tag{5.15}$$

Which is non-zero except at $\omega = 0$ in the Nyquist zone $|\omega| < \pi/\tau$, when $N \geq 3$. This means the spectrum of u and v share almost exactly the same set of zeros. This nice property enables us to use linear combination of u and v to cancel out a unwanted frequency component.

We define the pulse in the form of

$$w(N, \theta, \omega_0; n) = \left[\cos\theta \cdot u(n) + \sin\theta \cdot v(n)\right] \mathrm{e}^{\mathrm{j}\,(2n-N+1)\omega_0\tau/2} \tag{5.16}$$

as the building block of more complicated pulses. The parameter θ is determined by

$$\tan\theta = -\frac{u(\omega_1 - \omega_0)}{v(\omega_1 - \omega_0)}, \tag{5.17}$$

where ω_1 is the unwanted frequency component to be suppressed, and ω_0 adjusts the frequency of the main lobe. By carefully choosing both θ and ω_0, we are able to synthesize a pulse without the unwanted frequency component while maintaining zero overall detuning. This is done by numerical optimization using, for example, the L-BFGS-B algorithm from SciPy [73–75]. Fig. (5.8) shows the example of a pulse engineered to suppress the leakage into the second excited state.

Experimentally, longer pulses are often used because of the limitation of the output amplitude from the arbitrary wave generator (AWG). Longer pulses can be synthesized by convoluting multiple pieces together. The convolution of two functions $g_1(n)$ and $g_2(n)$ is define as

$$(g_1 * g_2)(n) = \sum_{m=-\infty}^{\infty} g_1(m) g_2(n-m). \tag{5.18}$$

The important property of convolution lies in the *convolution theorem* [76]:

$$(g_1 * g_2)(\omega) = g_1(\omega) g_2(\omega), \tag{5.19}$$

which implies the zeros in the spectrum of $(g_1 * g_2)$ is the combination of zeros of g_1 and g_2. An example of the pulses we use for the experiment is the convolution of three pieces

$$f(n) = A(w_1 * w_2 * sq)(n), \tag{5.20}$$

where A is a scaling factor and w_i represents a piece of pulse waveform given by Eq. (5.16) for suppressing a specific frequency component, sq represents a square waveform of certain length. This combined pulse is capable of canceling out multiple unwanted frequency components while having a flat top, making it more efficient than a Gaussian pulse on AWG with limited output amplitude. The combined pulse can be customized to fit with the purpose of specific experiment not limited to gate-based approach, for example, by replacing the square wave with time-dependent ones for the implementation of certain evolution. The number of w-pulses can also be changed.

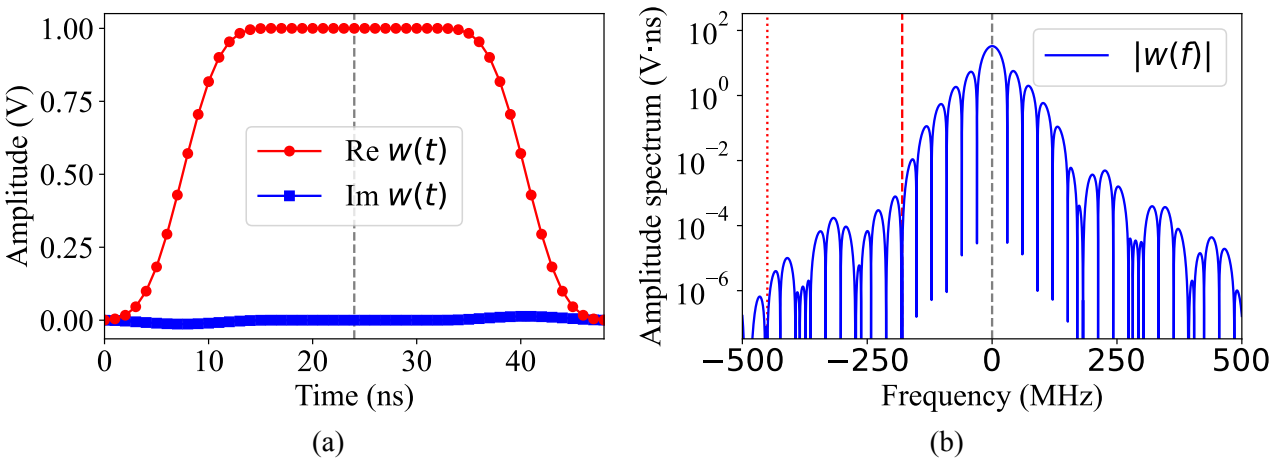

Figure 5.9: **Combined pulse.** (a) The real and imaginary parts of the combined pulse f. The pulse is an example Eq. (5.20) with w_1 and w_2 designed to suppress both the leakage to the second excited state and qubit crosstalk. (b) The Fourier transform of f. The spectral weight at the transmon anharmonicity $\alpha = -180$ MHz is suppressed, as indicated by the red dashed line. In addition, the spectral weight in resonance with the adjacent qubit which is at -450 MHz is suppressed, simultaneously, as indicated by the red dotted line.

Fig. (5.9) shows an example of a combined pulse design to suppress both the leakage to the second excited state and the crosstalk with an adjacent qubit. In the time domain, the pulse features smooth transitions at both the beginning and the end, with a flat top (Fig. (5.9a)). The steepness of the transitions are controlled by the total length of w_1 and w_2. The spectrum of the combined pulse has zeros both at the qubit anharmonicity and the resonance frequency of the adjacent qubit. In addition to these two specific frequencies, the pulse features the suppression of broadband frequency components as shown in the rapid decrease in the amplitude spectrum away from the main lobe (Fig. (5.9b)). As a comparison, the square wave contains a large amount of unwanted spectral weight, as is shown in the slowly decreasing baseline in the amplitude spectrum (Fig. (5.10b)).

The pulse generated by this approach is able to suppress leakage into unwanted quantum states. But phase error due to AC Stark shift needs to be compensated in other ways. We could use a pulse detuning to achieve this [77–79], which needs to be experimentally calibrated.

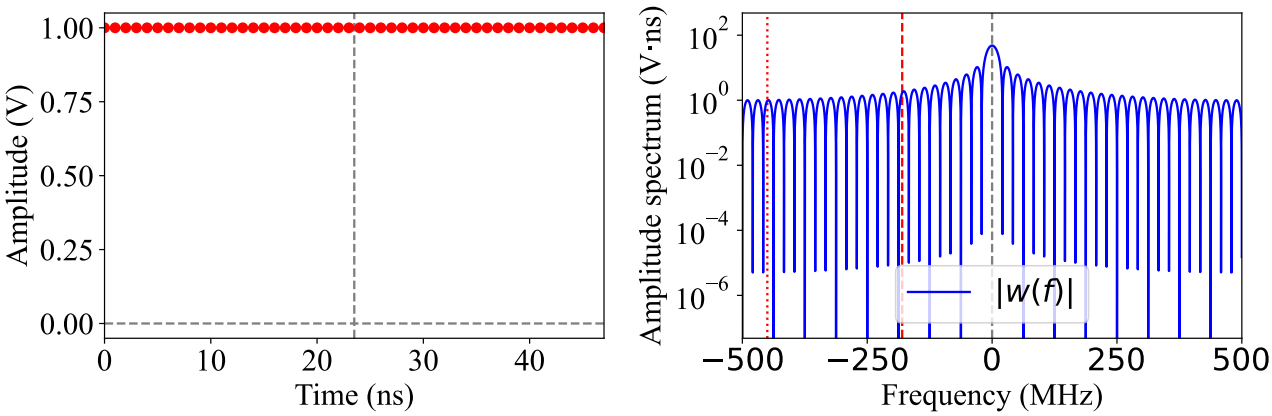

(a) (b)

Figure 5.10: **Square pulse.** (a) The square pulse waveform in the time domain. (b) The Fourier transform of of the square pulse. The frequency component at the transmon anharmonicity $\alpha = -180$ MHz is large, as indicated by the red dashed line. Same large amplitude is displayed near the resonance frequency of the adjacent qubit at -450 MHz (red dotted line).

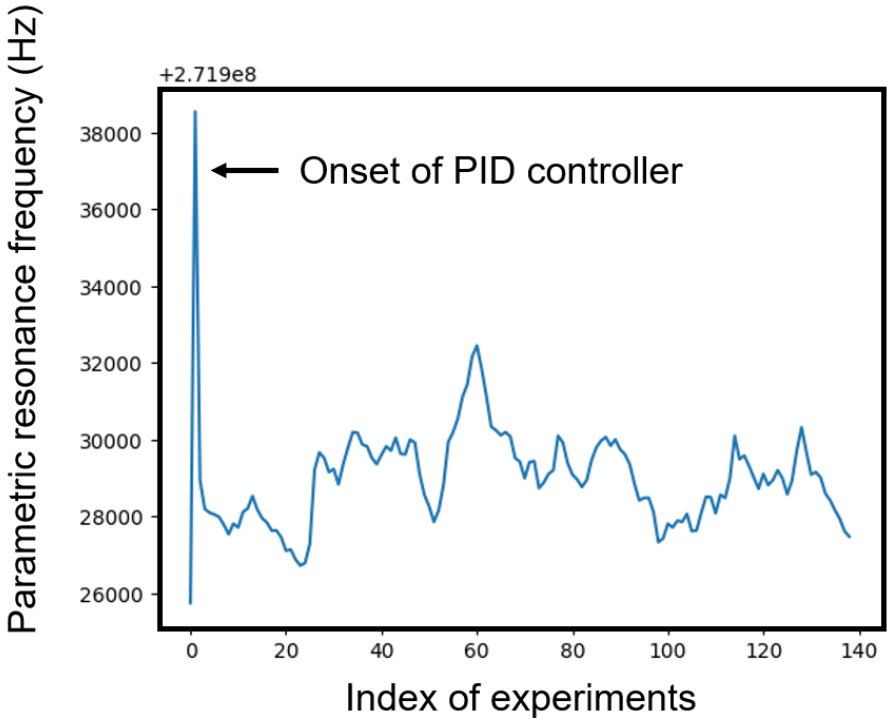

(a)

Figure 5.11: **Feedback control for parametric resonance.** The horizontal axis shows the index of the experiments, each separated by a few milliseconds. Real experiments is performed in a interleaved approach.

References

1. TriTertButoxy & Stannered. *Elementary particle interactions.svg* Published: Wikimedia Commons. https://en.m.wikipedia.org/wiki/File:Elementary_particle_interactions.svg (cited on p. 1).
2. Altland, A. & Simons, B. *Condensed matter field theory* 2nd ed. 770 pp. (Cambridge University Press, Cambridge ; New York, 2010) (cited on pp. 2, 12).
3. Wen, X.-G. *Quantum field theory of many-body systems: from the origin of sound to an origin of light and electrons* Repr. 505 pp. (Oxford University Press, Oxford, 2010) (cited on pp. 2, 12).
4. Tinkham, M. *Introduction to superconductivity* 2 ed. 454 pp. (Dover Publ, Mineola, NY, 2015) (cited on p. 2).
5. Annett, J. F. *Superconductivity, superfluids, and condensates* 186 pp. (Oxford University Press, Oxford ; New York, 2004) (cited on p. 2).
6. Bardeen, J., Cooper, L. N. & Schrieffer, J. R. Microscopic Theory of Superconductivity. *Physical Review* **106,** 162–164. doi:10.1103/PhysRev.106.162 (1957) (cited on p. 2).
7. Landau, L. D. in *Collected Papers of L.D. Landau* 546–568 (Elsevier, 1965). doi:10.1016/B978-0-08-010586-4.50078-X (cited on p. 2).
8. Abrikosov, A. A. On the Magnetic properties of superconductors of the second group. *Sov. Phys. JETP* **5,** 1174–1182 (1957) (cited on p. 2).
9. Gor'kov, L. P. Microscopic derivation of the Ginzburg–Landau equations in the theory of superconductivity. *Sov. Phys. - JETP (Engl. Transl.); (United States)* **9:6** (1959) (cited on p. 2).
10. Gödel, K. An Example of a New Type of Cosmological Solutions of Einstein's Field Equations of Gravitation. *Reviews of Modern Physics* **21,** 447–450. doi:10.1103/RevModPhys.21.447 (1949) (cited on p. 8).
11. Morris, M. S., Thorne, K. S. & Yurtsever, U. Wormholes, Time Machines, and the Weak Energy Condition. *Physical Review Letters* **61,** 1446–1449. doi:10.1103/PhysRevLett.61.1446 (1988) (cited on p. 8).
12. Deutsch, D. Quantum mechanics near closed timelike lines. *Physical Review D* **44,** 3197–3217. doi:10.1103/PhysRevD.44.3197 (1991) (cited on p. 8).

13. Bennett, C. H. in *Proceedings of QUPON* (Vienna, Austria, 2005) (cited on p. 8).

14. Svetlichny, G. Time Travel: Deutsch vs. Teleportation. *International Journal of Theoretical Physics* **50,** 3903–3914. doi:10.1007/s10773-011-0973-x (2011) (cited on p. 8).

15. Lloyd, S. *et al.* Closed Timelike Curves via Postselection: Theory and Experimental Test of Consistency. *Physical Review Letters* **106,** 040403. doi:10.1103/PhysRevLett.106.040403 (2011) (cited on p. 8).

16. Lloyd, S., Maccone, L., Garcia-Patron, R., Giovannetti, V. & Shikano, Y. Quantum mechanics of time travel through post-selected teleportation. *Physical Review D* **84,** 025007. doi:10.1103/PhysRevD.84.025007 (2011) (cited on p. 8).

17. Sommerfeld, A. Zur Quantentheorie der Spektrallinien. *Annalen der Physik* **356,** 1–94. doi:10.1002/andp.19163561702 (1916) (cited on p. 9).

18. Wilson, W. LXXXIII. *The quantum-theory of radiation and line spectra*. *The London, Edinburgh, and Dublin Philosophical Magazine and Journal of Science* **29,** 795–802. doi:10.1080/14786440608635362 (1915) (cited on p. 9).

19. Henneaux, M. & Teitelboim, C. *Quantization of Gauge Systems* doi:10.2307/j.ctv10crg0r (Princeton University Press, 2020) (cited on p. 9).

20. Peskin, M. E. & Schroeder, D. V. *An introduction to quantum field theory* 842 pp. (CRC Press, Taylor & Francis Group, Boca Raton London New York, 2019) (cited on pp. 9, 19).

21. Nambu, Y. Quasi-Particles and Gauge Invariance in the Theory of Superconductivity. *Physical Review* **117,** 648–663. doi:10.1103/PhysRev.117.648 (1960) (cited on p. 13).

22. Goldstone, J. Field theories with « Superconductor » solutions. *Il Nuovo Cimento* **19,** 154–164. doi:10.1007/BF02812722 (1961) (cited on p. 13).

23. Goldstone, J., Salam, A. & Weinberg, S. Broken Symmetries. *Physical Review* **127,** 965–970. doi:10.1103/PhysRev.127.965 (1962) (cited on p. 13).

24. Anderson, P. W. Coherent Excited States in the Theory of Superconductivity: Gauge Invariance and the Meissner Effect. *Physical Review* **110,** 827–835. doi:10.1103/PhysRev.110.827 (1958) (cited on p. 13).

25. Anderson, P. W. Random-Phase Approximation in the Theory of Superconductivity. *Physical Review* **112,** 1900–1916. doi:10.1103/PhysRev.112.1900 (1958) (cited on p. 13).

26. Bogoljubov, N. N., Tolmachov, V. V. & Širkov, D. V. A New Method in the Theory of Superconductivity. *Fortschritte der Physik* **6,** 605–682. doi:10.1002/prop.19580061102 (1958) (cited on p. 13).

27. London, F. & London, H. The electromagnetic equations of the supraconductor. *Proceedings of the Royal Society of London. Series A - Mathematical and Physical Sciences* **149,** 71–88. doi:10.1098/rspa.1935.0048 (1935) (cited on p. 14).

28. Feynman, R. P. *The Development of the Space-Time View of Quantum Electrodynamics: Nobel Lecture, December 11, 1965* Published: NobelPrize.org. https://www.nobelprize.org/prizes/physics/1965/feynman/lecture/ (cited on p. 18).

29. Srednicki, M. A. *Quantum field theory* 13th printing. 641 pp. (Cambridge Univ. Press, Cambridge, 2017) (cited on p. 19).

30. Fan, X., Myers, T. G., Sukra, B. A. D. & Gabrielse, G. Measurement of the Electron Magnetic Moment. *Physical Review Letters* **130,** 071801. doi:10.1103/PhysRevLett.130.071801 (2023) (cited on p. 21).

31. Gabrielse, G., Hanneke, D., Kinoshita, T., Nio, M. & Odom, B. New Determination of the Fine Structure Constant from the Electron *g* Value and QED. *Physical Review Letters* **97.** Erratum: Phys. Rev. Lett. 99, 039902 (2007)., 030802. doi:10.1103/PhysRevLett.97.030802 (2006) (cited on p. 21).

32. Landau, L. D. The moment of a two-photon system. Russian. *Dokl. Akad. Nauk SSSR* **60.** Original in Russian, 207–209 (1948) (cited on p. 21).

33. Yang, C. N. Selection Rules for the Dematerialization of a Particle into Two Photons. *Physical Review* **77,** 242–245. doi:10.1103/PhysRev.77.242 (1950) (cited on p. 21).

34. Zhao, Q. *et al.* Signatures of linear Breit-Wheeler pair production in polarized γ γ collisions. *Physical Review D* **105,** L071902. doi:10.1103/PhysRevD.105.L071902 (2022) (cited on p. 21).

35. Adam, J. *et al.* Measurement of e + e − Momentum and Angular Distributions from Linearly Polarized Photon Collisions. *Physical Review Letters* **127,** 052302. doi:10.1103/PhysRevLett.127.052302 (2021) (cited on p. 21).

36. Pike, O. J., Mackenroth, F., Hill, E. G. & Rose, S. J. A photon–photon collider in a vacuum hohlraum. *Nature Photonics* **8,** 434–436. doi:10.1038/nphoton.2014.95 (2014) (cited on p. 21).

37. Song, X., Salvati, F., Gaikwad, C., Yunger Halpern, N., Arvidsson-Shukur, D. R. M. & Murch, K. Agnostic Phase Estimation. *Physical Review Letters* **132,** 260801. doi:10.1103/PhysRevLett.132.260801 (2024) (cited on p. 21).

38. Ringbauer, M., Broome, M. A., Myers, C. R., White, A. G. & Ralph, T. C. Experimental simulation of closed timelike curves. *Nature Communications* **5,** 4145. doi:10.1038/ncomms5145 (2014) (cited on p. 22).

39. Marletto, C., Vedral, V., Virzì, S., Rebufello, E., Avella, A., Piacentini, F., Gramegna, M., Degiovanni, I. P. & Genovese, M. Theoretical description and experimental simulation of quantum entanglement near open time-like curves via pseudo-density operators. *Nature Communications* **10,** 182. doi:10.1038/s41467-018-08100-1 (2019) (cited on p. 22).

40. Kaiser, F., Coudreau, T., Milman, P., Ostrowsky, D. B. & Tanzilli, S. Entanglement-Enabled Delayed-Choice Experiment. *Science* **338,** 637–640. doi:10.1126/science.1226755 (2012) (cited on p. 22).

41. Lee, J.-C., Lim, H.-T., Hong, K.-H., Jeong, Y.-C., Kim, M. S. & Kim, Y.-H. Experimental demonstration of delayed-choice decoherence suppression. *Nature Communications* **5,** 4522. doi:10.1038/ncomms5522 (2014) (cited on p. 22).

42. Bennett, C. H., Brassard, G., Crépeau, C., Jozsa, R., Peres, A. & Wootters, W. K. Teleporting an unknown quantum state via dual classical and Einstein-Podolsky-Rosen channels. *Physical Review Letters* **70,** 1895–1899. doi:10.1103/PhysRevLett.70.1895 (1993) (cited on p. 23).

43. Nielsen, M. A. & Chuang, I. L. *Quantum computation and quantum information* 10th anniversary ed. 676 pp. (Cambridge University Press, Cambridge ; New York, 2010) (cited on pp. 23, 27, 41).

44. Cramér, H. *Mathematical methods of statistics Princeton mathematical series* **9** (Princeton university press, Princeton, 1991) (cited on p. 25).

45. Rao, C. R. in *Breakthroughs in Statistics* (eds Kotz, S. & Johnson, N. L.) Series Title: Springer Series in Statistics, 235–247 (Springer New York, New York, NY, 1992). doi:10.1007/978-1-4612-0919-5_16 (cited on p. 25).

46. Nakahara, M. *Geometry, topology, and physics* 2nd ed. OCLC: ocm52622950. 573 pp. (Institute of Physics Publishing, Bristol ; Philadelphia, 2003) (cited on p. 28).

47. Berry, M. V. Quantal phase factors accompanying adiabatic changes. *Proceedings of the Royal Society of London. A. Mathematical and Physical Sciences* **392,** 45–57. doi:10.1098/rspa.1984.0023 (1984) (cited on p. 28).

48. Naghiloo, M., Jordan, A. N. & Murch, K. W. Achieving Optimal Quantum Acceleration of Frequency Estimation Using Adaptive Coherent Control. *Physical Review Letters* **119,** 180801. doi:10.1103/PhysRevLett.119.180801 (2017) (cited on p. 33).

49. Braunstein, S. L. & Caves, C. M. Statistical distance and the geometry of quantum states. *Physical Review Letters* **72,** 3439–3443. doi:10.1103/PhysRevLett.72.3439 (1994) (cited on pp. 33, 38).

50. Braunstein, S. L., Caves, C. M. & Milburn, G. Generalized Uncertainty Relations: Theory, Examples, and Lorentz Invariance. *Annals of Physics* **247,** 135–173. doi:10.1006/aphy.1996.0040 (1996) (cited on p. 33).

51. Giovannetti, V., Lloyd, S. & Maccone, L. Quantum Metrology. *Physical Review Letters* **96,** 010401. doi:10.1103/PhysRevLett.96.010401 (2006) (cited on p. 38).

52. Giovannetti, V., Lloyd, S. & Maccone, L. Advances in quantum metrology. *Nature Photonics* **5,** 222–229. doi:10.1038/nphoton.2011.35 (2011) (cited on p. 38).

53. Chuang, I. L. & Nielsen, M. A. Prescription for experimental determination of the dynamics of a quantum black box. *Journal of Modern Optics* **44,** 2455–2467. doi:10.1080/09500349708231894 (1997) (cited on p. 41).

54. D'Ariano, G. M. & Lo Presti, P. Quantum Tomography for Measuring Experimentally the Matrix Elements of an Arbitrary Quantum Operation. *Physical Review Letters* **86,** 4195–4198. doi:10.1103/PhysRevLett.86.4195 (2001) (cited on p. 41).

55. Altepeter, J. B., Branning, D., Jeffrey, E., Wei, T. C., Kwiat, P. G., Thew, R. T., O'Brien, J. L., Nielsen, M. A. & White, A. G. Ancilla-Assisted Quantum Process Tomography. *Physical Review Letters* **90,** 193601. doi:10.1103/PhysRevLett.90.193601 (2003) (cited on p. 41).

56. Song, X., Naghiloo, M. & Murch, K. Quantum process inference for a single-qubit Maxwell demon. *Physical Review A* **104,** 022211. doi:10.1103/PhysRevA.104.022211 (2021) (cited on p. 41).

57. Hawking, S. *The illustrated A brief history of time* Updated and expanded ed. OCLC: ocm34745975. 248 pp. (Bantam Books, New York, 1996) (cited on p. 50).

58. Helstrom, C. W. Quantum detection and estimation theory. *Journal of Statistical Physics* **1,** 231–252. doi:10.1007/BF01007479 (1969) (cited on p. 63).

59. Holevo, A. *Probabilistic and Statistical Aspects of Quantum Theory* doi:10.1007/978-88-7642-378-9 (Edizioni della Normale, Pisa, 2011) (cited on p. 63).

60. Koch, J. *et al.* Charge-insensitive qubit design derived from the Cooper pair box. *Physical Review A* **76,** 042319. doi:10.1103/PhysRevA.76.042319 (2007) (cited on p. 66).

61. Schreier, J. A. *et al.* Suppressing charge noise decoherence in superconducting charge qubits. *Physical Review B* **77,** 180502. doi:10.1103/PhysRevB.77.180502 (2008) (cited on p. 66).

62. Scully, M. O. & Zubairy, M. S. *Quantum Optics* 1st ed. doi:10.1017/CBO9780511813993 (Cambridge University Press, 1997) (cited on p. 69).

63. Carroll, M., Rosenblatt, S., Jurcevic, P., Lauer, I. & Kandala, A. Dynamics of superconducting qubit relaxation times. *npj Quantum Information* **8,** 132. doi:10.1038/s41534-022-00643-y (2022) (cited on p. 70).

64. Ranadive, A., Esposito, M., Planat, L., Bonet, E., Naud, C., Buisson, O., Guichard, W. & Roch, N. Kerr reversal in Josephson meta-material and traveling wave parametric amplification. *Nature Communications* **13,** 1737. doi:10.1038/s41467-022-29375-5 (2022) (cited on p. 72).

65. Pozar, D. M. *Microwave engineering* Fourth Edition. 732 pp. (John Wiley & Sons, Inc, Hoboken, NJ, 2012) (cited on p. 73).

66. Rapin, J. & Teytaud, O. *Nevergrad - A gradient-free optimization platform* Publication Title: GitHub repository. 2018 (cited on p. 75).

67. Pedregosa, F. *et al.* Scikit-learn: Machine Learning in Python. *Journal of Machine Learning Research* **12,** 2825–2830 (2011) (cited on p. 77).

68. Breiman, L. Random Forests. *Machine Learning* **45,** 5–32. doi:10.1023/A:1010933404324 (2001) (cited on p. 77).

69. Friedman, J. H. Greedy function approximation: A gradient boosting machine. *The Annals of Statistics* **29.** doi:10.1214/aos/1013203451 (2001) (cited on p. 77).

70. Friedman, J. H. Stochastic gradient boosting. *Computational Statistics & Data Analysis* **38,** 367–378. doi:10.1016/S0167-9473(01)00065-2 (2002) (cited on p. 77).

71. Hastie, T., Tibshirani, R. & Friedman, J. *The Elements of Statistical Learning* doi:10.1007/978-0-387-84858-7 (Springer New York, New York, NY, 2009) (cited on p. 77).

72. Nachman, B., Urbanek, M., De Jong, W. A. & Bauer, C. W. Unfolding quantum computer readout noise. *npj Quantum Information* **6,** 84. doi:10.1038/s41534-020-00309-7 (2020) (cited on p. 78).

73. Virtanen, P. *et al.* SciPy 1.0: fundamental algorithms for scientific computing in Python. *Nature Methods* **17,** 261–272. doi:10.1038/s41592-019-0686-2 (2020) (cited on p. 81).

74. Byrd, R. H., Lu, P., Nocedal, J. & Zhu, C. A Limited Memory Algorithm for Bound Constrained Optimization. *SIAM Journal on Scientific Computing* **16,** 1190–1208. doi:10.1137/0916069 (1995) (cited on p. 81).

75. Zhu, C., Byrd, R. H., Lu, P. & Nocedal, J. Algorithm 778: L-BFGS-B: Fortran subroutines for large-scale bound-constrained optimization. *ACM Transactions on Mathematical Software* **23,** 550–560. doi:10.1145/279232.279236 (1997) (cited on p. 81).

76. Oppenheim, A. V., Willsky, A. S. & Nawab, S. H. *Signals & systems* 2nd ed. 957 pp. (Prentice Hall, Upper Saddle River, N.J, 1997) (cited on p. 81).

77. Hyyppä, E. *et al.* Reducing Leakage of Single-Qubit Gates for Superconducting Quantum Processors Using Analytical Control Pulse Envelopes. *PRX Quantum* **5,** 030353. doi:10.1103/PRXQuantum.5.030353 (2024) (cited on p. 82).

78. Chen, Z. *et al.* Measuring and Suppressing Quantum State Leakage in a Superconducting Qubit. *Physical Review Letters* **116,** 020501. doi:10.1103/PhysRevLett.116.020501 (2016) (cited on p. 82).

79. Gambetta, J. M., Motzoi, F., Merkel, S. T. & Wilhelm, F. K. Analytic control methods for high-fidelity unitary operations in a weakly nonlinear oscillator. *Physical Review A* **83,** 012308. doi:10.1103/PhysRevA.83.012308 (2011) (cited on p. 82).

80. D'Ariano, G. M., Chiribella, G. & Perinotti, P. *Quantum theory from first principles: an informational approach* First paperback edition. 342 pp. (Cambridge University Press, Cambridge New York, 2019) (cited on p. 94).

81. Cross, A. W. *et al.* OpenQASM 3: A broader and deeper quantum assembly language. Publisher: arXiv Version Number: 2. doi:10.48550/ARXIV.2104.14722 (2021) (cited on p. 99).

Appendix A:

A.1 Energy-momentum Tensor of Superconductor

Appendix: for future reference, the stress-energy tensor of a superconductor is given by

$$\begin{aligned}
\delta T^{\alpha}_{\beta} &= -\delta(j^{\alpha}p_{\beta}) - \delta^{\alpha}_{\beta}\mathcal{L}, \\
\delta T^{0}_{0} &= \mathcal{H} = \mu\delta n + \boldsymbol{j}\cdot\delta\boldsymbol{p}, \\
\delta T^{a}_{0} &= \frac{1}{c}\delta(\mu\boldsymbol{j}), \\
\delta T^{0}_{a} &= -c\delta(n\boldsymbol{p}), \\
\delta T^{a}_{a} &= -n\delta\mu - p_a\delta j_a + j_b\delta p_b, \quad (\text{Not summing over } a) \\
\delta T^{a}_{b} &= -\delta(j_a p_b), \quad (a \neq b).
\end{aligned} \tag{A.1}$$

The trace

$$\delta T^{\alpha}_{\alpha} = \mu\delta n - \boldsymbol{p}\cdot\delta\boldsymbol{j} - 3(n\delta\mu + \boldsymbol{j}\cdot\delta\boldsymbol{p}) \tag{A.2}$$

A.2 Properties of the Entangled States

To emphasize the special meaning of the singlet states, we also introduce a circle symbol in addition to the labeled cup.

A generalized singlet state for N-level qudits is defined as a N-body entangled state

$$|A_N\rangle = \varepsilon_{m_1 m_2 \ldots m_N} |m_1 m_2 \ldots m_N\rangle , \tag{A.3}$$

where m_i takes value from 0 to $(N-1)$ and $\varepsilon_{m_1 m_2 \ldots m_N}$ is the *Levi-Civita symbol*.

$$|\Psi^-\rangle = |A_2\rangle = \tfrac{1}{\sqrt{2}}\left(|01\rangle - |10\rangle\right) =$$

$$|A_3\rangle = \tfrac{1}{\sqrt{6}}\left(|012\rangle - |021\rangle + |120\rangle - |102\rangle + |201\rangle - |210\rangle\right) =$$

$$(U \otimes I)\,|\Psi^-\rangle =$$ 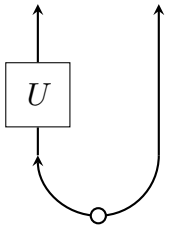 $$=$$ 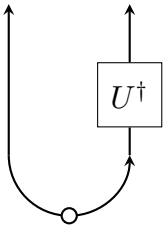 $$= (I \otimes U^\dagger)\,|\Psi^-\rangle$$

$$(U \otimes I \otimes I)\,|A_3\rangle =$$ 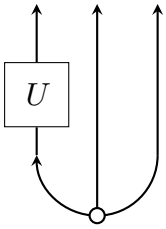 $$=$$ 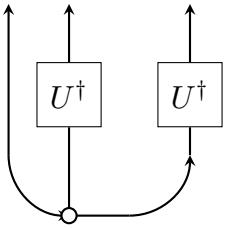 $$= (I \otimes U^\dagger \otimes U^\dagger)\,|A_3\rangle$$

Figure A.2: Cup and cap. (a) Cup and (b) cap.

A.3 Bell States

The definition of the Bell states are

$$\begin{aligned}
|\Phi^+\rangle &= \frac{1}{\sqrt{2}}\left(|00\rangle + |11\rangle\right) \\
|\Phi^-\rangle &= \frac{1}{\sqrt{2}}\left(|00\rangle - |11\rangle\right) \\
|\Psi^+\rangle &= \frac{1}{\sqrt{2}}\left(|01\rangle + |10\rangle\right) \\
|\Psi^-\rangle &= \frac{1}{\sqrt{2}}\left(|01\rangle - |10\rangle\right)
\end{aligned} \tag{A.4}$$

A.4 Relation between the Bell States

The Bell states are related by single-qubit π-rotations

$$\begin{aligned}
|\Phi^+\rangle &= X \otimes I\,|\Psi^+\rangle = I \otimes X\,|\Psi^+\rangle \\
|\Phi^+\rangle &= -iY \otimes I\,|\Psi^-\rangle = iI \otimes Y|\Psi^-\rangle \\
|\Phi^-\rangle &= -X \otimes I\,|\Psi^-\rangle = I \otimes X\,|\Psi^-\rangle \\
|\Psi^+\rangle &= Z \otimes I\,|\Psi^-\rangle = -I \otimes Z\,|\Psi^-\rangle
\end{aligned} \tag{A.5}$$

$$\begin{aligned}
\langle\Phi^+|U \otimes YU^\dagger Y|\Phi^+\rangle \\
\langle\Phi^-|U \otimes XU^\dagger X|\Phi^-\rangle \\
\langle\Psi^+|U \otimes ZU^\dagger Z|\Psi^+\rangle \\
\langle\Psi^-|U \otimes U^\dagger|\Psi^-\rangle
\end{aligned} \tag{A.6}$$

A.5 Arbitrary Single-qubit Rotation

There are two conventions for representing an arbitrary single-qubit rotation

1. The $R_{\hat{\boldsymbol{n}}}(\alpha)$ representation, where rotation axis $\hat{\boldsymbol{n}}$ and the rotation angle α. This representation is both geometrically intuitive with a clear physical meaning but less straightforward to implement. The matrix representation appears to be complicated.
2. The $U(\theta, \phi, \lambda)$ representation, where the three parameters are the Euler angle. This representation is slightly less geometrically intuitive but is easier algebraically featuring the decomposition into sequential rotations of simpler types.

We will discuss these two representations in the following subsections.

A.5.1 The $R_{\hat{\boldsymbol{n}}}(\alpha)$ Representation

The first one is based on the rotation axis $\hat{\boldsymbol{n}}$ and the rotation angle α. $\hat{\boldsymbol{n}}$ is a 3-dimensional unit vector specified by the polar angle θ and the azimuthal angle ϕ in the usual spherical coordinates

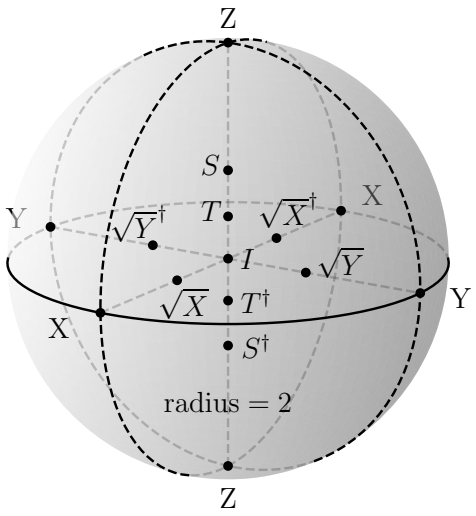

Figure A.3: **Ball of single qubit gates.** Every single qubit gate can be represented in this ball (up to a global phase). The structure of this ball is essentially equivalent to the 2QMES ball due to the *Choi–Jamiołkowski isomorphism* [80].

The rotation axis $\hat{\boldsymbol{n}}$ is given by

$$\hat{\boldsymbol{n}}(\theta,\phi) = \sin\theta\cos\phi\,\hat{\boldsymbol{x}} + \sin\theta\sin\phi\,\hat{\boldsymbol{y}} + \cos\theta\,\hat{\boldsymbol{z}} \tag{A.7}$$

Based on the parameterization, we alternatively use the notation $R(\alpha,\theta,\phi)$. The rotation along the $\hat{\boldsymbol{n}}$ axis with angle α is

$$R_{\hat{\boldsymbol{n}}}(\alpha) = \mathrm{e}^{-\mathrm{i}\,\alpha\boldsymbol{\sigma}\cdot\hat{\boldsymbol{n}}/2} = I\cos\frac{\alpha}{2} - \mathrm{i}\,\boldsymbol{\sigma}\cdot\hat{\boldsymbol{n}}\,\sin\frac{\alpha}{2} \tag{A.8}$$

The matrix representation

$$R_{\hat{\boldsymbol{n}}}(\alpha) = \begin{pmatrix} \cos\dfrac{\alpha}{2} - \mathrm{i}\,\sin\dfrac{\alpha}{2}\cos\theta & -\mathrm{i}\,\mathrm{e}^{-\mathrm{i}\,\phi}\sin\dfrac{\alpha}{2}\sin\theta \\ -\mathrm{i}\,\mathrm{e}^{\mathrm{i}\,\phi}\sin\dfrac{\alpha}{2}\sin\theta & \cos\dfrac{\alpha}{2} + \mathrm{i}\,\sin\dfrac{\alpha}{2}\cos\theta \end{pmatrix} \tag{A.9}$$

All single-qubit gates can be regarded as special cases of $R_{\hat{\boldsymbol{n}}}(\alpha)$. Here is an incomplete list of them

$$R_x(\alpha) = \begin{pmatrix} \cos\dfrac{\alpha}{2} & -\mathrm{i}\,\sin\dfrac{\alpha}{2} \\ -\mathrm{i}\,\sin\dfrac{\alpha}{2} & \cos\dfrac{\alpha}{2} \end{pmatrix}, \tag{A.10}$$

$$R_y(\alpha) = \begin{pmatrix} \cos\dfrac{\alpha}{2} & -\sin\dfrac{\alpha}{2} \\ \sin\dfrac{\alpha}{2} & \cos\dfrac{\alpha}{2} \end{pmatrix}, \tag{A.11}$$

$$R_z(\alpha) = \begin{pmatrix} \mathrm{e}^{-\mathrm{i}\,\alpha/2} & 0 \\ 0 & \mathrm{e}^{\mathrm{i}\,\alpha/2} \end{pmatrix}, \tag{A.12}$$

Defined in this way, $R_{\hat{\boldsymbol{n}}}(\alpha)$ contains a nontrivial geometric phase proportional to α. In order to see this, we write

$$R_{\hat{\boldsymbol{n}}}(2\pi) = -I = \mathrm{e}^{-\mathrm{i}\,\pi} I, \tag{A.13}$$

where an extra phase of $-\pi$ is accumulated every 2π rotation. To compensate for the global phase, the Pauli gates (effectively π rotations) are defined with an extra phase factor of $\mathrm{i} = \exp(\mathrm{i}\,\pi/2)$ relative to $R_{\hat{\boldsymbol{n}}}(\alpha)$

$$X = \mathrm{i}\, R_{\hat{\boldsymbol{x}}}(\pi) = \begin{pmatrix} 0 & 1 \\ 1 & 0 \end{pmatrix}, \tag{A.14}$$

$$Y = \mathrm{i}\, R_{\hat{\boldsymbol{y}}}(\pi) = \begin{pmatrix} 0 & -\mathrm{i} \\ \mathrm{i} & 0 \end{pmatrix}, \tag{A.15}$$

$$Z = \mathrm{i}\, R_{\hat{\boldsymbol{z}}}(\pi) = \begin{pmatrix} 1 & 0 \\ 0 & -1 \end{pmatrix}, \tag{A.16}$$

Also, for the Hadamard gate

$$H = \mathrm{i}\, R_{(\hat{\boldsymbol{x}}+\hat{\boldsymbol{z}})/\sqrt{2}}(\pi) = \frac{1}{\sqrt{2}} \begin{pmatrix} 1 & 1 \\ 1 & -1 \end{pmatrix}, \tag{A.17}$$

Similarly, the roots of the gates are defined as

$$\sqrt{X} = \mathrm{e}^{i\pi/4} R_{\hat{\boldsymbol{x}}}\left(\frac{\pi}{2}\right) = \frac{1}{2} \begin{pmatrix} 1+i & 1-i \\ 1-i & 1+i \end{pmatrix}, \tag{A.18}$$

$$S = \sqrt{Z} = \mathrm{e}^{i\pi/4} R_{\hat{\boldsymbol{z}}}\left(\frac{\pi}{2}\right) = \begin{pmatrix} 1 & 0 \\ 0 & i \end{pmatrix}, \tag{A.19}$$

$$T = \sqrt[4]{Z} = \mathrm{e}^{\mathrm{i}\,\pi/8} R_{\hat{\boldsymbol{z}}}\left(\frac{\pi}{4}\right) = \begin{pmatrix} 1 & 0 \\ 0 & \mathrm{e}^{\mathrm{i}\,\pi/4} \end{pmatrix}. \tag{A.20}$$

And generally, the phase gate

$$P(\alpha) = \mathrm{e}^{\mathrm{i}\,\alpha/2} R_{\hat{\boldsymbol{z}}}\left(\alpha\right) = \begin{pmatrix} 1 & 0 \\ 0 & \mathrm{e}^{\mathrm{i}\,\alpha} \end{pmatrix}. \tag{A.21}$$

Finally, we define a special case of the $R_{\hat{\boldsymbol{n}}}\left(\alpha\right)$ when $\hat{\boldsymbol{n}}$ lies in the $\hat{\boldsymbol{x}}$-$\hat{\boldsymbol{y}}$-plane

$$R(\phi, \alpha) = R_{\hat{\boldsymbol{n}}(\frac{\pi}{2},\phi)}(\alpha) = \begin{pmatrix} \cos\dfrac{\alpha}{2} & -\mathrm{i}\,\mathrm{e}^{-\mathrm{i}\,\phi}\sin\dfrac{\alpha}{2} \\ -\mathrm{i}\,\mathrm{e}^{\mathrm{i}\,\phi}\sin\dfrac{\alpha}{2} & \cos\dfrac{\alpha}{2} \end{pmatrix} \tag{A.22}$$

and especially the π rotations

$$R(\phi, \pi) = -\mathrm{i} \begin{pmatrix} 0 & \mathrm{e}^{-\mathrm{i}\,\phi} \\ \mathrm{e}^{\mathrm{i}\,\phi} & 0 \end{pmatrix}, \tag{A.23}$$

and $\pi/2$ rotations

$$R\left(\phi, \frac{\pi}{2}\right) = \frac{1}{\sqrt{2}} \begin{pmatrix} 1 & -\mathrm{i}\,\mathrm{e}^{-\mathrm{i}\,\phi} \\ -\mathrm{i}\,\mathrm{e}^{\mathrm{i}\,\phi} & 1 \end{pmatrix} \tag{A.24}$$

A.5.2 Virtual z-rotations

Before moving on with more complicated manipulation of quantum gates, this subsection is devoted for understanding virtual and physical frame rotations.

The qubit Hamiltonian in the lab frame is represented as

$$H_0^{\mathrm{lab}} = -\frac{1}{2}\hbar\omega_q\sigma_z, \tag{A.25}$$

The qubit is constantly rotating along the $-\hat{\boldsymbol{z}}$-axis. It would be helpful to distinguish the operators and states by labeling them in different frames. The ground state and excited state are used to encode a qubit

$$|0\rangle^{\mathrm{lab}} = |g\rangle^{\mathrm{lab}} = \begin{pmatrix} 1 \\ 0 \end{pmatrix}^{\mathrm{lab}}, \quad |1\rangle^{\mathrm{lab}} = |e\rangle^{\mathrm{lab}} = \begin{pmatrix} 0 \\ 1 \end{pmatrix}^{\mathrm{lab}}. \tag{A.26}$$

We define the Pauli operators in the rotating frame to be $\sigma_i^{\rm rot}(t)$, with

$$\sigma_z^{\rm rot}(t) = \sigma_z^{\rm lab}(t) = \sigma_z. \tag{A.27}$$

We supress the label for σ_z in any frames for simplicity. They satisfy the same commutation relation $[\sigma_j^{\rm rot}, \sigma_k^{\rm rot}] = 2\,{\rm i}\,\varepsilon_{jkl}\sigma_l^{\rm rot}$. In order to find the other two, we write down the Heisenberg equations of motion for the operators in the rotating frame,

$$\begin{aligned} \partial_t \sigma_x^{\rm rot} &= \frac{\rm i}{\hbar}[H_0^{\rm lab}, \sigma_x^{\rm rot}] = \omega_q \sigma_y^{\rm rot}, \\ \partial_t \sigma_y^{\rm rot} &= \frac{\rm i}{\hbar}[H_0^{\rm lab}, \sigma_y^{\rm rot}] = -\omega_q \sigma_x^{\rm rot}, \end{aligned} \tag{A.28}$$

At $t = 0$, the operators are the same in both frames

$$\begin{aligned} \sigma_x^{\rm rot}(0) &= \sigma_x^{\rm lab}(0), \\ \sigma_y^{\rm rot}(0) &= \sigma_y^{\rm lab}(0), \end{aligned} \tag{A.29}$$

From these equations we obtain the solution

$$\begin{aligned} \sigma_x^{\rm rot} &= \sigma_x^{\rm lab}\cos\omega_q t - \sigma_y^{\rm lab}\sin\omega_q t, \\ \sigma_y^{\rm rot} &= \sigma_x^{\rm lab}\sin\omega_q t + \sigma_y^{\rm lab}\cos\omega_q t. \end{aligned} \tag{A.30}$$

In general, we could use the evolution operator

$$U^{\rm lab}(t) = {\rm e}^{-{\rm i}\,H^{\rm lab}t/\hbar} = {\rm e}^{{\rm i}\,\omega_q t\sigma_z/2}, \tag{A.31}$$

to find out the relation between the quantum state represented in the two frames

$$|\psi(t)\rangle^{\rm rot} = U^{\rm lab\dagger}(t)\,|\psi(t)\rangle^{\rm lab} = |\psi(0)\rangle^{\rm lab} \tag{A.32}$$

The Hamiltonian in the rotation frame is $H_0^{\rm rot} = 0$. In other words, the qubit state keeps constant in the rotating frame, which make it the prototype of a reasonable computational space.

Now, let us consider adding an external microwave drive. Under rotating wave approximation

$$\begin{aligned} H^{\rm lab} &= H_0^{\rm lab} + H_d^{\rm lab} \\ &= -\frac{1}{2}\hbar\omega_q\sigma_z - \frac{1}{2}\hbar\Omega_R\left(\sigma_+^{\rm lab}{\rm e}^{-{\rm i}\,\omega_q t} + \sigma_-^{\rm lab}{\rm e}^{{\rm i}\,\omega_q t}\right), \\ &= -\frac{1}{2}\hbar\omega_q\sigma_z - \frac{1}{2}\hbar\Omega_R\left(\sigma_x^{\rm lab}\cos\omega_q t - \sigma_y^{\rm lab}\sin\omega_q t\right), \end{aligned} \tag{A.33}$$

where the raising and lowering operators are defined as [1]

$$\begin{aligned}\sigma_+^{\rm lab} &= |1\rangle^{\rm lab}\langle 0| = \frac{1}{2}\left(\sigma_x^{\rm lab} - {\rm i}\,\sigma_y^{\rm lab}\right),\\ \sigma_-^{\rm lab} &= |0\rangle^{\rm lab}\langle 1| = \frac{1}{2}\left(\sigma_x^{\rm lab} + {\rm i}\,\sigma_y^{\rm lab}\right),\end{aligned} \tag{A.34}$$

In the rotating frame, the Hamiltonian has the simple form

$$H^{\rm rot} = -\frac{1}{2}\hbar\Omega_R\sigma_x^{\rm rot}, \tag{A.35}$$

We define the *computational frame* F with an extra frame rotation ϕ_F,

$$\begin{aligned}\sigma_x^F &= \sigma_x^{\rm lab}\cos\big(\omega_q t + \phi_F\big) - \sigma_y^{\rm lab}\sin\big(\omega_q t + \phi_F\big),\\ \sigma_y^F &= \sigma_x^{\rm lab}\sin\big(\omega_q t + \phi_F\big) + \sigma_y^{\rm lab}\cos\big(\omega_q t + \phi_F\big).\end{aligned} \tag{A.36}$$

Now, consider adding a frame rotation

$$\phi_{F'} = \phi_F + \alpha, \tag{A.37}$$

We have the relation

$$\begin{aligned}\sigma_x^{F'} &= \sigma_x^F\cos\alpha - \sigma_y^F\sin\alpha,\\ \sigma_y^{F'} &= \sigma_x^F\sin\alpha + \sigma_y^F\cos\alpha,\\ A^{F'} &= {\rm e}^{-{\rm i}\,\alpha\sigma_z/2}A^F{\rm e}^{{\rm i}\,\alpha\sigma_z/2}\end{aligned} \tag{A.38}$$

The corresponding relation for quantum states

$$|\psi\rangle^{F'} = {\rm e}^{-{\rm i}\,\alpha\sigma_z/2}\,|\psi\rangle^F = R_z(\alpha)\,|\psi\rangle^F, \tag{A.39}$$

In other words, by doing the frame rotation, we are applying a virtual R_z gate. Practically, the computational frame is dynamically defined according to the value of ϕ_F, whose value is updated every time virtual R_z gate is applied on the system. This type of virtual R_z gate is the standard implementation for cQED-based quantum information processing due to the advantage that it does not introduce any extra noise. In terms of instrumentation, this approach only requires changing the phase of the intermediate frequency signal.

[1] The sign in the definitions complies with our definition of the ground and exited states.

Throughout this thesis, we always work in the computational frame F without explicit labeling

$$|0\rangle \equiv \begin{pmatrix} 1 \\ 0 \end{pmatrix}^F, \quad |1\rangle \equiv \begin{pmatrix} 0 \\ 1 \end{pmatrix}^F, \tag{A.40}$$

where F may reduce to the plain rotating frame in the special case if the z-rotations being used are all *physical*, which will be discussed in the next subsection.

A.5.3 Physical z-rotations

Arbitrary physical z-rotations can be implemented by cascading two π rotations (up to a global phase of π),

$$\begin{aligned} R\left(\phi + \frac{\alpha}{2}, \pi\right) R(\phi, \pi) &= -\begin{pmatrix} 0 & \mathrm{e}^{-\mathrm{i}\,(\phi+\alpha/2)} \\ \mathrm{e}^{\mathrm{i}\,(\phi+\alpha/2)} & 0 \end{pmatrix} \begin{pmatrix} 0 & \mathrm{e}^{-\mathrm{i}\,\phi} \\ \mathrm{e}^{\mathrm{i}\,\phi} & 0 \end{pmatrix} \\ &= -\begin{pmatrix} \mathrm{e}^{-\mathrm{i}\,\alpha/2} & \\ 0 & \mathrm{e}^{\mathrm{i}\,\alpha/2} \end{pmatrix} \\ &= -R_z(\alpha), \end{aligned} \tag{A.41}$$

where ϕ could be arbitrarily chosen but usually $\phi = 0$ for convenience. The advantage of physical z-rotations is they are natively compatible with parametric operations without any additional adjustments.

A.5.4 The $U(\vartheta, \varphi, \lambda)$ Representation

This matrix can be decomposed into three parts. Due the advantage in engineering implementation, it is usually defined as a standard type of gate, e.g. as part of the OPENQASM3 [81]. To experimentally implement arbitrary rotation, we represent the rotation with Euler angles.

$$U(\vartheta, \varphi, \lambda) = \begin{pmatrix} \cos\dfrac{\vartheta}{2} & -\mathrm{e}^{\mathrm{i}\,\lambda} \sin\dfrac{\vartheta}{2} \\ \mathrm{e}^{\mathrm{i}\,\varphi} \sin\dfrac{\vartheta}{2} & \mathrm{e}^{\mathrm{i}\,(\varphi+\lambda)} \cos\dfrac{\vartheta}{2} \end{pmatrix} \tag{A.42}$$

The above expression can be decomposed into the combination of Y-rotation sandwiched by two phase gates,

$$\begin{aligned} U(\vartheta,\varphi,\lambda) &= \begin{pmatrix} 1 & 0 \\ 0 & \mathrm{e}^{\,\mathrm{i}\,\varphi} \end{pmatrix} \begin{pmatrix} \cos\dfrac{\vartheta}{2} & -\sin\dfrac{\vartheta}{2} \\ \sin\dfrac{\vartheta}{2} & \cos\dfrac{\vartheta}{2} \end{pmatrix} \begin{pmatrix} 1 & 0 \\ 0 & \mathrm{e}^{i\lambda} \end{pmatrix} \\ &= P(\varphi)R_y(\vartheta)P(\lambda). \end{aligned} \tag{A.43}$$

In terms of experimental realization, the above expression can be transformed into various forms. On a platform with well-calibrated $\pi/2$ pulses, it is generally desirable to convert $R_y(\vartheta)$ into

$$\begin{aligned} R_y(\vartheta) &= \frac{1}{4} \begin{pmatrix} 1-i & 1+i \\ 1+i & 1-i \end{pmatrix} \begin{pmatrix} \mathrm{e}^{-\,\mathrm{i}\,\vartheta/2} & 0 \\ 0 & \mathrm{e}^{\,\mathrm{i}\,\vartheta/2} \end{pmatrix} \begin{pmatrix} 1+i & 1-i \\ 1-i & 1+i \end{pmatrix} \\ &= \sqrt{X}^{\dagger} R_z(\vartheta) \sqrt{X}, \end{aligned} \tag{A.44}$$

which can be easily implemented. Up to a global phase,

$$U(\vartheta,\varphi,\lambda) = R_z(\varphi)\sqrt{X}^{\dagger} R_z(\vartheta)\sqrt{X} R_z(\lambda). \tag{A.45}$$

Though the solution is not unique, the conversion table we choose is

$$\begin{aligned} \vartheta &= 2\arcsin\Big(\sin\frac{\alpha}{2}\sin\theta\Big) \\ \varphi &= \arctan\Big(\tan\frac{\alpha}{2}\cos\theta\Big) + \phi - \frac{\pi}{2} \\ \lambda &= \arctan\Big(\tan\frac{\alpha}{2}\cos\theta\Big) - \phi + \frac{\pi}{2}, \end{aligned} \tag{A.46}$$

which are defined for $-\pi \le \alpha \le \pi$ and $0 \le \theta \le \pi$. For the boundary case where $\alpha = \pm\pi$, we define

$$\begin{aligned} \vartheta &= \pi - |\pi - 2\theta| \\ \varphi &= \mathrm{sgn}(\pi - 2\theta)\frac{\pi}{2} + \phi - \frac{\pi}{2} \\ \lambda &= \mathrm{sgn}(\pi - 2\theta)\frac{\pi}{2} - \phi + \frac{\pi}{2}, \end{aligned} \tag{A.47}$$

A.5.5 Hermitian Conjugate of U

$$U(\vartheta, \varphi, \lambda) = \begin{pmatrix} \cos\dfrac{\vartheta}{2} & -\mathrm{e}^{\mathrm{i}\,\lambda}\sin\dfrac{\vartheta}{2} \\ \mathrm{e}^{\mathrm{i}\,\varphi}\sin\dfrac{\vartheta}{2} & \mathrm{e}^{\mathrm{i}\,(\varphi+\lambda)}\cos\dfrac{\vartheta}{2} \end{pmatrix} \tag{A.48}$$

$$U^{\dagger}(\vartheta, \varphi, \lambda) = \begin{pmatrix} \cos\dfrac{\vartheta}{2} & \mathrm{e}^{-\mathrm{i}\,\varphi}\sin\dfrac{\vartheta}{2} \\ -\mathrm{e}^{-\mathrm{i}\,\lambda}\sin\dfrac{\vartheta}{2} & \mathrm{e}^{-\mathrm{i}\,(\varphi+\lambda)}\cos\dfrac{\vartheta}{2} \end{pmatrix} \tag{A.49}$$

$$U^{\dagger}(\vartheta, \varphi, \lambda) = U(-\vartheta, -\lambda, -\varphi) \tag{A.50}$$